12-9-2006

Heat Transfer and Friction in Helically-Finned Tubes using Artificial Neural Networks

Gregory J. Zdaniuk

HEAT TRANSFER AND FRICTION IN HELICALLY-FINNED TUBES USING ARTIFICIAL NEURAL NETWORKS

By

Gregory Zdaniuk

A Dissertation
Submitted to the Faculty of
Mississippi State University
in Partial Fulfillment of the Requirements
for the Degree of Doctor of Philosophy
in Mechanical Engineering
in the Department of Mechanical Engineering

Mississippi State, Mississippi

December 2006

HEAT TRANSFER AND FRICTION IN HELICALLY-FINNED TUBES USING ARTIFICIAL NEURAL NETWORKS

By

Gregory Zdaniuk

Approved:

Louay M. Chamra Professor of Mechanical Engineering (Major Professor)	J. Mark Janus Associate Professor of Aerospace Engineering (Minor Professor)
Pedro Mago Assistant Professor of Mechanical Engineering (Committee Member)	Keith Walters Assistant Professor of Mechanical Engineering (Committee Member)
B. Keith Hodge Professor of Mechanical Engineering (Committee Member)	Steven Daniewicz Professor and Graduate Coordinator of Mechanical Engineering
Kirk H. Schultz Dean of the College of Engineering	

Name: Gregory Zdaniuk

Date of Degree: December 8, 2006

Institution: Mississippi State University

Major Field: Mechanical Engineering

Major Professor: Dr. Louay M. Chamra

Title of Study: HEAT TRANSFER AND FRICTION IN HELICALLY-FINNED TUBES USING ARTIFICIAL NEURAL NETWORKS

Pages in Study: 166

Candidate for Degree of Doctor of Philosophy

The last few decades have seen a significant development of complex heat transfer enhancement geometries such as a helically-finned tube. The arising problem is that as the fins become more complex, so does the prediction of their performance. In addition to discussing existing prediction tools, this dissertation demonstrates the successful use of artificial neural networks as a correlating method for experimentally-measured heat transfer and friction data of helically-finned tubes.

ACKNOWLEDGEMENTS

My path to this advanced degree would never be possible without the help of my family from whom I have received assistance and motivation. My sincere gratitude also goes to my dissertation committee members for their valuable contributions to this work. Finally, I wish to especially thank Dr. Louay Chamra for his continuous support in my graduate education and professional development.

TABLE OF CONTENTS

CHAPTER Page

LIST OF TABLES

LIST OF FIGURES

FIGURE Page

FIGURE Page

NOMENCLATURE

A	Surface area (m^2)
b	Node bias
c_p	Specific heat at constant pressure (J/kg-K)
C	Constant used in Nusselt number correlation
D	Diameter (m)
D_h	Hydraulic diameter (m)
e	Fin height (m)
$e+$	Roughness Reynolds number
f	Fanning friction factor
F	Node function
G	Heat transfer roughness function
h	Convective heat transfer coefficient (W/m^2-K)
H	Pitch for 180° rotation of twisted tape (m)
H_R	Helix ratio
j	Colburn j-factor ($=StPr^{2/3}$)
k	Thermal conductivity (W/m-K)
l_c	Characteristic length (m)
l_{csw}	Modified characteristic length for swirling flows (m)

L	Length of the tube (m)
$LMTD$	Log Mean Temperature Difference (K)
$\dot{m}$	Mass flow rate (kg/s)
MSE	Mean squared error
N_s	Number of fin starts
Nu	Nusselt number
P	Pressure (Pa)
p	Axial fin pitch (m)
Pr	Prandtl number
q	Heat flux (W/m^2)
$\dot{Q}$	Heat transfer rate (W)
r	Radial direction in cylindrical coordinates (m)
R	Momentum transfer roughness function
Ra	Rayleigh number
Re	Reynolds number
S	Number of nodes in a layer
St	Stanton number
t	Average rib width (m)
T	Temperature (K)
u^*	Friction (or shear) velocity (m/s)
V	Velocity (m/s)
w	Weight

x	Node input/output
z	Axial direction in cylindrical coordinates (m)

Greek Letters

α	Helix angle (°)
α' and α''	Corrugation shape angles (°)
β	Included angle (°)
Γ	Diffusivity (m^2/N-s)
Δ	Difference
θ	Circumferential direction in cylindrical coordinates (rad)
Θ	Equation matrix $\Theta = \begin{bmatrix} 1 & \ln \mathrm{Re} & \ln N_s & \ln(e/D) & \ln \alpha \\ \vdots & \vdots & \vdots & \vdots & \vdots \end{bmatrix}$
μ	Dynamic viscosity (N s/m^2)
v	Kinematic viscosity (m^2/s)
ρ	Density (kg/m^3)
τ	Shear stress (Pa)
Φ	Tube severity factor
χ	Constant
X	Vector of constants $\mathrm{X} = \begin{bmatrix} \ln \chi_1 \\ \chi_2 \\ \vdots \end{bmatrix}$
Ψ	Experimental data vector, e.g. $\Psi = \begin{bmatrix} \ln f \\ \vdots \end{bmatrix}$

Subscripts

eff	Effective
eq	Equivalent
i	Inside
in	At inlet
o	Outside (annulus side)
out	At outlet
p	Plain (or smooth) tube
r	Radial direction in cylindrical coordinates
turb	Turbulent
z	Axial direction in cylindrical coordinates
θ	Angular direction in cylindrical coordinates
$\parallel$	Component parallel to the fin
$\perp$	Component perpendicular to the fin

Superscripts

*	With the exception of u^*, refers to normalized network inputs and outputs

CHAPTER I

INTRODUCTION

The use of heat transfer enhancement has become widespread during the last 50 years. The goal of heat transfer enhancement is to reduce the size and cost of heat exchanger equipment. This goal can be achieved in two ways: active and passive enhancement. Of the two, active enhancement is less common because it requires the addition of external power (e.g., an electromagnetic field) to cause a desired flow modification. On the other hand, passive enhancement consists of alteration to the heat transfer surface or incorporation of a device whose presence results in a flow field modification. The most popular surface enhancement is the fin. The next section describes the basics of heat transfer enhancement and fins.

I.A Passive Heat Transfer Enhancement

Newton's Law of Cooling says that the rate of heat transfer between a solid and a surrounding fluid is directly proportional to the temperature difference between the two media, the surface area of the solid, and the convective heat transfer coefficient:

$$\dot{Q} = hA\left(T_{solid} - T_{fluid}\right) \tag{1}$$

In most heat transfer problems, engineers seek to obtain the maximum rate of heat transfer with a predefined (constant) temperature difference. Equation (1) shows that in

order to achieve this goal, either the surface area or the convective heat transfer coefficient has to be increased. The heat transfer coefficient and/or the surface area can be increased by using some kind of surface "enhancement." The remainder of this section presents two examples of fins used to enhance heat transfer from a flat plate.

Consider the situation shown in Figure 1. A horizontal plate is enhanced with vertical fins resulting in a considerable increase in surface area. Assume that a fluid flows over both plates in the horizontal direction and that natural convection effects are negligible. The fluid flow characteristics are essentially the same for both plates (boundary layers are similar) and the primary reason for heat transfer enhancement is the increase in heat transfer area. The fins shown in Figure 1 are geometrically two-dimensional.

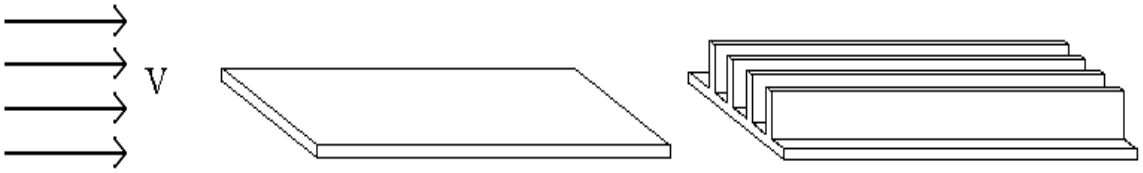

Figure 1. Flat Plate with Vertical Fins.

Now consider the arrangement illustrated in Figure 2. Fins are created by cutting and bending the plate in different locations. Such an arrangement is called a louvered fin. Compared to the plain plate, the louvered-fin plate has approximately the same surface area. However, the flow characteristics for the louvered fin are completely different because the fins induce more turbulence, better mixing of the fluid, and periodic disruptions in the boundary layer. As a result, the heat transfer coefficient is increased. The fins shown in Figure 2 are geometrically three-dimensional.

Increasing the rate of heat transfer by changing the geometry of a surface is called enhancement. The last two examples have shown how heat transfer enhancement can be achieved mainly due to surface area increase or mainly due to a change in the heat transfer coefficient. In most engineering applications, a geometry enhancement results in both an area increase and a change in the heat transfer coefficient.

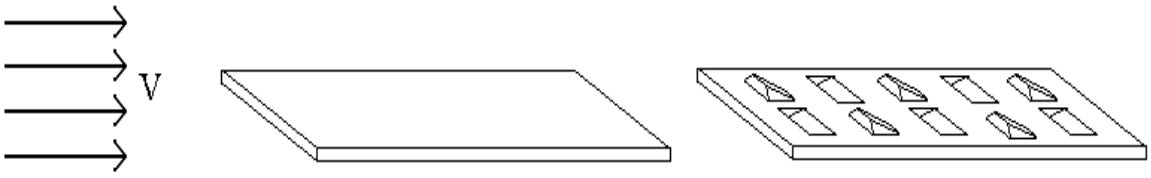

Figure 2. Flat Plate with Louvered Fins.

An important consequence of surface enhancement is the increase in the fluid pressure drop. In the first example, the wall shear stress is approximately the same for the flat plate and the finned plate, but the additional pressure drop comes from the increased contact area between the fluid and the solid (force = stress * area). In the second example, the contact area between the fluid and the solid is almost the same for both the plain and louvered-finned plate but the friction factor is increased due to increased turbulence, disruptions in the boundary layer, and form drag imposed by the fin. Hence, just like heat transfer, the pressure drop can be amplified due to an increase in surface area and/or an increase in friction factor.

I.B Helically-finned Tubes

Passive enhancement of heat transfer has also been used inside pipes. Webb (1982) gives an overview of different enhancement mechanisms available in commercial

tubes. Figure 3 is of great visual help in identifying the roughness type as well as the relevant nomenclature.

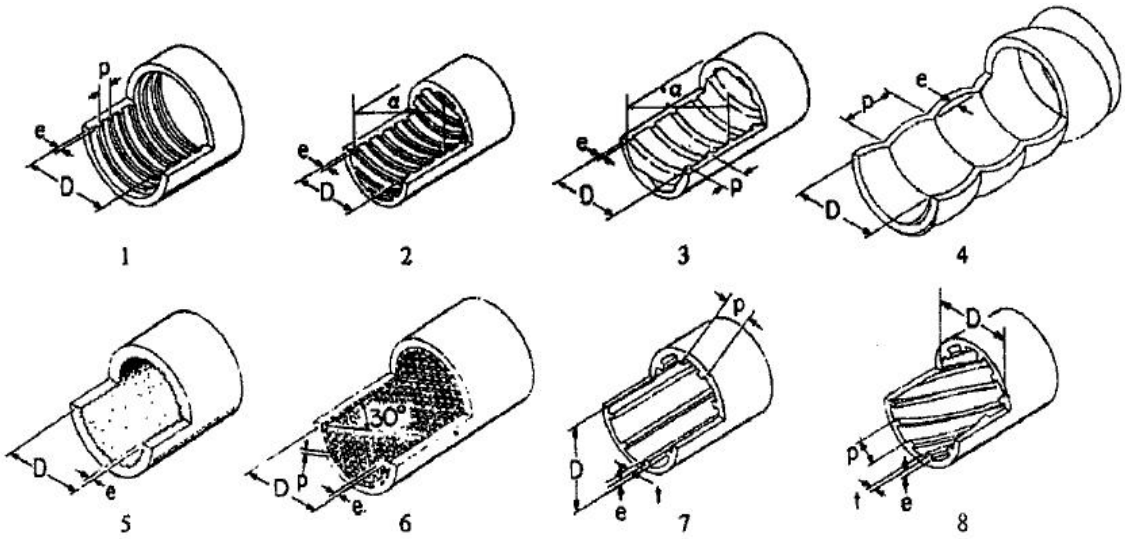

Figure 3. Sketches of Typical Roughness Configurations [Webb (1982)]. 1-Transverse Rib, 2-Helical Rib, 3-'Turbochil' Type, 4-Corrugated, 5-Sand-grain, 6-Three-dimensional, 7-Axially-finned Tube, 8-Helically-finned Tube.

One contemporary enhancement geometry is the helical fin shown in Figure 4. The helical fin is considered to be two-dimensional. Several geometric variables describe a helical fin. Figure 5 provides a pictorial description of the geometric variables. These variables are: the fin height (e), the fin pitch (p), the helix angle (α), number of starts (N_s), and included angle (β). The fin height is the distance measured from the internal wall of the tube to the top of the fin. The fin pitch is the distance between the centers of two fins measured in the axial direction. The helix angle is the angle the fin forms with the tube axis. The number of starts refers to how many fins one can count around the circumference of the tube. Finally, the angle at which the sides of the fin meet is called the included angle.

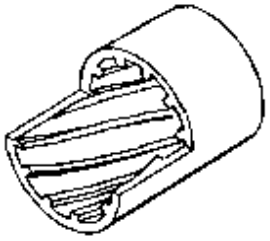

Figure 4. A Helically-finned Tube.

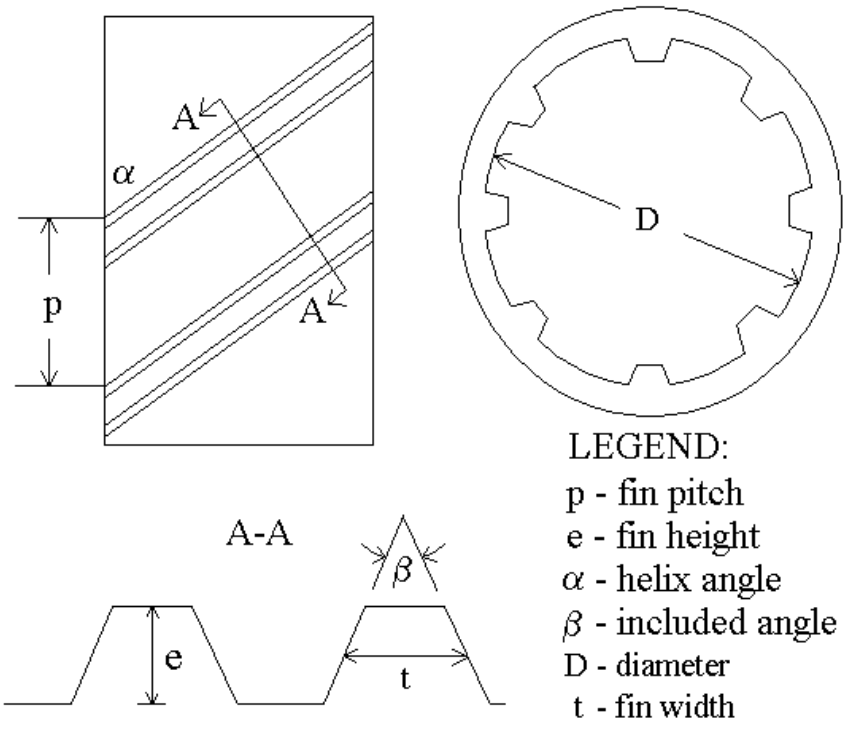

Figure 5. Geometric Variables of the Helical Fin.

Two special cases are worth mentioning, namely tubes with 90° and 0° helix angles. A 90° helix angle corresponds to the transverse fin, and the 0° angle means the tube is axially finned (as shown in Figure 6). In the case of the transverse fin, the above-mentioned definition of the number of starts does not apply. Likewise, for the case of the axial fin, the definition of fin pitch is invalid. Even though technically, the transversely-

finned and axially-finned tubes do not belong to the helically-finned tube "family," they can be classified as such under the 0° and 90° helix angle claim. There is an additional justification for this classification. Research has shown that tubes with small helix angles (less than 10°) behave very similarly to axially-finned tubes and that tubes with large helix angles (above 80°) display the same characteristics as a transversely-finned tube.

Presently, to predict heat transfer and pressure drop in helically-finned tubes engineers rely on empirical correlations. Tubes with axial and transverse fins have been studied extensively and techniques for predicting the friction factor and heat transfer coefficient exist. However, fluid flow in helically-finned tubes is more difficult to model and few attempts have been made to obtain non-empirical solutions. The purpose of this dissertation is to experimentally study the fluid flow in helically-finned tubes and to develop a tool aimed at predicting their performance.

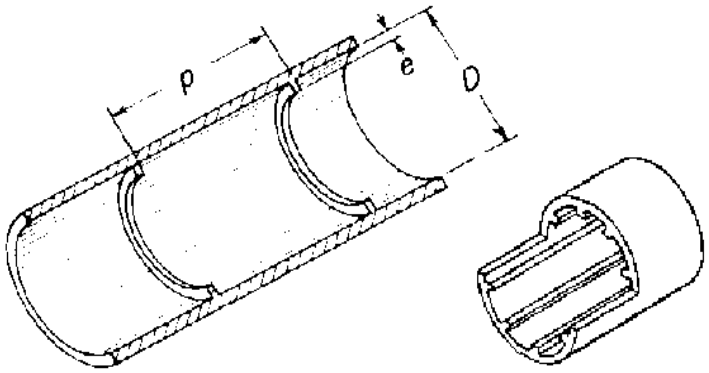

Figure 6. Transversely- and Axially-finned Tubes.

CHAPTER II

LITERATURE REVIEW

The purpose of this chapter is to describe the research completed on fluid flow and heat transfer in tubes with helical enhancements. Publications dealing with theoretical and empirical models will be discussed. In addition, articles of relevance to the mathematics governing the flow in helically-finned tubes will be examined.

II.A Empirical and Semi-empirical Models

An excellent source that concisely describes many different models of flow in enhanced tubing was published by Ravigururajan (1999). Ravigururajan (1999) outlined various correlations available for predicting the thermal-hydraulic performance of turbulent flow in enhanced tubes. Each correlation was classified as either analogy-based or statistical/empirical. Information about the relevant applications, the source, and the limitations of each correlation was compiled. Many references cited by Ravigururajan (1999) are listed in this chapter.

Li et al. (1982) was the first study that attempted to describe the mechanisms of heat transfer in helically-finned tubes by means of flow visualization. Li et al. (1982) performed a study on four tubes with rounded ribs, helix angles between 38° and 80°, and one or three starts, and used the hydrogen-bubble technique to take high-speed

photographs of the fluid flow. Traces of hydrogen bubbles revealed the direction of the flow near the ribs.

Photographs taken by Li et al. (1982) indicated that in laminar flow, bubbles follow parabolic patterns. In the turbulent regime, these patterns break down because of random separation vortices. Additionally, tubes with helical ridges showed lower transition Reynolds numbers than the smooth tube.

Spiral flow was observed for all tubes in the turbulent flow regime. In the 80°-helix tube, the flow direction near the wall was rather different from the rib trend. Besides, bubbles seemed to oscillate back and forth between ribs implying the existence of separation vortices near the wall. In tubes with smaller helix angles, there was more agreement between the flow direction and the rib trend. Li et al. (1982) concluded that "spiral flow and boundary-layer separation flow both occurred in helical-ridging tubes, but with different intensities in tubes having different configurations."

Li et al. (1982) performed additional heat transfer and pressure drop experiments using 20 enhanced brass tubes with one to four starts and helix angles between 41.4° and 81.8°. Li et al. (1982) reported their results in terms of the roughness functions of momentum transfer R [Nikuradse (1950), Schlichting (1979)] and heat transfer G [Dipprey and Sabersky (1963)]. The R and G functions facilitate comparison of the data because the functions are considered independent of the geometry and size of the test channel.

G and R represent the effect of ribs on momentum and heat transfer in the vicinity of the wall and are defined by the following expressions:

$$R = \sqrt{2/f} + 2.5\ln(2e/D) + 3.75 \tag{2}$$

$$G = \frac{(f/2St) - 1}{\sqrt{f/2}} + R \tag{3}$$

Functions R and G are generally plotted versus local parameters such as the roughness Reynolds number

$$e+ = \frac{e}{D}\mathrm{Re}\sqrt{f/2} = \frac{eu^*}{\nu} \tag{4}$$

and the enhancement geometry (α, p/e, or rib shape). Gee and Webb (1980) demonstrate that geometries with different helix angles, rib shapes, or pitch-to-height ratios are non-similar. Therefore, functions developed on the basis of similarity laws [e.g., *R(e+)* and *G(e+)*] require empirical corrections. Hence, there is need to incorporate parameters such as α, p/e, and rib shape in the analysis.

Li et al. (1982) limited their analysis to single-start tubes because, based on their flow visualizations, single-start tubes achieve higher intensities of boundary-layer separation than multiple-start tubes with same parameters (e/D, p/e). Thus, according to Li et al. (1982), single-start tubes are more beneficial for heat transfer applications. Li et al. (1982) obtained the following correlations for R and G:

$$R = 0.995\left(e/D\right)^{-0.156}(p/e)^{0.465}(\alpha/90)^{0.484}\exp\left[\frac{(\ln(\mathrm{Re}) - 9.62)^2}{1000\left(p/e\right)^{-1.38}}\right] \tag{5}$$

$$G = 0.478(e/D)^{-0.621}(\alpha/90)^{-0.869}(e+)^{0.641+0.105\ln(e/D)}\,\mathrm{Pr}^{0.57} \tag{6}$$

Li et al. (1982) combined equations (2) and (5), and refined constants to obtain the following expression for the Fanning friction factor:

$$\sqrt{\frac{f}{2}} = 3.42\ln\left(\frac{D}{2e}\right) - 4.64 + 1.25\left(\frac{e}{D}\right)^{-0.057}\left(\frac{p}{e}\right)^{0.5}\left(\frac{\alpha}{90}\right)^{1.14}\exp\left[\frac{(\ln(\mathrm{Re}) - 9.62)^2}{1000\left(\frac{p}{e}\right)^{-1.38}}\right] \qquad (7)$$

Another investigation of flow visualization in tubes with helical roughness was undertaken by Ravigururajan and Bergles (1994). Ravigururajan and Bergles (1994) used water in a transparent plexiglass tube with a wire coil insert. Dyes of different colors were introduced into the flow at different distances from the tube wall in order to identify the patterns associated with each region of the tube (e.g., core, wall, etc…). A blue dye was injected just above the disruption height, and a red dye was injected close to the wall. Both dyes were injected at a distance of 20 diameters upstream of the coil insert. Photographs of flow patterns obtained by Ravigururajan and Bergles (1994) are reproduced in Figure 7.

Ravigururajan and Bergles (1994) drew the following conclusions from the photographs:

1) Flow visualization tests indicated the presence of a rotational layer close to the wall and a crossover layer in the core of the tube. The rotational pattern dominated for helix angles less than 30°, and the crossover pattern dominated for helix angles larger than 70°.
2) With increasing roughness height, the transition *Re* decreased.
3) As the roughness height increased, the angle of fluid rotation was increased.
4) In augmented tubes, the hydrodynamic developing length was insignificant.
5) Decreasing the helix angle decreased turbulence and the transition *Re*.

6) The thickness of the rotational layer decreased with increasing *Re*.
7) Rotational angles tended towards the helix angle as *Re* was decreased.
8) A rotating layer was also present in turbulent flows.
9) At a *p/e* = 8 ratio, both friction and heat transfer reached a maximum value.

Nakayama et al. (1983) tested tubes with spiral ribs having helix angles ranging from 0° to 80° and between 2 and 10 starts. The ribs had rounded cross sections. Nakayama et al. (1983) compared their results with other investigators in terms of the roughness functions of heat transfer (G) and momentum heat transfer (R).

Based on the studies of Li et al. (1982), Nakayama et al. (1983) classified their tubes into three categories and proposed different correlations accordingly. The first category corresponded to a helix angle greater than 60°, where roughness form drag is the major contribution to the pressure drop (implying that rounded ribs cause a much smaller pressure drop than sharply-edged fins). For this category, Nakayama et al. (1983) proposed the following correlations for R and G:

$$R = 4.5 + 5.63 \times 10^{-4} (p/e)^{2.59} \ln(e+) \tag{8}$$

$$G / \mathrm{Pr}^{0.57} = 4.75 e+^{0.28} \tag{9}$$

The second category applied to tubes with a helix angle of less than 45° where flow is directed along the ribs. Hence, the roughness function of momentum was expected to be a function of $e+$, α, and p/e:

$$R = 5.02 e+^{0.15} (\alpha / 45°)^{-0.16} (p \sin(\alpha)/e)^{0.1} \tag{10}$$

Data for G in the $\alpha < 45°$ tube category were well represented by equation (9).

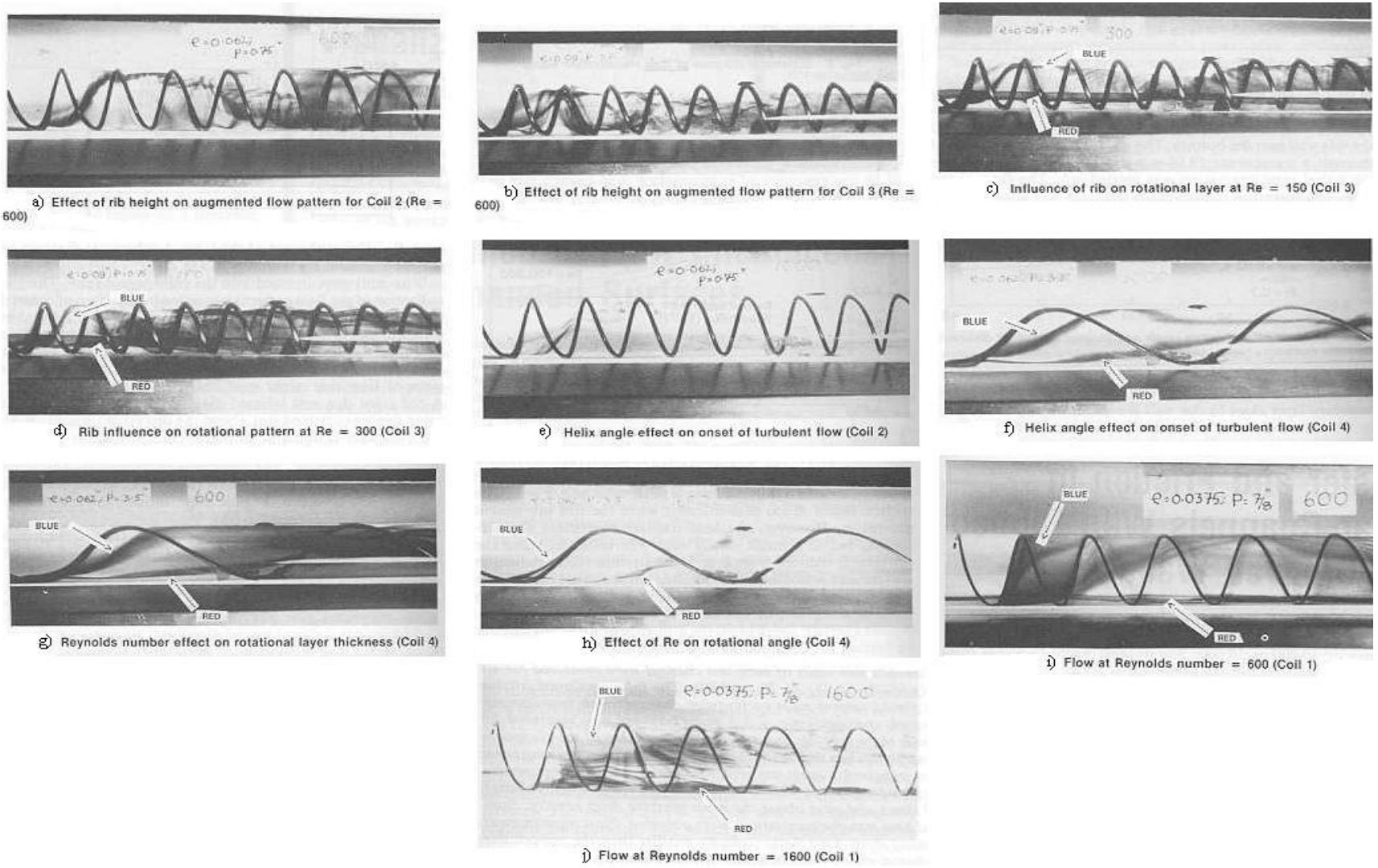

Figure 7. Visualization Photographs Taken by Ravigururajan and Bergles (1994).

The third category of tubes discussed by Nakayama et al. (1983) included tubes with a helix angle between 45° and 60° "where the flow near the wall undergoes a transition from a swirling-dominated flow to a crossover flow." The correlation of data in the transition range was difficult because data are not systematic. Nonetheless, for tubes with helix angles between 45° and 60° Nakayama et al. (1983) proposed the following correlations for *R* and *G*:

$$R = 5.14e+^{0.12} (\alpha / 45°)^{-0.8} (p \sin(\alpha) / e)^{0.1} \tag{11}$$

$$G / \mathrm{Pr}^{0.57} = 4.90e+^{0.37} \tag{12}$$

Nakayama et al. (1983) concluded that the criteria for hydrodynamically rough and transition flow regimes depend not only on *e*+ but also on the helix angle, rib shape, and the pitch-to-height ratio. Therefore, according to the authors, the definition of a parameter domain for analysis of rough regimes is open to discussion.

An earlier study conducted by Gee and Web (1980) investigated tubes with helical square-shaped ribs. The helix angle varied between 30° and 70°, and the pitch was held constant at 3.81 mm. Gee and Webb (1980) used air at Reynolds numbers varying from 6 000 to 65 000. In their analysis, Gee and Webb (1980) included data for tubes with transverse ribs obtained by Webb et al. (1971).

Gee and Webb (1980) plotted *R* versus *e*+ (but gave no explicit correlation for *R*). The curve started at $R \approx 8$ and $e+ = 6$ and reached a constant value of $R \approx 8.8$ at $e+ = 30$. Gee and Webb (1980) defined *R* and *G* in the following fashion:

$$R = \left[\sqrt{2/f} + 2.5 \ln(2e/D) + 3.75\right](\alpha / 50)^{0.16} \tag{13}$$

$$G/\mathrm{Pr}^n = \left[\frac{(f/2St)-1}{\sqrt{f/2}} + R\right](\alpha/50)^i \tag{14}$$

where $i = 0.37$ for $\alpha < 50°$ and $i = -0.16$ for $\alpha > 50°$. In equations (13) and (14), there is no dependence on *p/e* because the tubes tested by Gee and Webb (1980) had a constant pitch. By comparing their results with other researchers, Gee and Webb (1980) concluded that:

1) Helical rib-roughness provides higher heat transfer per unit friction than transverse roughness, and
2) The preferred operating condition is at a roughness Reynolds number corresponding to $e+ = 20$.

Webb et al. (2000) published a more comprehensive study where tubes with different helix angles, starts, fin pitch, and height were tested. Webb et al. (2000) varied the helix angle between 25° and 45°, the number of starts between 18 and 45, and the rib height between 0.33 mm and 0.55 mm. Webb et al. (2000) used water for the inside and condensing R-12 on the outside of the tubes. The modified Wilson plot technique [Briggs and Young (1968)] was used to obtain the refrigerant-side heat transfer coefficient.

Webb et al. (2000) derived empirical explicit correlations for *j* and *f*:

$$f = 0.108\,\mathrm{Re}^{-0.283}\,N_s^{0.221}(e/D)^{0.785}\alpha^{0.78} \tag{15}$$

$$j = \mathrm{St}\,\mathrm{Pr}^{2/3} = 0.00933\,\mathrm{Re}^{-0.181}\,N_s^{0.285}(e/D)^{0.323}\alpha^{0.505} \tag{16}$$

Webb et al. (2000) have also derived correlations based on the heat transfer-momentum transfer analogy approach:

$$R = 4.762(e+)^{-0.2138}\,N_s^{-0.1096}\alpha^{-0.297} \tag{17}$$

$$G / \mathrm{Pr}^{0.57} = 1.714(e+)^{0.06} N_s^{-0.21} \alpha^{-0.16} \tag{18}$$

Webb et al. (2000) examined additional performance parameters for each tube. These parameters were $(h/h_p)/(A/A_p)$ and the efficiency index,

$$\eta = \frac{h / h_p}{f / f_p} \tag{19}$$

where the subscript p stands for smooth (or plain) tube. The first parameter indicated the ratio of the increase of the heat transfer coefficient to the increase of the surface area with respect to the plain tube. This parameter helps to determine what portion of the heat transfer coefficient increase is due to the increase of the surface area and what portion is due to the alteration of the flow field. The efficiency index, η, helps to evaluate the effect of fins on both the heat transfer and friction factor. The higher the efficiency index, the better the enhancement geometry. Both parameters depend on the geometry of the tube, the Reynolds number, and the Prandtl number of the fluid.

By examining the above-defined performance parameters, Webb et al. (2000) concluded that the two key factors that affect h/h_p in helically-finned tubes are the area increase and fluid mixing in the interfin region caused by flow separation and reattachment[†]. The combination of the two determines the enhancement intensity[‡].

Withers (1980a) tested fourteen single-helix corrugated tubes (see Figure 3) at various Reynolds and Prandtl numbers ($10\,000 < Re < 120\,000$; $2.3 < Pr < 10.4$). None of the tubes tested by Withers (1980a) indicated fully-rough behavior (f being

[†] A conclusion which is in agreement with the flow visualization experiments of Li et al. (1982).
[‡] The levels at which the increased surface area and the boundary-layer mixing contribute to the apparent heat transfer coefficient depend on the enhancement geometry (as discussed in CHAPTER I), the *Re*, and the *Pr*. The higher the helix angle and the Reynolds number, the higher the chance of flow separation. The lower the *p/e* and *e/D* ratio, the higher the chance of skimming flow, etc…

independent of *Re*). Friction factor data were correlated by means of the following expression:

$$\sqrt{f/2} = -\frac{1}{2.46\ln\left[r + (7/\mathrm{Re})^{m}\right]} \tag{20}$$

where operands *r* and *m* were empirically determined for each tube. Heat transfer data were correlated in a more comprehensive manner:

$$G/\mathrm{Pr}^{0.5} = 7.22(e+)^{0.127}(p/D)^{-1/3} \tag{21}$$

Withers (1980a) used the above equations to perform a parametric study to find the optimum fin height (i.e., the fin height that yields highest heat transfer coefficients and lowest friction factors) for single-helix corrugated tubes (the pitch was held constant). After looking at different Reynolds and Prandtl numbers, Withers (1980a) inferred that in every case, the optimum *e/D* ratio is 0.04.

Withers (1980b) published data for tubes with multi-start helix ridges. The same experimental apparatus as in Withers (1980a) was used to test 25 tubes with helix angles varying between 29° and 55°. Equation (20) along with a new set of operands *r* and *m* was used to correlate the friction factor to the Reynolds number. By observing the behavior of the friction factor, Withers (1980b) conjectured that a shift in flow behavior occurs at *p/D* = 0.36. The explanation was that "at higher values of *p/D* a substantial degree of swirl could occur, as opposed to more abrupt cascading when *p/D* is below 0.36." Withers (1980b) graphed *R* versus *e+* for nine tubes, but except for equation (20), made no attempt to correlate his friction data more comprehensively.

Withers (1980b) heat transfer data were correlated much more thoroughly. The correlating equation for *G* was given by:

$$G/\mathrm{Pr}^{0.5} = 5.68(e+)^{0.136}(e/p)^{-1/8} \tag{22}$$

Unfortunately, equation (22) does not include the effect of helix angle or number of starts. However, Withers was one of the first to attempt the use of the *G* correlating function to tubes with helical roughness.

Twelve single-start spirally corrugated geometries were tested by Gupta and Rao (1979). Gupta and Rao's (1979) test used water and power-law type non-Newtonian fluids. Non-Newtonian fluids are beyond the scope of this dissertation; therefore, the correlations obtained by Gupta and Rao (1979) and listed here assume a behavior index equal to one (water). Gupta and Rao (1979) found that an important factor in analyzing spirally-corrugated tubes was the tube severity factor, Φ, defined as e^2/pD.

Gupta and Rao (1979) correlated the friction factor by the following equation:

$$f = 0.079\exp(-79.5\Phi)\,\mathrm{Re}^{-0.25\exp(-210\Phi)} \tag{23}$$

The interesting fact is that equation (23) reduces to the Blasius form when the tube severity factor is zero (plain tube). The Nusselt number was correlated as:

$$Nu = 0.029\exp(-45\Phi)\,\mathrm{Re}^{0.8\exp(13\Phi)}\,\mathrm{Pr}^{0.4\exp(13\Phi)} \tag{24}$$

Equation (24) reduces to the Dittus-Boelter form when $\Phi = 0$, and the constant 0.029 is replaced by 0.023. Gupta and Rao (1979) used the correlations for *f* and *Nu* to perform an extensive parametric study, which showed that the most favorable spiral configuration (highest increase in *Nu* with lowest increase in *f*) is achieved with a tube severity factor ranging between 0.00067 and 0.0020.

Ganeshan and Rao (1982) tested seven spirally-corrugated tubes of one to four starts with a constant helix angle of 65°. In their study, the authors used water and power-

law non-Newtonian fluids to correlate the G and R functions versus $e+$. As was the case for the equations of Gupta and Rao (1979), correlations obtained by Ganeshan and Rao (1982) and listed here assume a behavior index equal to one (water):

$$R \cdot \left[e/(N_s p - t)\right]^{0.52} N_s^{0.24} = 0.273 \ln(e+) + 0.127 \tag{25}$$

$$\log(G/\mathrm{Pr}^{0.55}) = 2.576 - 1.707 \log(e+) + 0.497\left[\log(e+)\right]^2 - 0.0103\left[\log(e+)\right]^3 \tag{26}$$

where t is the rib width. The correlations are applicable for $20 < e+ < 300$.

Ganeshan and Rao (1980) made several interesting remarks about their findings:

1) R always increased with $e+$.
2) Due to the unique nature of flow in corrugated tubes, R was not independent of $e+$ in the fully-rough regime as is typically seen in smooth pipes ($e+ > 70$).
3) Inter-rib spacing was a more significant parameter than pitch.
4) No significant dependence of G on pN_s/e was observed.[†]
5) pN_s/D had a small effect on heat transfer

Sethumadhavan and Rao (1986) investigated friction and heat transfer characteristics of five spirally corrugated tubes with one to four corrugation starts with a constant 65° helix angle. Water and 50 percent glycerol were used as test fluids. Steam was condensed on the outside of the test tube.

The experimental results of the friction factor were reduced in terms of the momentum transfer roughness function $R(e+)$ and tube severity factor $\Phi = e^2/pD_{eq}$ (where $D_{eq} = D - e$) in the following equation:

[†] pN_s corresponds to the axial distance through which a rib makes a 360° turn along the tube circumference.

$$R \cdot \left[e^2 / (pD_{eq})\right]^{0.33} = 0.40(e+)^{0.164} \quad \text{for } 3 < \text{e+} < 200 \tag{27}$$

Sethumadhavan and Rao (1986) concluded that the friction factors were higher than for a smooth tube and, furthermore, increased with decreasing pitch (or increasing number of starts).

The heat transfer coefficient results were reduced via the heat transfer roughness function *G(e+, Pr)* in the following fashion:

$$G / \mathrm{Pr}^{0.55} = 8.6(e+)^{0.13} \quad \text{for } 25 < \text{e+} < 180 \tag{28}$$

Sethumadhavan and Rao (1986) compared their results with data from Gupta and Rao (1979) and Withers (1980a and 1980b). The agreement was found to be good despite the differences in tube geometries and fluids used by the different researchers. This fact supports the idea of using momentum transfer and heat transfer functions to describe friction and heat transfer characteristics of complex, yet structured fins.

Vicente et al. (2004) compared spirally-corrugated tube correlations of 8 different researchers and concluded that for the same operating conditions, differences in predictions of friction factors and Nusselt numbers can be as high as 231 and 167 percent, respectively. This discrepancy motivated Vicente et al. (2004) to obtain experimental data for a wide variety of flow conditions. Vicente et al. (2004) performed experiments on a family of 10 helically corrugated tubes under the following conditions: *e/D* ranging from 0.02 to 0.06, *p/D* from 0.6 to 1.2, *Re* from 2 000 to 90 000, and *Pr* from 2.5 to 100.

Based on about 600 data points, Vicente et al. (2004) correlated the friction factor with the following equation:

$$f = 1.47(e/D)^{0.91}(p/D)^{-0.54}\,\mathrm{Re}^{-0.16} \tag{29}$$

or using the definition of the severity index,

$$f = 1.53\Phi^{0.46}\,\mathrm{Re}^{-0.16} \tag{30}$$

Vicente et al. (2004) also analyzed the results with the momentum roughness function *R(e+)* and proposed that:

$$\begin{aligned} R(e+) &= 2.60(p/e)^{0.35} \quad \text{for} \quad e+ < 925(p/e)^{-1} \\ R(e+) &= 1.07(p/e)^{0.48}(e+)^{0.13} \quad \text{for} \quad e+ > 925(p/e)^{-1} \end{aligned} \tag{31}$$

Vicente et al. (2004) noted that the friction factors did not reach an asymptotical value with increasing *Re* and thus did not show a "sand-grain" behavior. According to the authors, the flow inside helically corrugated tubes is not fully understood, but it seems reasonable to assume that rotation flow and axial flow exist concurrently. The degree of flow rotation depends on the helix angle, and how rotation spreads to the core of the flow depends on the flow conditions, namely the Reynolds number. Flow separation may or may not exist depending on the shape of the corrugation.

Based on about 800 data points, Vicente et al. (2004) fitted the heat transfer data with the following equation:

$$Nu = 0.403(e/D)^{0.53}(p/D)^{-0.29}(\mathrm{Re}-1500)^{0.74}\,\mathrm{Pr}^{0.44} \tag{32}$$

or using the definition of the severity index,

$$Nu = 0.374\Phi^{0.25}(\mathrm{Re}-1500)^{0.74}\,\mathrm{Pr}^{0.44} \tag{33}$$

Vicente et al. (2004) also analyzed the results with the heat transfer roughness function *G(e+)* and proposed that:

$$\begin{aligned} G(e+)\,\mathrm{Pr}^{-0.57} &= 14.3 \qquad \text{for} \quad 15 < \mathrm{e+} < 60 \\ G(e+)\,\mathrm{Pr}^{-0.57} &= 5.13(\mathrm{e+})^{0.25} \qquad \text{for} \quad 60 < \mathrm{e+} < 600 \end{aligned} \tag{34}$$

Vicente et al. (2004) concluded that *Nu* augmentation increased with increasing severity index and *Pr* and decreased with increasing *Re*. The reason for this behavior is that at low *Re* numbers the boundary layer is relatively thick (and the thermal resistance high) and mixing induced by the corrugations helps to decrease the boundary-layer thickness, lowering its thermal resistance. At high *Re* numbers, the boundary layer is thinner and mixing does not improve the situation as much as for the low *Re* case. Accordingly, Vicente et al. (2004) suggested using tubes with a high severity index for low *Re* applications and tubes with an intermediate severity index for high *Re* applications.

Newson and Hodgson (1974) tested 32 helically corrugated tubes of different types. These types are shown in Figure 8 and are classified as follows:

a) 4 start, swaged (or roped) helical,

b) 4 start, positive indentation helical,

c) 8 start, swaged helical,

d) 8 start, longitudinal wave,

e) 16 start, multifluted,

f) 30 start, multifluted, high density fluting.

A detailed analysis of the heat transfer and pressure drop performance was accomplished for only tubes a, b, and c.

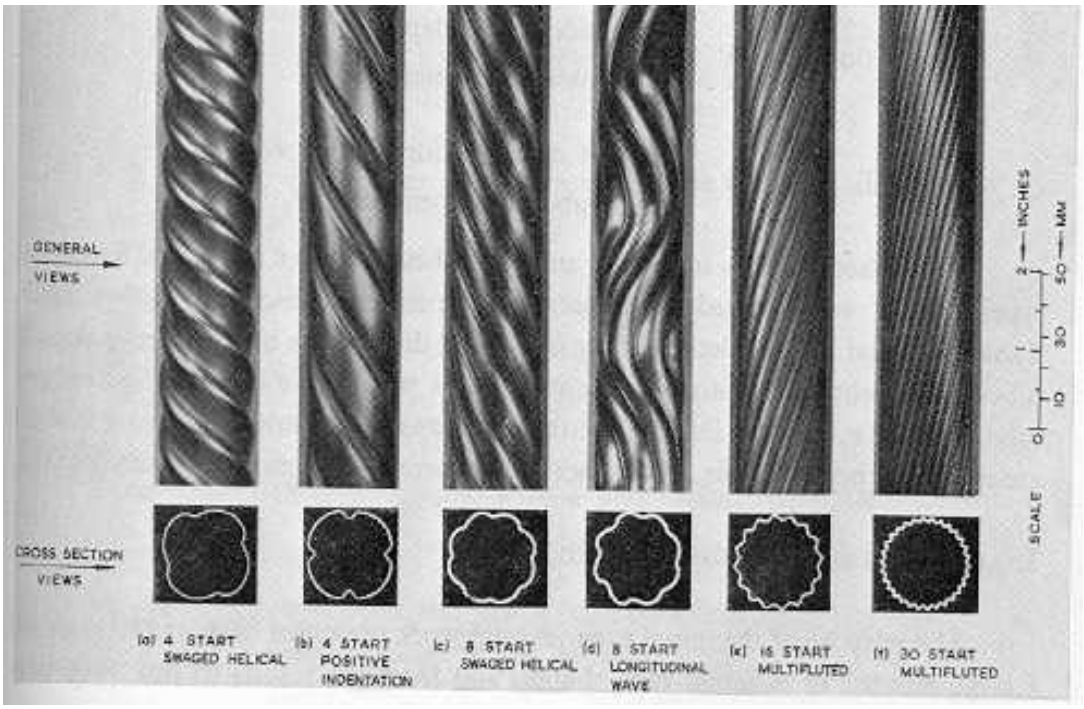

Figure 8. Tubes Tested by Newson and Hodgson (1974).

For tube types a, b, and c, Newson and Hodgson (1974) proposed a model based on the swirl flow theory. This "model assumes that the fluid flowing within the tube follows exactly the spiral path of the indentations." As a result, the distance traveled by the fluid is *L/(cos α)*, and the resulting velocity is *V/(cos α)*. By utilizing this assumption in the Dittus-Boelter equation, Newson and Hodgson (1974) postulated that:

$$\frac{h}{h_p} = \frac{1}{(\cos\alpha)^{0.8}} = (1+1/H_R^2)^{0.4} \tag{35}$$

where H_R is defined as the "helix ratio" and is equal to *(pNs)*/perimeter. In a similar manner, the Blasius equation for the friction factor gave:

$$\frac{f}{f_p} = \frac{1}{(\cos\alpha)^{2.75}} = (1+1/H_R^2)^{1.38} \tag{36}$$

Newson and Hodgson (1974) plotted experimental values of h/h_p and f/f_p versus the factors derived in equations (35) and (36), respectively. In the case of the heat transfer coefficient, most experimental results lay within 12% of the ones predicted by the swirl flow model. The swirl flow model disagreed with experiment for two tubes with the shortest helix ratios (highest helix angles). The authors stated that the reason for the disagreement could be that at higher helix angles (H_R less than 0.4), the fluid tends to spill over the indentations rather than following them.[†] For such tubes, the indentations act as roughness to the flow and the swirl flow model cannot be applied. In addition, based on the results from the 4-start and 8-start tubes, Newson and Hodgson (1974) argued that the number of starts has no influence on the applicability of the swirl flow model.

For the pressure drop data, the agreement between experiment and theory was not very good. The discrepancy between experiment and prediction increased with increasing helix angle (decreasing helix ratio) suggesting that real flow had little relevance with the swirl flow model. The pressure drop results tended to confirm the fact that flow spills over indentations at large helix angles. In the authors' opinion, the swirl flow model failed to account for the effect of the indentation ratio (e/D). To show this effect, the authors plotted the variation of h/h_p and f/f_p versus e/D_h. The trend was increasing h/h_p and f/f_p with increasing indentation ratio. In addition, this increase was directed toward the swirl flow model values. Therefore, the authors postulated that the effect of

[†] This statement is in agreement with the theories postulated by different authors in previously cited literature.

indentations is to direct the flow into a more truly swirling mode as the height of the indentation increases.

With the gathered data, Newson and Hodgson (1974) obtained an empirical correlation for the pressure drop, which predicted all but four data points within 14%:

$$\frac{f}{f_p} = 1 + 6.0647 \frac{(e/D_h)^{0.73864 - 0.1948\times10^{-6}\,\mathrm{Re}}}{H_R^{1.815}} \tag{37}$$

Equation (37) is valid for tubes of type a, b, and c, and for $0.4 < H_R < 3.0$.

In their article about tubes with spiral sheet intensifiers (single-start spiral fin), Migai and Uporov (1979) went beyond the swirl flow theory of Newson and Hodgson (1974). Migai and Uporov (1979) based their derivation on the fact that in the case of flow inside a helically-finned tube, part of the stream is swirled, while the rest is separated from the upper end of the spiral. Furthermore, based on flow visualization experiments, the authors stated that in stabilized conditions, the axial velocity field is close to uniform and the stream moves along the spiral. However, the fraction of separated flow increased with a decrease in fin pitch. The authors also noted a 30-50% increase in levels of turbulence.

The basis for Migai and Uporov's (1979) analysis was to resolve the velocity vector of the stream flowing onto the spiral into two components. $V_{||}$ was the component parallel to the spiral ($V_{||} = V^{*}\cos\alpha$) and $V\perp$ perpendicular to the spiral ($V\perp = V^{*}\sin\alpha$). $V_{||}$ represents the stream swirling, and $V\perp$ provides for stream separation. For $\alpha = 0°$, rectilinear non-separation flow is achieved, and for $\alpha = 90°$ purely separation flow is obtained. The next step in the modeling was to use superposition of Nusselt numbers determined for the swirling motion and the separation component. Nu_{swirl} was determined

by coupling the Dittus-Boelter equation with a mixing component [Migai (1966)]. Nu_{sep} was obtained by looking at the kinetic energy of the flow at the reattachment point past a transverse plate. The derivation and the resulting formulas are lengthy so the reader is referred to Migai and Uporov (1979) for further details.

Migai (1968) gave a fairly qualitative discussion of flow behavior in single-start helically-finned tubes and helically-indented tubes. Migai (1968) indicated that pressure losses are governed by friction of the swirled flow, separation of vortices from the edge of the fin, as well as formation of vortices behind the fin. Furthermore, depending on the *e/D* ratio, a fraction of the flow follows the helix of the fin and interacts with the rectilinearly-moving portion of the flow near the axis. Intensive shear vortices take place at the interface. Migai (1968) noticed that the measured friction factor was highly depended on *Re*, differing from flow in very rough tubes, where the process is governed by separated flows mainly. Therefore, Migai (1968) concluded that the strong dependence of *f* on *Re* indicates that the fraction of separated flows is small and the process is mainly governed by the friction of the swirling flow.

Another analysis of helically-finned tubes was published by Belyakov et al. (1989). This study tested 13 tubes with helical fins of different cross-sections. A method similar to that of Migai and Uporov (1979) was employed to model friction and heat transfer characteristics of the flow. The mean velocity was resolved into a parallel and perpendicular component, $V_{||}$ and $V\perp$, respectively. The principle of superposition of effects was used to add losses due to (1) friction, (2) swirling of the flow, and (3) separation of the flow around the fins.

For frictional resistance factor, Belyakov et al. (1989) proposed the following pressure drop equation:

$$\Delta P_{friction} = 2 f_{friction} \rho V_{\parallel}^2 \frac{L_{equivalent}}{D_h} = 2 f \rho V^2 \frac{L}{D_h} \tag{38}$$

Since $f = \dfrac{0.079}{\left(\dfrac{V_{\parallel} D_h}{\nu}\right)^{0.25}}$ (the plain-tube Blasius equation) and $L_{equivalent} = L / \cos(\alpha)$ [†], then:

$$f = f_{friction} \cos^{3/4}(\alpha) \tag{39}$$

Belyakov et al. (1989) argued that the centrifugal force caused by the swirling flow ejects the slow portion of the boundary layer up the sides of the fin and into the core of the flow causing additional turbulence and exchange of momentum. Based on that hypothesis, as well as the 1/7th power-law velocity profile, the additional friction coefficient due to vortex mixing was given as:

$$4 f_{vortex.mixing} = \frac{0.180}{\mathrm{Re}} \frac{D}{p N_s} \left[1125 \ln\left(\frac{\mathrm{Re}\sqrt{4 f_p + 4 f_{vortex.mixing}}}{2} - 3170 \right) \right] \tag{40}$$

The resistance factor was the sum of the friction factor and the vortex mixing factor: $f = f_{friction} + f_{vortex.mixing}$.

In addition to the resistance factor due to vortex mixing and friction at the wall, Belyakov et al. (1989) suggested the incorporation of a separation factor caused by the component of velocity that is perpendicular to the fin, $V\perp$. To account for the separation coefficient, the following pressure drop equation was proposed:

[†] As in the swirl flow model of Newson and Hodgson (1974).

$$\Delta P_{separation} = 2 f_{separation} \rho V_{\perp}^2 \frac{L}{D} = 2 f_{separation} \rho V^2 \sin^2(\alpha) \frac{L}{D} \tag{41}$$

Belyakov et al. (1989) stated that "at present, $f_{separation}$ can be found only experimentally" and that "it depends on form of the fins and their number." The overall resistance factor was thus

$$f = (f_{friction} + f_{vortex.mixing}) \cos^{3/4}(\alpha) + f_{separation} \sin^2(\alpha) =$$
$$= \left[\frac{0.079}{\left(\frac{V_{\parallel} D_h}{\nu} \right)^{0.25}} + f_{vortex.mixing} \right] \cos^{3/4}(\alpha) + f_{separation} \sin^2(\alpha) \tag{42}$$

Through experiment, Belyakov et al. (1989) correlated the overall resistance coefficient with the following equation:

$$4f = 0.115 \frac{\left[\sqrt[3]{\left(\frac{D-2e}{p \sin(\alpha)} \right)^2} \log\left(\frac{p \sin(\alpha) - t}{e} \right) \right]^2}{\left[\log\left(\frac{D}{e} \right) \right]^2} \tag{43}$$

A Nusselt number analysis was performed with the same approach as the overall resistance coefficient analysis. The components due to flow twist and flow separation were added to account for the overall Nusselt number. The component due to flow twist was determined as the sum of $Nu_{friction}$ and $Nu_{vortex.mixing}$. The Nusselt number due to friction was calculated from the formula for smooth tubes with the introduction of the parallel component of velocity:

$$Nu_{friction} = 0.023 \,\mathrm{Re}^{0.8} \,\mathrm{Pr}^{0.4} \cos^{0.8}(\alpha) \tag{44}$$

To account for $Nu_{vortex.mixing}$, Belyakov et al. (1989) used the equation derived by Migai (1966). The value of the Nusselt number due to separation was determined from the

following scheme. Part of the heat transfer occurs from the top of the fin, where the Nusselt number can be derived from a flat plate correlation. Another portion of heat transfer occurs from the depression, where the Nusselt number can be approximated based on the results of Migai (1968). The plate and depression Nusselt numbers can be approximated with the following equations:

$$Nu_{plate} = 0.036\,\mathrm{Re}^{0.8}\,\mathrm{Pr}^{0.4}(D_h/t)^{0.2}\sin^{0.8}(\alpha) \tag{45}$$

$$\begin{aligned} Nu_{depression} &= 100\left(\tfrac{2e}{D}\right)^{0.445} \times 0.0216\,\mathrm{Re}^{0.8}\,\mathrm{Pr}^{0.445}\sin^{0.8}(\alpha) \quad \text{for } \tfrac{2e}{D} < 0.07 \\ Nu_{depression} &= 100(0.07)^{0.445} \times 0.0216\,\mathrm{Re}^{0.8}\,\mathrm{Pr}^{0.445}\sin^{0.8}(\alpha) \quad \text{for } \tfrac{2e}{D} \geq 0.07 \end{aligned} \tag{46}$$

The overall *Nu* due to separation was thus:

$$\begin{aligned} Nu_{separation} &= \frac{tNu_{plate} + [p\sin(\alpha) - t]Nu_{depression}}{p\sin(\alpha)} = \\ &= \frac{t}{p\sin(\alpha)} 0.036\,\mathrm{Re}^{0.8}\,\mathrm{Pr}^{0.4}(D_h/t)^{0.2}\sin^{0.8}(\alpha) + \\ &+ \frac{p\sin(\alpha) - t}{p\sin(\alpha)} 100\left(\tfrac{2e}{D}\right)^{0.445} 0.0216\,\mathrm{Re}^{0.8}\,\mathrm{Pr}^{0.445}\sin^{0.8}(\alpha) \end{aligned} \tag{47}$$

where $\frac{t}{p\sin(\alpha)}$ is the proportion of the length of protrusion and $\frac{p\sin(\alpha) - t}{p\sin(\alpha)}$ is the proportion of the length of depression.

Jensen and Vlakancic (1999) tested fifteen helically-finned tubes with a wide range of helix angles (0° - 45°), *e/D* ratios (0.0075 - 0.085), number of starts (8 - 54), and fin widths (0.62 mm - 1.84 mm). However, experimental data of only six tubes were reported. Isothermal friction factor tests were conducted with water and ethylene glycol, and the heat transfer tests were executed in both heating and cooling modes. Jensen and Vlakancic (1999) stated that, generally, the friction factor increased with increasing N_s, α,

and *e/D*; however, a large fin thickness can cause the flow to stall in between the fins, reducing the friction factor. Similar conclusions were drawn from the behavior of the Nusselt number. Jensen and Vlakancic (1999) attempted to predict their experimental data with correlations of Carnavos (1980) with a poor outcome. Data of only a few tubes fell within 10% of the predicted values. Jensen and Vlakancic (1999) attributed this discrepancy to the existence of two types of flows in spirally-finned tubes. The first type of flow occurs inside tubes with tall fins, few starts, and relatively small helix angles (less than 30°). In this type of flow, the fluid follows the space in between the fins (swirl flow). The second type of flow takes place in tubes with shorter fins (when $e/D \leq 0.02$, the authors refer to micro-fin tubes), more fin starts and higher helix angles. According to the authors, the second type of flow is prone to coring[†] with possible relaminarization in the interfin regions. Jensen and Vlakancic (1999) stated that since the governing physics are different in different helically-finned tubes, existing correlations are usually limited to the type of tube that was used for their development.

To predict the characteristics of the two flow patterns Jensen and Vlakancic (1999) developed two sets of correlations. The first set, for friction factors in tall-fin tubes, is as follows:

$$\frac{f}{f_p} = \left(\frac{l_{csw}}{D}\right)^{-1.25} \left(\frac{\pi D^2/4}{\pi D^2/4 - N_s e t}\right)^{1.75} \tag{48}$$

$$\frac{l_{csw}}{D} = \frac{l_c}{D}\left[1 - 0.203 p_{\text{modified}}{}^{0.65} (2e/D)^{0.20}\right] \tag{49}$$

[†] Coring occurs when the interfin region poses such a resistance to the flow that the main portion of the flow is constrained to the core of the tube, skimming over the fins.

$$\frac{l_c}{D} = \frac{\pi^{D^2}\!/_4\,(1-2e/D)^2}{\pi^{D^2}\!/_4 - N_s e t}\left(1-2e/D\right) + \left[1 - \frac{\pi^{D^2}\!/_4\,(1-2e/D)^2}{\pi^{D^2}\!/_4 - N_s e t}\right]\left[\frac{\pi}{N_s}\left(1-e/D\right) - \frac{t}{D}\right] \quad (50)$$

where $p_{modified} = N_s \cdot sin\alpha/\pi$ is the non-dimensional fin pitch. The Nusselt number for tall-fin tubes is expressed with:

$$\frac{Nu}{Nu_p} = \left(\frac{l_{csw}}{D}\right)^{-1/2}\left(\frac{\pi^{D^2}\!/_4}{\pi^{D^2}\!/_4 - N_s e t}\right)^{0.8} \cdot func(geometry) \quad (51)$$

$$func(geometry) = \left(\frac{L\pi^{D^2}\!/_4}{A_{actual}}\right)^{0.29}\left[1 - 1.792\, p_{\text{modified}}{}^{0.64}\,(2e/D)^{2.76}\,\text{Re}^{0.27}\right] \quad (52)$$

where A_{actual} is the actual inside surface are of the tube. For micro-fin tubes, Jensen and Vlakancic (1999) proposed:

$$\begin{aligned} \frac{l_{csw}}{D} &= \left[1 - 1.577\, p_{\text{modified}}{}^{0.64}\,(2e/D)^{0.53}\left[(\pi/N_s - t/D)\cos\alpha\right]^{0.28}\right] \text{ for } \text{e/D} \le 0.02 \\ \frac{l_{csw}}{D} &= \left[1 - 0.994\, p_{\text{modified}}{}^{0.89}\,(2e/D)^{0.44}\left[(\pi/N_s - t/D)\cos\alpha\right]^{0.41}\right] \text{ for } 0.02 < \text{e/D} \le 0.03 \end{aligned} \quad (53)$$

valid for Re ≥ 20 000, and

$$func(geometry) = \left(\frac{L\pi^{D^2}\!/_4}{A_{actual}}\right)^{0.29}\left[1 - 0.059\, p_{\text{modified}}{}^{-0.31}\left[\left(\frac{\pi}{N_s} - \frac{t}{D}\right)\cos\alpha\right]^{-0.66}\right] \quad (54)$$

The above correlations predicted most of Jensen and Vlakancic (1999) data within 15%. Jensen and Vlakancic (1999) also evaluated their correlations with other data [e.g., Carnavos (1980)], and the results were good.

An experiment performed by Han et al. (1978) tested a parallel-plate channel with ribs on both sides. The ribs were placed symmetrically or in a staggered arrangement. During the test, one of the variables was the angle of attack of the air flowing in the channel, which can be compared to a helix angle for air flowing inside a spirally-finned

tube. Thus, the results can be a good indicator of flow behavior in helically-finned tubes. In addition to the angle of attack, the investigators varied the rib height to hydraulic diameter ratio, the rib spacing to rib height ratio, and the rib included angle.

Han et al. (1978) presented conclusions about each variable they investigated. These conclusions were as follows:

1) Rib height to hydraulic diameter: As e/D_H increased, the friction factor increased. For different values of e/D_H, the fully-rough regime started at different *Re* numbers.
2) Rib cross-section. The larger the rib included angle, the smaller the friction factor. The effect of included angle on heat transfer was modest.
3) Rib pitch to height ratio. For *p/e* less than 10, skimming flow occurred (the flow did not reattach before it reached the succeeding rib). For *p/e* value of about 10 the flow reattached close to the next rib causing the friction factor and the *St* number to be the highest. For larger rib spacings, the reattachment point was reached before the succeeding rib and a boundary layer began to grow. The average shear stress and heat transfer were greatly reduced.
4) Flow attack angle. As the angles of attack changed from 90° to 45°, *St* decreased only 5%. The friction factor decreased with attack angle "because the form drag, which makes no contribution to the heat transfer, is being reduced." The authors claimed that the optimum attack angle is 45° because the viscous sublayer is still broken up

while the form drag is reduced. As the angle of attack was decreased further, smooth tube performance was approached.

Han et al. (1978) presented the following correlations for friction and heat transfer:

$$R = \frac{5.4(e+/35)^m}{(\frac{10}{p/e})^n (\frac{90-\beta/2}{90})^{0.32} (\frac{\alpha}{45})^{0.52}} \tag{55}$$

where

m = -0.36 for $e+ < 35$

m = 0 for $e+ \geqslant 35$

n = -0.12 for $p/e < 10$

$n = 0.49(\alpha/90)^{0.84}$ for $p/e \geqslant 10$

and

$$G(0.72/\mathrm{Pr})^{0.57} = 10.48(e+/35)^i (\alpha/45)^j \tag{56}$$

where

i = 0 for $e+ < 35$

i = 0.27 for $e+ \geqslant 35$

j = -0.43 for $\alpha \geqslant 45°$

j = 0.48 for $\alpha < 45°$

The definition of R for flow in a parallel plate channel differs from equation (2) and is given by

$$R = \sqrt{2/f} + 2.5\ln(2e/D_h) + 4.23 \tag{57}$$

All of the studies presented so far were conducted on turbulent flow of water or air. Laminar flow is not in the scope of this dissertation. However, laminar flow can be of practical importance to chemical engineers who deal with highly viscous fluids such as oil, ethylene glycol, or liquid polymers. Those readers should refer to Shome (1995) for a more detailed review of investigations on laminar flow in helically-finned tubes.

II.B Numerical Approach

The numerical approach has advantages and disadvantages. The disadvantages are that (1) experimental results are needed to verify most numerical models and algorithms and (2) numerical modeling is available to a limited number of engineers with access to computing power. One of the advantages is that once a numerical model is proven, parametric studies and optimization can be easily performed without the need of an elaborate (and often expensive) experimental program.

Based on the literature survey, there are few publications that present numerical solutions of laminar or turbulent flow in helically-finned tubes. Laminar flow is easier to model because there is no problem of closure[†] of the transport equation. Nonetheless, as the state of the art in the area of turbulence modeling evolves, the problem of turbulent flow in helically-finned tubes is likely to be understood better.

Date (1974) introduced an interesting mathematical concept, useful in modeling of flow in spirally-finned tubes. Date (1974) presented a numerical solution for friction and heat transfer characteristics of flow in a tube containing a twisted tape insert (Figure 9). Date's (1974) model was based on the use of rotating cylindrical coordinates, in

[†] An explanation of closure is given later in the section.

which the angular coordinate is always measured from the surface of the tape. The rotating coordinate system is related to the stationary one by the following transformations:

$$\begin{aligned} r' &= r \\ z' &= z \\ \theta' &= \theta + \pi z / H \end{aligned} \tag{58}$$

where H is the pitch for 180° rotation of the twisted tape insert. With the equations above, the following relations can be formulated:

$$\begin{aligned} \frac{\partial}{\partial r} &= \frac{\partial r'}{\partial r}\frac{\partial}{\partial r'} + \frac{\partial z'}{\partial r}\frac{\partial}{\partial z'} + \frac{\partial \theta'}{\partial r}\frac{\partial}{\partial \theta'} = \frac{\partial}{\partial r'} \\ \frac{\partial}{\partial z} &= \frac{\partial r'}{\partial z}\frac{\partial}{\partial r'} + \frac{\partial z'}{\partial z}\frac{\partial}{\partial z'} + \frac{\partial \theta'}{\partial z}\frac{\partial}{\partial \theta'} = \frac{\partial}{\partial z'} + \frac{\pi}{H}\frac{\partial}{\partial \theta'} \\ \frac{\partial}{\partial \theta} &= \frac{\partial r'}{\partial \theta}\frac{\partial}{\partial r'} + \frac{\partial z'}{\partial \theta}\frac{\partial}{\partial z'} + \frac{\partial \theta'}{\partial \theta}\frac{\partial}{\partial \theta'} = \frac{\partial}{\partial \theta'} \end{aligned} \tag{59}$$

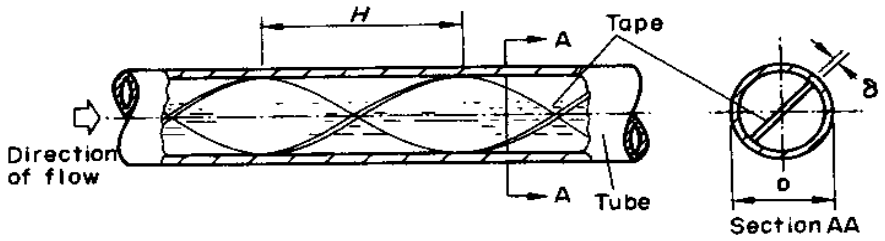

Figure 9. Configuration Analyzed by Date (1974).

With the derivative relations available, Date (1974) transformed the transport equations from stationary to rotating cylindrical coordinates and applied the mathematical inference of fully-developed flow:

$$\frac{\partial}{\partial z'} = 0 \tag{60}$$

for all variables, except temperature and pressure. The derivatives of pressure and temperature in the *z'* direction are treated as known values. Hence, the transport equations in the *r'*, *θ'*, and *z'* are as follows:

Continuity equation

$$\rho\left[\frac{1}{r'}\frac{\partial(r'V_r)}{\partial r'}+\frac{1}{r'}\frac{\partial}{\partial\theta'}\left(V_\theta+\frac{\pi r'}{H}V_z\right)\right]=0 \tag{61}$$

Axial momentum equation

$$\begin{aligned}\rho\left[V_r\frac{\partial V_z}{\partial r'}+\left(\frac{V_\theta}{r'}+\frac{\pi}{H}V_z\right)\frac{\partial V_z}{\partial\theta'}\right]&=-\left[\frac{\partial\overline{P}}{\partial z'}+\frac{\pi}{H}\frac{\partial P_0}{\partial\theta'}\right]+\\ -\left[\frac{1}{r'}\frac{\partial}{\partial r'}(r'\tau_{r,z})+\frac{1}{r'}\frac{\partial}{\partial\theta'}(\tau_{\theta,z})+\frac{\pi}{H}\frac{\partial}{\partial\theta'}(\tau_{z,z})\right]&\end{aligned} \tag{62}$$

Tangential momentum equation

$$\begin{aligned}\rho\left[V_r\frac{\partial V_\theta}{\partial r'}+\left(\frac{V_\theta}{r'}+\frac{\pi}{H}V_z\right)\frac{\partial V_\theta}{\partial\theta'}+\frac{V_rV_\theta}{r'}\right]&=-\frac{1}{r'}\frac{\partial P_0}{\partial\theta'}+\\ -\left[\frac{1}{r'^2}\frac{\partial}{\partial r'}(r'^2\tau_{r,\theta})+\frac{1}{r'}\frac{\partial}{\partial\theta'}(\tau_{\theta,\theta})+\frac{\pi}{H}\frac{\partial}{\partial\theta'}(\tau_{\theta,z})\right]&\end{aligned} \tag{63}$$

Radial momentum equation

$$\begin{aligned}\rho\left[V_r\frac{\partial V_r}{\partial r'}+\left(\frac{V_\theta}{r'}+\frac{\pi}{H}V_z\right)\frac{\partial V_r}{\partial\theta'}-\frac{V_\theta^2}{r'}\right]&=-\frac{\partial P_0}{\partial r'}+\\ -\left[\frac{1}{r'}\frac{\partial}{\partial r'}(r'\tau_{r,r})+\frac{1}{r'}\frac{\partial}{\partial\theta'}(\tau_{r,\theta})-\frac{\tau_{\theta,\theta}}{r'}+\frac{\pi}{H}\frac{\partial}{\partial\theta'}(\tau_{r,z})\right]&\end{aligned} \tag{64}$$

Energy equation

$$\begin{aligned}\rho\left[V_r\frac{\partial T}{\partial r'}+\left(\frac{V_\theta}{r'}+\frac{\pi}{H}V_z\right)\frac{\partial T}{\partial\theta'}\right]&=-\rho V_z\frac{\partial T}{\partial z'}+\\ -\left[\frac{1}{r'}\frac{\partial}{\partial r'}(r'q_r)+\frac{1}{r'}\frac{\partial}{\partial\theta'}(q_\theta)-\frac{\pi}{H}\frac{\partial}{\partial\theta'}(q_z)\right]&\end{aligned} \tag{65}$$

In the above equations, the pressure consists of two terms: an average term at a given z location and a cross-section variation term:

$$P(r', z', \theta') = \overline{P}(z') + P_0(r', \theta') \tag{66}$$

With the fully-developed flow assumption, and the fact that $\partial \overline{P} / \partial z'$ and $\partial T / \partial z'$ are known, V_r, V_θ, V_z, and T are functions of r' and θ' only. When information about stresses and heat fluxes (τ's and q's) is specified, the mathematical statement of the transport equations is complete.

For laminar flow, the coupling between τ and the velocity gradients is achieved via viscosity, μ, and between q and the temperature gradients via diffusivity, Γ. For turbulent flow, the approach is to replace μ and Γ with effective values $\mu_{eff} = \mu + \mu_{turb}$ and $\Gamma_{eff} = \Gamma + \Gamma_{turb}$. Moreover, research has shown that [Kays and Crawford (1980)]:

$$\mathrm{Pr}_{eff} = \frac{\mu_{eff}}{\Gamma_{eff}} \approx 0.9 \tag{67}$$

The above definition eliminates the need to know Γ_{eff}. Nonetheless, information about μ_{turb} still needs to be provided. The term μ_{turb} is not a fluid property but rather a property of the flow pattern. Therefore, details about μ_{turb} must come from experiments. Providing an equation for μ_{eff} is referred to as "closure" of the turbulent Navier-Stokes equations. For years, closure has been the most difficult step in solving a turbulent flow problem. A detailed description of the closure and solution procedure used by Date (1974) is beyond the scope of this dissertation.

In his doctoral dissertation, Ivanović (1978) presented solutions to three scenarios: (1) turbulent flow and heat transfer in longitudinally-finned tubes, (2) turbulent flow and heat transfer in longitudinally-finned annuli, and (3) laminar flow and heat

transfer in helically-finned tubes. The simplifying assumptions were fully-developed flow with constant properties, zero fin thickness, and 100% fin efficiency. The longitudinal fin problem was solved with two different turbulence models. The first approach was a modified mixing-length model that consisted of a superposition of a mixing length for a channel and a mixing length for a plain tube. The second approach was a low *Re* k-ε model. Both approaches yielded satisfactory results.

The helical fin problem was solved using Date's (1974) rotating coordinate system. The coordinate system transformation results in converting a 3-D problem into a 2-D one. Ivanović (1978) further simplified the equations by limiting his analysis to small helix angles (i.e., $\alpha < 17°$). The number of starts was varied from 4 to 24 and the dimensionless fin height *2e/D* from 0.2 to 0.8. The computational domain used is shown in Figure 10. The boundary conditions consisted of the wall-temperature and no-slip condition applied at surfaces BC, CD, and CE. The condition for surfaces AB and AE was that the velocities, pressures, and temperatures are equal at corresponding *r*'s.

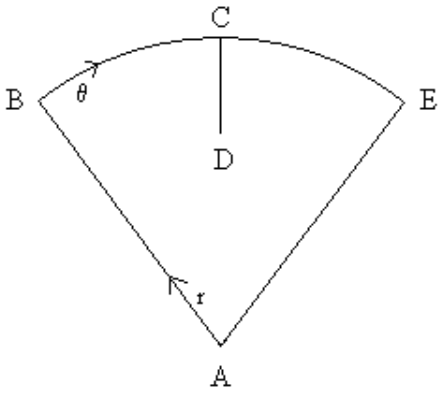

Figure 10. Computational Domain of Ivanović (1978).

Ivanović (1978) postulated several remarks based on the results of his computation:

1) The helix angle seemed to have no effect on the friction factor and Nusselt number for the values of $tan(\alpha)Re$ less than 100. Past this value of $tan(\alpha)Re$, Nu and f increased steeply.
2) f and Nu increased with increasing fin height.
3) The helix angle ceased to have any effect on f and Nu for large number of starts ($N_s = 18$).
4) $f/f_{longitudinal}$ continuously decreased with increasing N_s. This was because as the interfin region became narrower, secondary flows were diminished.
5) $f/f_{longitudinal}$ increased with increasing fin height. This increase was steep for tubes with small number of fins and rather small and uniform for tubes with large number of fins.
6) By analyzing the efficiency indices and local heat transfer coefficients, Ivanović (1978) claimed that "the economical effect of fin-twisting is associated only with longer fins."

The coordinate system transformation developed by Date (1974) was also used by Shome and Jensen (1996b) to model variable-viscosity, mixed-convection laminar flow in helically-finned tubes at $100 < Re < 1000$. Numerical results were verified with experimental data obtained by Shome and Jensen (1996a). The numerical model assumed:

- steady laminar flow,

- negligible viscous dissipation and axial conduction in tube wall, fin, and fluid,
- 100% fin efficiency,
- applicability of the Boussinesq approximation, constant fluid thermal conductivity and specific heat but variable viscosity, and
- the uppermost fin at the inlet being always aligned with the gravity vector.

The included angle of the fin was fixed at 3°. Shome and Jensen's (1996b) model was more realistic than that of Ivanović's (1978) because the fins had a finite thickness and an included angle, flow was developing, natural convection was taken into account, and there was no small helix angle assumption.

The code was validated for a longitudinal fin setup against the results of other researchers. The grid independence was successfully tested by refining the mesh and observing the change in final results. The agreement between measured [Shome and Jensen (1996a)] and predicted values for the isothermal friction coefficient and Nusselt number was well within 10%. The Nusselt number analysis revealed that neglecting free convection could lead to an underprediction of Nu by up to 47% (especially at low Re). On the other hand, computation of the diabatic friction factor revealed that the error in f is more affected by the neglect of variable viscosity effect than by the neglect of free convection effects.

Shome and Jensen (1996b) also performed a parametric study by varying the geometric parameters $0.03 \leq 2e/D \leq 0.1$, $8 \leq N_s \leq 54$, and $0 \leq \alpha \leq 45°$ and the operating

conditions $100 \leq Re \leq 1000$, $50 \leq Pr \leq 1000$, $0 \leq Ra \leq 10^6$, and -30 K $\leq (T_{wall} - T_{in}) \leq 30$ K. The authors concluded the following:

1) In the developing region, the Nusselt numbers were considerably higher for enhanced tubes than for the smooth tube.
2) Once the flow was developed, and the swirling flow gained strength, Nusselt numbers increased with increasing helix angles.
3) At large distances from the tube entrance, the Nusselt numbers of the enhanced tubes lay below those of a smooth tube by as much as 15-20 percent, probably due to coring of the fluid.
4) Friction factors for enhanced tubes were up to 25% higher than those of a smooth tube.
5) The effect of helix angle on the friction factors was negligible.
6) In the entrance region, the Nusselt numbers increased with increasing number of starts.
7) Once the flow was fully-developed, the change in Nu due to a change in N_s was marginal.
8) Diabatic friction factors increased by 7-10% when N_s increased from 14 to 30 and by 2-3% when N_s further increased to 54.
9) In the entrance region, increasing the fin height from $2e/D = 0.03$ to 0.1 increased the Nusselt numbers by up to 45%. However, in the developed region, the same change in $2e/D$ had little effect on Nu.
10) Contrary to the Nusselt number behavior, the effect of dimensionless fin height on friction factor was more uniform throughout the entrance

and developed regions. Increasing *2e/D* from 0.03 to 0.1 increased *f* by about 25-30 percent.

11) Coring was a strong proportional function of the number of fins.

12) For tubes with large number of fins, heat transfer in the interfin region was low (even lower than for a plain tube) due to low velocity of the fluid adjacent to fin walls.

Perhaps the most advanced numerical analysis of flow in helically-finned tubes was that of Kim et al. (2004). The most important aspect of the Kim et al. (2004) study was that the numerical flow simulation was carried out in the turbulent regime. Kim et al. (2004) did not use the helical coordinate system of Date (1974) because their goal was to develop computational tools that were applicable to a wide range of internal flows. Instead, the azimuthal symmetry of the cross section was used to implement a periodic boundary condition, thus simplifying the computational domain. Kim et al. (2004) used three different types of mesh models along with four different turbulence models [i.e., the model of Spalart and Allmaras (1992), shear stress transport model of Menter (1994), k-ε model of Goldberg et al. (1998), and the k-ε model of Lam and Bremhorst (1981)] to solve a set of Reynolds averaged Navier-Stokes (RANS) equations for flow inside two different spirally-finned tubes. The first tube had 8 fin starts, D = 23.64 mm, α = 30°, e/D = 0.05, and t = 1 mm. The second one had 30 fin starts, D = 24.2 mm, α = 30°, e/D = 0.015, and t = 0.64 mm. Numerical results were compared to the experimental data of Jensen and Vlakancic (1999). For the first tube, friction factors and Nusselt numbers were within 13% and 11% of the experiment, respectively. The solution to the second tube problem converged with the Goldberg et al. (1998) model only, suggesting perhaps

its superiority for multiple-wall geometry. Numerical results for the second tube case with the Goldberg model were within 7.6% of the experiment for the friction factor and 10% for the Nusselt number. Velocity visualizations of Kim et al. (2004) are shown in Figure 11.

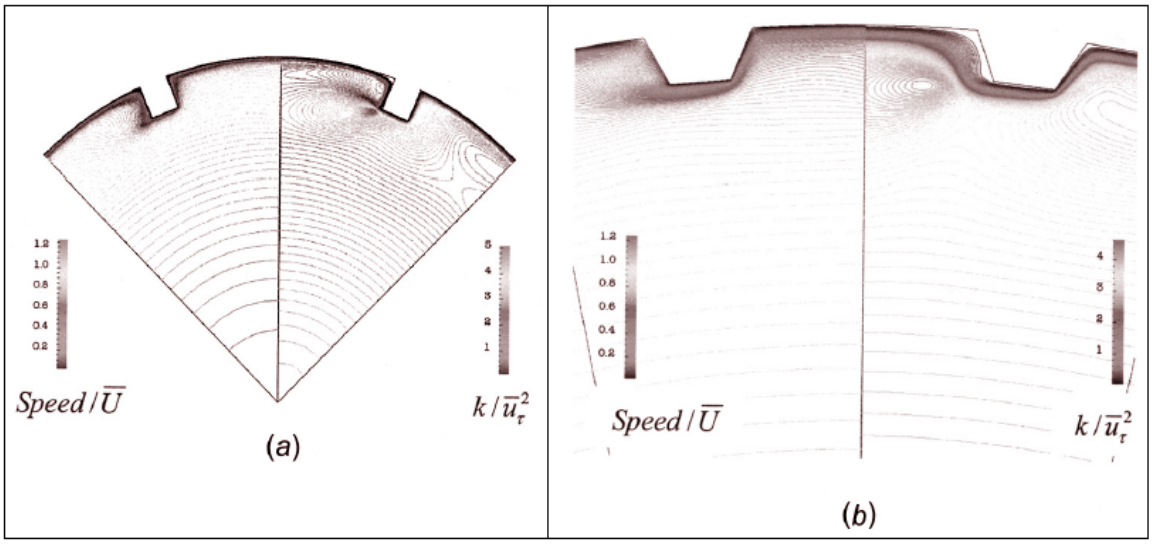

Figure 11. Flow Visualizations of Kim et al. (2004): (a) Non-dimensional speed and turbulent kinetic energy for the 8-start tube at *Re* = 36 000, (b) Non-dimensional speed and turbulent kinetic energy for the 30-start tube at *Re* = 31 796.

CHAPTER III

PRINCIPLES OF ARTIFICIAL NEURAL NETWORKS

From the information presented so far, friction and heat transfer in helically-finned tubes are governed by an intricate set of coupled and non-linear physical interactions. Therefore, obtaining a single prediction formula seems to be an unattainable goal with the knowledge engineers currently possess. Regression techniques performed on experimental data require mathematical functional form assumptions, which limit their accuracy. To achieve accuracy, techniques that can effectively overcome the complexity of the problem without dubious assumptions are needed. One of these techniques is the artificial neural network (ANN), inspired by the biological network of neurons in the brain.

Despite the complexity of the natural environment, living creatures are able to perform involved activities within their ecosystems. Animals can rapidly process vast amounts of data and make "calculated" decisions. This capability, attributed to the nervous system, is partly acquired and partly enhanced through a process called learning. Last century's advancements in bio-medical sciences have shed some light on the functioning of the nervous system. Studies in bio-medicine and psychology have always attempted to understand the brain and its elementary component - the neuron. Knowledge

gained in this topic encouraged scientists to apply the concept of a neuron to mathematics and logic, giving birth to artificial neural networks (ANNs).

The purpose of ANNs is to provide solution algorithms to complex problems such as classification, clustering, data compression, pattern association, function approximation, forecasting, control applications, or optimization[†]. To many researchers dealing with these topics, ANNs are a subject of study in themselves. The purpose of this chapter is to briefly introduce the concept of ANNs and how ANNs can be used in heat transfer and fluid problems. Readers who are interested in learning more about ANNs are encouraged to explore some of the many texts on this subject [e.g., Haykin (1994) or Mehrotra et al. (1996)].

III.A Biological and Artificial Neurons

Figure 12 shows a biological (real) neuron. A real neuron is composed of a cell body, dendrites, and a tubular axon, which terminates with end bulbs called synapses. The axon of a neuron makes synaptic connections with dendrites of many other neurons. The number of connections ranges from 100 to 100 000. A neuron receives signals from other neurons at the dendrites and transmits them down the axon to the synapses. The magnitude of the signal received by a neuron depends on the efficiency, or strength, of the synaptic connection. An electrostatic potential difference is always maintained across the cell membrane. The cell membrane becomes electrically active when sufficiently excited by signals from other neurons. The neuron fires, or sends a 100 mV signal down

[†] Heat transfer applications mostly deal with function approximation, control, and optimization. However, pattern recognition capabilities of ANNs have also been used in conjunction with flow visualization techniques to assist in unsupervised learning algorithms that develop friction, mass, and heat transfer correlations [Ashforth-Frost et al. (1995)].

its axon, if its net excitation during a certain period of time (period of latent summation) exceeds a threshold value. Firing is followed by a brief refractory period during which a neuron is inactive. The whole process can occur at frequencies of up to several hundred Hertz. It is the neuron's firing frequency that is referred to as the output of a neuron.

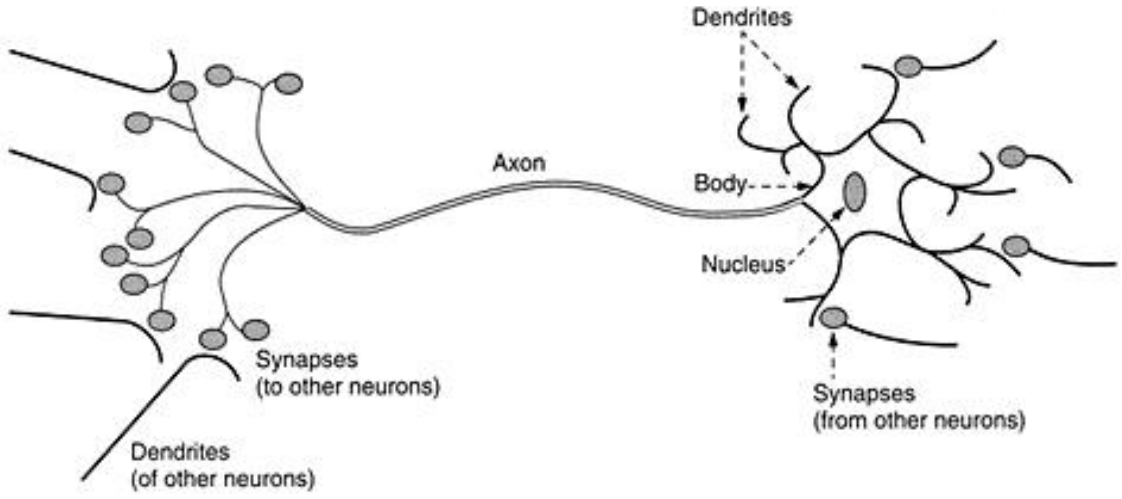

Figure 12. Biological Neuron [Mehrotra et al. (1996)].

The picture presented so far is possibly oversimplified. Axons may form synapses with other axons. A neuron may have no axon, but only "processes" that receive and transmit signals. Dendrites may form synapses with other dendrites. A neuron may have synapses with its own dendrites. Nevertheless, the above description presents the characteristics of a neuron that are relevant to ANNs.

Introduction to the artificial neuron model requires the discussion of terminology that is used in this dissertation. The equivalents between biological and artificial terms are as follows:

- neuron = node

- synapse = connection
- received signal = input
- synaptic efficiency = weight
- firing frequency = node output
- threshold = bias

The easiest way to describe an artificial neuron model is graphically. Figure 13 shows a schematic of an artificial neuron. The similarity between an artificial neuron and a real one is in the operation. Each input ($x_1, x_2, \ldots, x_n$) is multiplied by a weight and is fed into the node. The node sends an output based on some function of the weighted inputs. The differences between an artificial neuron and a real one come from the simplifying assumptions:

1) The position of the incoming connection is irrelevant.
2) Each node outputs a single value to other nodes via outgoing connections, irrespective of their positions.
3) All inputs come in at the same time or remain activated long enough for the computation of function *F* to take place.

A further simplification is to postulate that:

$$F(w_1 x_1, \ldots, w_n x_n) = F(w_1 x_1 + \ldots + w_n x_n) = F(net).$$

This assumption is supported by the fact that voltages are added across a circuit, which is what approximately happens in a brain. In order to facilitate the learning process of an artificial neuron, a bias is often added to the sum of weighted inputs. In such case, the node function really computes *F(net + bias)*, where *bias* (like *w*) is a node variable rather

than an input. Throughout the rest of this chapter, the terms *F(net)* and *F(net + bias)* are equivalent.

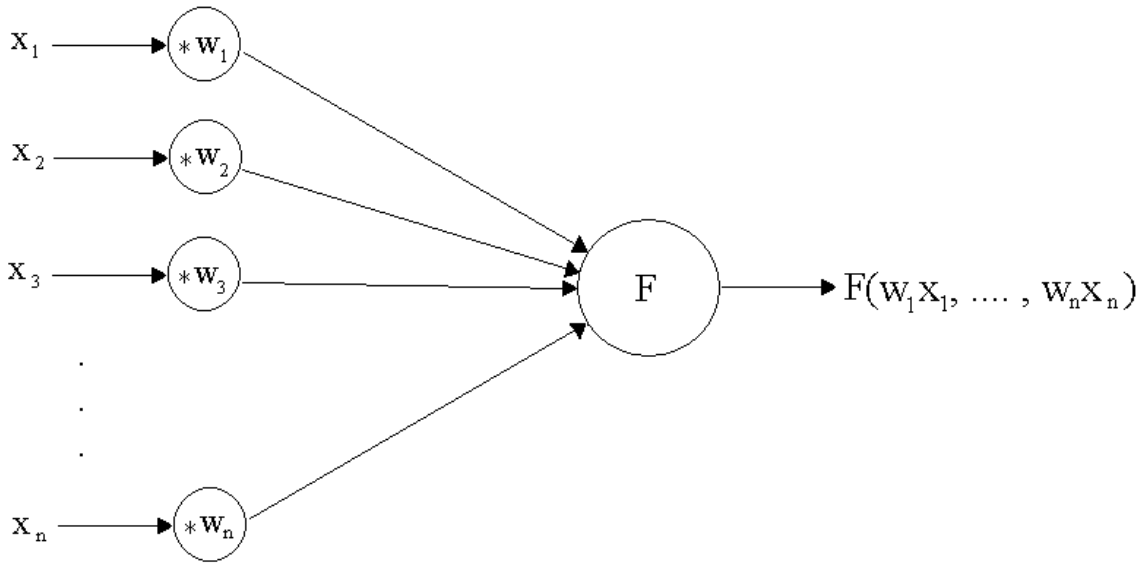

Figure 13. An Artificial Neuron.

Although applying the node function to the sum of the weighted inputs is the most common practice, there exist networks (e.g., "sigma-pi" networks) that take the product of the weighted inputs. Nevertheless, the *F(net)* approach is the most widely used and will be employed herein. The next section discusses the types of functions used within the nodes.

III.B Node Functions

There are no legitimate limitations as to the type of node function *F(net)* one can use. Obviously, the best function to use is the one that performs the job best. Experience has shown that certain function types perform well in ANNs.

III.B.1 Step Function

Figure 14 shows an arbitrary step function. This function simply outputs a value *a* if *net* is less than a threshold value *c* and a value *b* if *net* is greater than the threshold value:

$$F(net) = \begin{cases} a & \text{if} \quad net < c \\ b & \text{if} \quad net > c \end{cases}$$

The output at *net* = *c* is sometimes *a*, sometimes *b*, or the average of the two. The step function is suitable for binary applications. For example, digital processes need inputs and outputs that can be represented with only two numbers, 0 and 1.

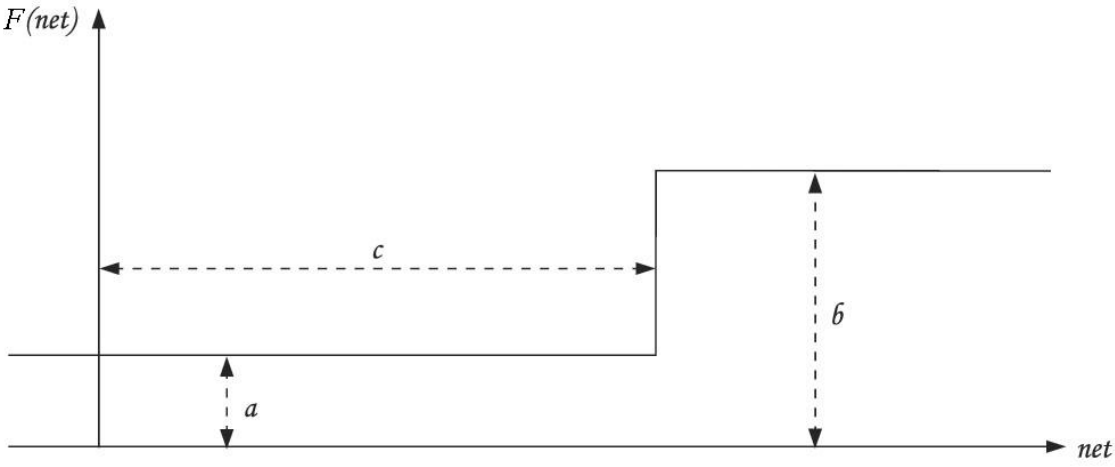

Figure 14. An Arbitrary Step Function.

Although the idea of threshold is biologically plausible, the fact that the magnitude of the input has little relevance (except for whether or not it is above the threshold) seems to be against logic. On the other hand, the output of the step function saturates, meaning that it cannot go infinitely high or low, following the idea that an infinitely high neuron firing rate is biologically impossible. A potential disadvantage of

the step function is that it is discontinuous, making it sensitive to noise. Moreover, non-differentiability of this function constrains the number of learning algorithms that can be applied to the network.

III.B.2 Ramp Function

The ramp function is an evolution of the step function that overcomes the discontinuity problem by introducing a linear "ramp" between the high and low output values. The ramp function is illustrated in Figure 15 and is defined by the following set of equations:

$$F(net) = \begin{cases} a & \text{if } net < c \\ b & \text{if } net > d \\ a + (net - c)(b - a)/(d - c) & \text{otherwise} \end{cases}$$

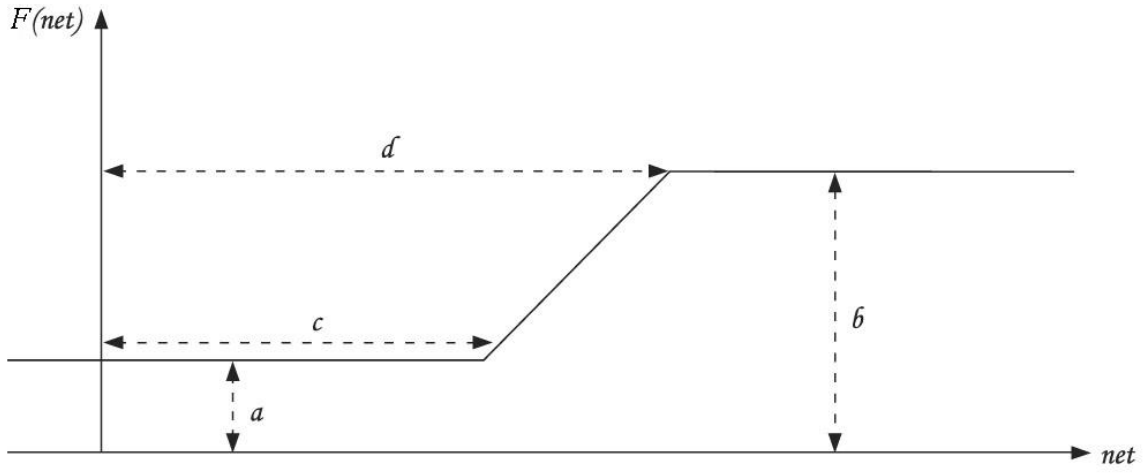

Figure 15. An Arbitrary Ramp Function.

By virtue of continuity, the ramp function has no binary attribute, but still saturates at a high and low output value. Even though the ramp function is continuous, it is non-differentiable at *net* = *c* and *net* = *d*. The ramp function is an example of a simple

piecewise linear function. More elaborate functions can be created by combining even more linear functions.

III.B.3 Sigmoid Functions

Sigmoid functions are S-shaped functions that are smooth (continuous and differentiable), symmetric about a point, and asymptotically approach a low and high value. Because of these characteristics, effective learning algorithms are easier to apply and, as a result, sigmoid functions are the most common functions in neural network applications. In addition, experimental observation suggests that the firing rate of a biological neuron is approximately a sigmoidal function of the net input [Mehrotra et al. (1996)].

An arbitrary sigmoid function is depicted in Figure 16. This function's limits are:

$$\lim_{net \to \infty} F(net) = b$$
$$\lim_{net \to -\infty} F(net) = a$$

Common choices are a = -1 or a = 0, b = 1, and c = 0. Two examples of sigmoid functions are:

$$F(net) = \frac{1}{1 + \exp(-net)} \tag{68}$$

and

$$F(net) = \tanh(net) \tag{69}$$

These two example functions can be scaled, translated, and rotated according to the application without losing the characteristics of a sigmoid function.

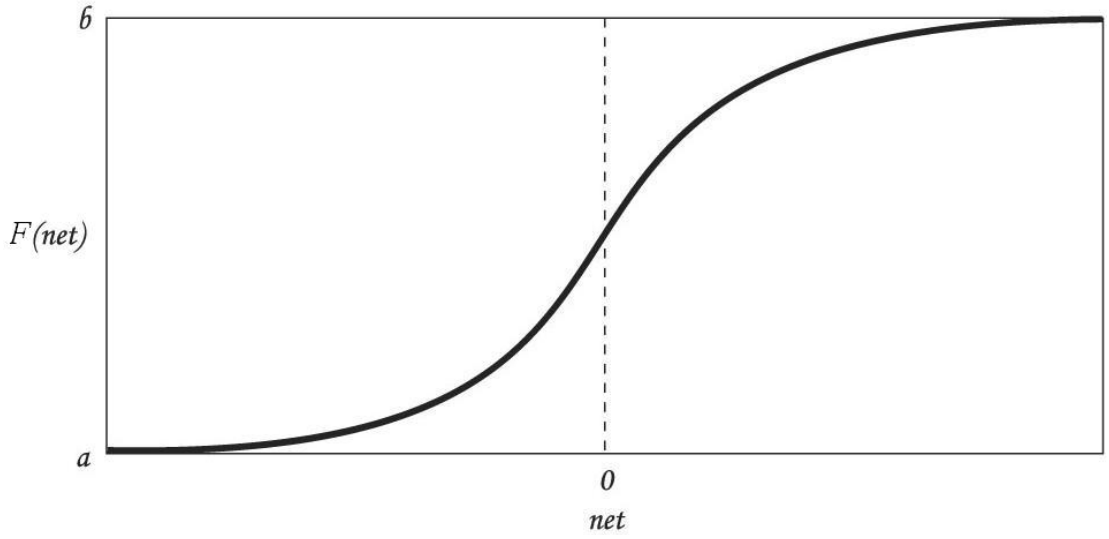

Figure 16. An Arbitrary Sigmoid Function.

III.B.4 Gaussian Functions

Bell-shaped curves such as the one illustrated in Figure 17 are known as Gaussian or radial-basis functions. Gaussian functions are also continuous, differentiable, and have asymptotes but they are not monotonic. Gaussian functions are used in radial-basis function networks. Algebraically, a Gaussian function may be described with the following expression:

$$F(net) = \frac{1}{\sqrt{2\pi}\sigma} \exp\left[-\frac{1}{2}\left(\frac{net - \mu}{\sigma} \right)^2 \right] \tag{70}$$

where μ and σ are the mean and standard deviation, respectively.

III.C Network Architecture

The power of an artificial neuron is fully realized when nodes are combined into an interactive network. The way that nodes are connected influences the performance of

an ANN, so network architecture must be considered at an early stage of the design process.

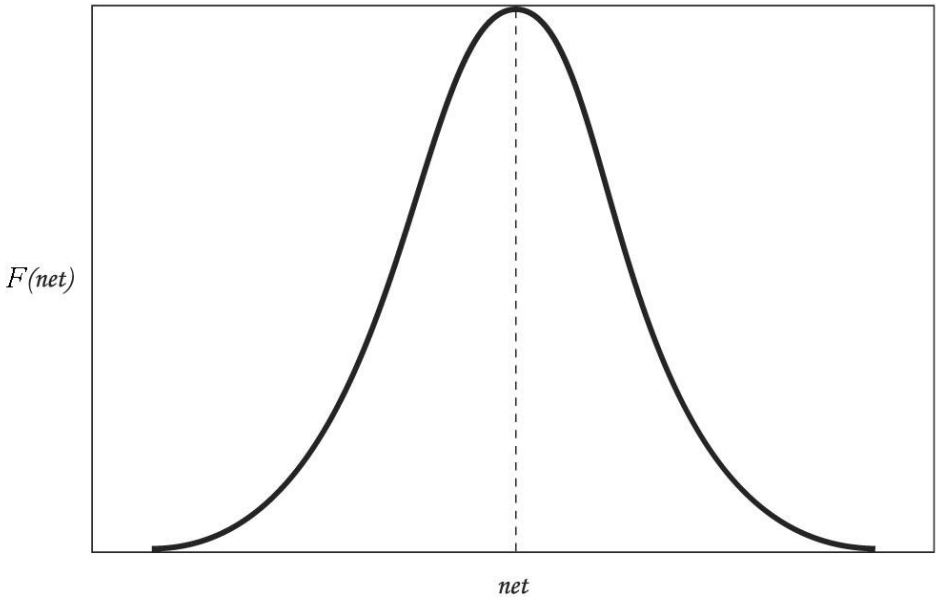

Figure 17. An Arbitrary Gaussian Function.

Biological networks in the central nervous system are complex, but a general schematic emerges from observations. The cerebral cortex, where most processing is believed to occur, is composed of five to seven layers of neurons with each layer supplying inputs into the next. However, layer boundaries are not strict. Feedback connections, connections within layers, and crossing layers are known to exist. To simulate this, each node of the general artificial network would have to communicate with itself and all of the remaining nodes. An example of such a network is shown in Figure 18, where the network has two input and two output nodes at arbitrary locations, one hidden node (a hidden node is a neither an input or an output node). Even though a

fully-connected network is most general, its use is limited due to large number of parameters. Training such a network would, therefore, be very involved.

Every other type of network can be considered a special case of the fully-connected network. Simplification is achieved by dividing the network into layers and setting some weights to zero. Many variations of such networks exist, but the simplest one presented here is the feed-forward network shown in Figure 19. Feed-forward networks are the most common among ANNs. A feed-forward network allows connections from layer *i* to layer *i + 1* only (no intra-layer connections) and can be easily described by a set of numbers that represent the number of nodes in each layer. E.g. the network in Figure 19 is a 3-2-3-2 network.

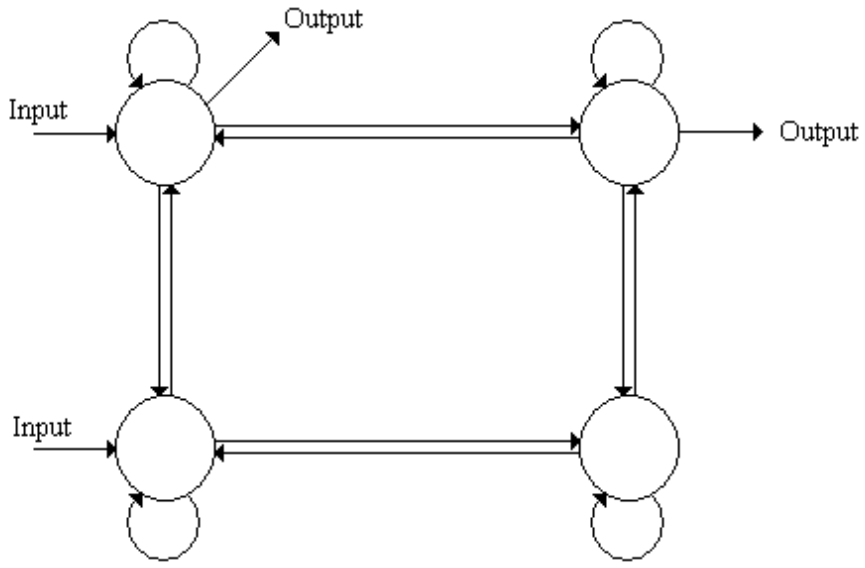

Figure 18. A Fully-connected Network.

Networks are not limited to the above-described categories. Small networks can be treated as modules, which in turn can be combined into larger systems. These systems

can be organized in different ways depending on whether modular emphasis is placed on inputs, successive refinement, etc….

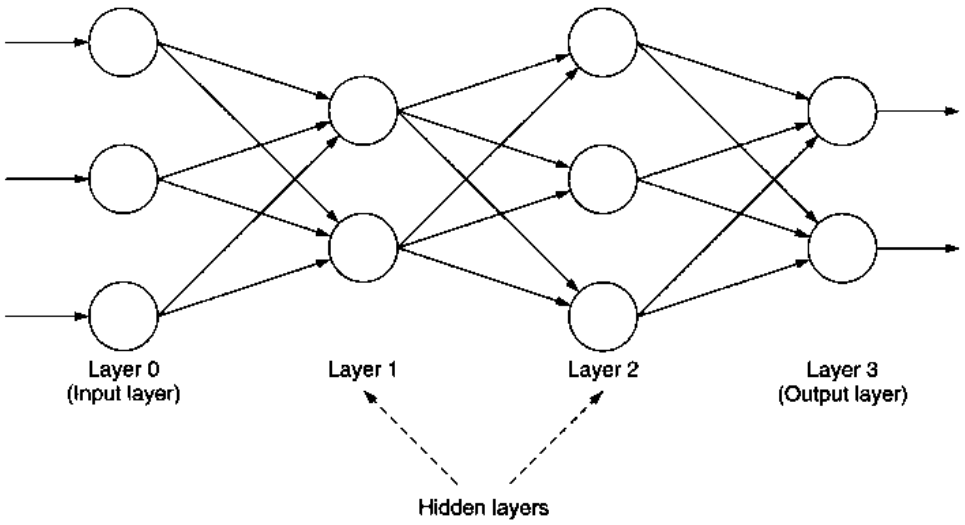

Figure 19. A Feed-forward Network [Mehrotra et al. (1996)].

III.D ANN Learning

Previous sections have shown that ANNs are made up of inputs, outputs, weights, and nodes, and have elaborated on node functions and network architectures. However, the most difficult part of obtaining an effective ANN is the selection of appropriate weights and biases. The process in which weights and biases are adjusted to achieve the best performance of an ANN is called training (or learning).

Mehrotra et al. (1996) described three types of neural learning:

1) Correlation learning. Correlation learning is based on Hebb's theory, which states that if the output from neuron A repeatedly or persistently takes place in firing neuron B, then the synaptic efficiency between

neuron A and B is increased. For ANNs, this means that the weight between node A and B is proportional to the outputs of both nodes.

2) Competitive learning. In competitive learning, different nodes compete to become "winners" for a certain type of input parameters, weights are adjusted to promote "winners" and demote "losers" for each type of input pattern. This leads to the development of networks in which each node specializes in the given type of input parameters. One can postulate that the competitive learning technique draws its principles from the fact that in biological systems, limited resources are economically distributed to the organs that are needed the most at a given instant in time.
3) Feedback-based learning. Weights in ANNs can be adapted based on a measure associated with how close the output is to the desired value. This measure is usually quantified as error, and the weights and biases are adjusted until the error is minimized. This method , and particularly the backpropagation algorithm, is very common in ANN training.

Because the backpropagation algorithm is so common, elaborating on this technique is worthwhile. The backpropagation algorithm is a supervised feedback-based learning method. The procedure consists of iteratively presenting the network with a training set of inputs and outputs, these are data from which the network can make proper pattern associations. Weights and biases are first initialized with random values, and then the training inputs are fed into the network. The output is then compared with the desired

value to determine the magnitude of the error. The error gradient[†] is computed, and the weights and biases are updated in the direction of most rapidly decreasing error. The whole process is repeated until the minimum error is found.

The exact number of data sets (points) needed to train the network is not known a priori, but there exist different heuristic approximations [Mehrotra et al. (1996)]. The more elaborate the ANN, the more data sets are needed to train the weights and biases. Simpler networks are, therefore, preferred to limit the number of required experiments. Moreover, the supervised training process can only utilize about 50-80% of the data sets available. The remaining data sets are used to test (or to validate) the performance of the ANN. Sometimes, the training process monitors the performance of both the training set and the test set and stops when the global error is smallest.

There are some indications as to which data sets should be put in the training basket and which ones kept for testing. The idea behind this decision is that when a test sample is submitted for evaluation, the ANN "interpolates" between the training points that are close to the test sample presented. Intuitively, the training batch should include the extreme available points so that the predictions are within the same range. Pacheco-Vega et al. (2001b) applied a neural network analysis to a fin-tube heat exchanger with limited experimental heat transfer data. The authors presented a cross-validation technique to identify regions where not enough training data were available to construct a reliable neural network. This technique was described as follows: "From the *M* available sets of experimental data, *(M - 1)* are used to train the ANN. After the training is finished, the data set left out is predicted and the result is compared to the experimental value. The

[†] Computation of error gradients requires that the node functions be differentiable, as stated in section III.B.

percentage error (…) is a measure of the importance of that particular set of data with respect to all the measurements." The work of Pacheco-Vega et al. (2001b) helps to determine which data points are crucial for training and where additional experimental data may be needed.

III.E ANNs in Fluid Flow and Heat Transfer Literature

Now that the principles of ANNs have been discussed, attention is shifted to the use of ANNs in heat transfer and fluid mechanics. Because ANNs have emerged relatively recently, their presence in the thermal science literature is limited. The following section describes several articles that can assist in getting started with a more thorough literature survey. By listing actual examples, this section can also help to understand how ANNs can be implemented successfully in heat transfer and fluid flow problems.

Kalogirou (1999) presented a review of various applications of ANNs in energy problems. The problems were classified into six thematic categories, and each category had subsections with specific examples as well as references. The categories described by Kalogirou (1999) were as follows:

1) Modeling various aspects of a solar steam generator.
2) HVAC systems: estimation of building heating loads, prediction of energy use in commercial buildings, optimization of energy consumption by HVAC systems, or controlling a bus air conditioning system.
3) Solar radiation.

4) Modeling and control in power generation systems: combustion modeling, control of a thermal plant, or analysis of harmonic power distortion.
5) Forecasting and prediction of power consumption and cost.
6) Refrigeration: frost prediction on evaporator coils.

Sen and Yang (2000) described the scope of ANNs and genetic algorithm[†] techniques in thermal science applications including an exhaustive bibliography. Sen and Yang (2000) presented two interesting examples that use ANNs to predict the performance of compact heat exchangers. The first heat exchanger was a single-row, fin-tube, cross-flow air-to-water type, and the second one was similar but with more tube rows. The second heat exchanger was more complex than the first one due to its geometry, the presence of air-side condensation, and fin spacing being a variable. The authors' purpose was to compare the mathematical correlations for heat transfer with an ANN approach. Both techniques were compared against experimental data. Sen and Yang (2000) proved that in both cases the ANN approach yields more accurate results (most errors within 0.7% for the first heat exchanger). The explanation is worth citing: "results suggest that the ANNs have the ability of recognizing all the consistent patterns in the training data including the relevant physics as well as random and biased measurement errors. (…) However, the ANN does not know and does not have to know what the physics is. It completely bypasses simplifying assumptions such as the use of coefficient of heat transfer. On the other hand, any unintended and biased errors in the

[†] Genetic algorithms are another type of artificial intelligence techniques. Their description here is omitted for the sake of brevity.

training data set are also picked up by the ANN. The trained ANN, therefore, is not better than the training data, but not worse either."

Another application of ANNs that Sen and Yang (2000) described is in thermal systems dynamics and control. Control of dynamic thermal systems ideally requires dynamic systems models, which relate the outputs to the inputs. Such models are usually impossible to obtain due to the complexity of practical thermal systems. This is understandable since modeling is difficult even in the static cases. Sen and Yang (2000) used ANNs to perform control experiments with the first heat exchanger. Results were again excellent showing that ANNs are able to easily overcome complexities of the problems they solve.

Ashforth-Frost et al. (1995) described a multitude of uses of ANNs in heat transfer and fluid mechanics with emphasis on visualization processing techniques such as particle image velocimetry [see also Jambunathan et al. (1996)]. The authors reported several references that used ANNs to recognize different geometric patterns in multiphase flows. In these cases, ANNs have replaced methods which had been performed manually. ANN modeling of physiological flows was also mentioned as a solution to very complex medical analyses. Furthermore, the authors mentioned inverse problems as being good candidates for ANN treatment due to their sensitivity to noise and reported several successful examples reported in the literature.

Thibault and Grandjean (1991) were one of the early authors to show the use of ANNs in heat transfer data analysis. Thibault and Grandjean (1991) solved three different heat transfer problems using three-layered, feed-forward ANNs: a thermocouple lookup table, a series of correlations between Nusselt and Rayleigh numbers for the free

convection around horizontal smooth cylinders, and the problem of natural convection along slender vertical cylinders with variable surface heat flux. The backpropagation method and the quasi-Newton methods were used in the training procedure. The quasi-Newton method showed faster and more robust convergence than the backpropagation technique and was, therefore, preferred by the authors.

Thibault and Grandjean (1991) concluded that neural networks can be used efficiently to model and correlate heat transfer data. In their opinion, the main advantage of ANNs is to remove the burden of finding appropriate model structures to fit experimental data and the disadvantage is the impossibility, simply by inspection, of determining the influence that one variable has on an output variable. ANNs, therefore, lack the transparency of most standard mathematical expressions.

ANNs were also used to correlate two-phase flow data. Kelleher et al. (2001) investigated data from a series of experiments on R-114 and R-113 pool boiling heat transfer from a vertical bank of tubes with variable amounts of oil present in the refrigerant. Their objective was to employ the neural network technique as a method of using experimental data to predict heat transfer behavior and to make the heat transfer predictions more accurate (than regular mathematical correlations), less reliant on assumptions, and easier to use.

The ANN used by Kelleher et al. (2001) had four inputs and one output. The inputs were: the temperature above saturation (superheat), the percent oil in the refrigerant, the number of active tubes, and whether the tubes were finned or staggered. The output was the heat flux. In order to graphically correlate the output for every input situation, over 60 plots would be needed. Due to this complexity, there was no attempt to

correlate the data mathematically, but rather the neural network approach was used. Kelleher et al.'s (2001) neural network had one hidden layer with log-sigmoid node functions and an output layer with linear node functions. The network was trained using the Levenberg-Marquardt [Levenberg (1944) and Marquardt (1963)] accelerated backpropagation algorithm and a set of example data. The results were very good. After training, the network was able to accurately predict the heat flux for 72 different tube correlations and varying superheat. The average percent errors were well under 10%. The advantage of the neural network technique in this situation was that complex data were correlated accurately without any assumptions that would limit the neural network's use.

Heat transfer literature is most abundant in examples of ANNs used for performance prediction and control of heat exchangers. Research around the world has been fueled by the industry's interest in being able to control heat exchangers and to provide the design engineers with simple yet effective prediction algorithms. A number of publications in this topic originated at the University of Notre Dame [Pacheco-Vega et al. (1999), (2001a), and (2001b), Diaz et al. (1996), (1999), (2001a), and (2001b), and Sen and Yang (2000)].

In order to demonstrate how ANNs can be used to analyze heat exchangers a fairly simple example by Islamoglu (2003) is described here. Islamoglu (2003) used a feed-forward backpropagation ANN to predict heat transfer rates of a wire-on-tube type heat exchanger widely used in small refrigeration systems. Nineteen experiments were conducted in three air flow modes: all cross-, wire cross-, and tube cross-flow. Islamoglu's (2003) network had twelve input nodes (describing heat exchanger geometry and fluid flow rates), one output node corresponding to the heat flux, and one hidden

layer with five nodes. The data were successfully correlated with a mean relative error of 4% (7.94% maximum relative error). Islamoglu's (2003) example shows how powerful ANNs are in correlating data governed by complex physics.

ANNs have also been used to characterize various flows inside tubes and channels, a topic of particular interest in this dissertation. Ghajar et al. (2004) used ANNs to significantly improve heat transfer correlations in the transition region for a circular tube with three different inlet configurations. The network Ghajar et al. (2004) used had five input nodes, one hidden layer with eleven nodes, and one output node. A separate training process was used for each tube inlet configuration. Islamoglu and Kurt (2004) trained an ANN to predict heat transfer from a channel with triangular corrugations. The input parameters were: corrugation pitch, corrugation angle, the *Re* number, and the hydraulic diameter. The output was the *Nu* number. The network had a 4-5-1 feed-forward architecture and correlated *Nu* numbers with an average relative error <4%. Scalabrin and Piazza (2003) applied neural networks to analyze heat transfer from tubes with supercritical carbon dioxide. This problem was particularly challenging due to thermophysical properties having very strong gradients in the near-critical zone. Scalabrin and Piazza (2003) demonstrated the importance of selecting the proper input variables (i.e., those that account for the property gradients in the radial direction of flow) to obtain a universal ANN. In their particular case, failure to identify the correct input variables resulted in an ANN that was only able to "memorize" the training data set but was not general enough to correlate data from other sources.

Chen et al. (2001) is the only source known to the author that dealt with spirally corrugated tubes in terms of ANNs. However, the focus was only on the shape of the

corrugation and not the helix angle. Chen et al. (2001) tested tubes with four starts, a similar pitch (~9mm), diameter (~18.9mm), ridge height (~2.2mm), and helix angle (~61°) but different corrugation shapes. The shape of the corrugation was quantified in terms of angles α' and α'' as shown on Figure 20. The authors devised a radial-basis function ANN that correlated the angles of the triangular groove, α' and α'', with the inside heat transfer coefficient. Next, they used the ANN to determine the optimal corrugation shape. The highest value for the heat transfer coefficient occurred at $\alpha'' \approx 90°$ and $\alpha' \approx 62°$. This result was outside of the range of tested tubes.

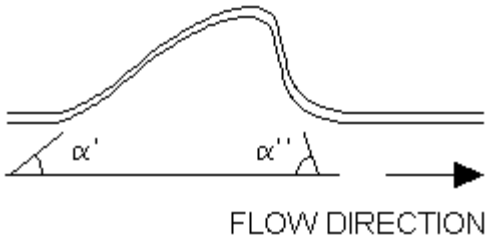

Figure 20. Corrugation Angles Investigated by Chen et al. (2001).

Albeit small, the number of publications described here indicates that ANNs can be used for a wide range of heat transfer and fluid problems. The literature review also shows that ANNs have not been applied to correlate heat transfer and friction with all of the necessary geometric parameters of a helically-finned tube. Such attempt is made in the following chapters of this dissertation.

CHAPTER IV

EXPERIMENTAL PROGRAM

Previous chapters introduced the concepts and historical background of heat transfer and friction in helically-finned tubes, as well as principles of artificial neural networks. Attention was focused on the lack of complete understanding of flow behavior in helically-finned tubes and the consequent need for empirical data.

An experimental program devised to measure turbulent pressure drop and heat transfer in helically-finned tubes was conducted at Mississippi State University. The experimental results were needed to train various artificial neural networks and to develop algebraic correlations for prediction purposes.

IV.A Tube Geometries Tested

Eight enhanced tubes and one plain tube were tested. The tubes were manufactured by Wieland-Werke AG of Ulm (Germany) for condenser applications. The geometric parameters of each tube are delineated in Table 1. The external geometry and the length were the same for each tube. The length was 10 ft; however, for installation purposes, only 9 ft of length were "finned" on both the outside and the inside of the tube. The tube material was copper-nickel. The internal fins were 0.48-mm thick at the base and 0.2-mm thick at the tip. Thus, the included angle β was 41°.

Tubes 5, 6, and 7 were matched to test the effect of the fin height. Tubes 2 and 3, and 4, 6, and 8 were used to analyze the influence of the helix angle. Finally, tubes 3 and 8 and 1, 2, and 4 were tested to investigate the effect of the number of starts.

Table 1. Tube Geometries.

Tube #	External Structure			Copper Wall	Internal Structure			
	Outside Diameter	Fin pitch	Fin Height	Thickness	Fin Height	Number of Starts	Helix Angle	Internal Diameter
	(mm)	(fins/inch)	(mm)	(mm)	(mm)	-	(°)	(mm)
1	18.82	40	0.945	0.645	0.38	10	25	15.64
2	18.82	40	0.925	0.68	0.375	30	25	15.61
3	18.86	40	0.94	0.68	0.38	30	48	15.62
4	18.79	40	0.925	0.685	0.38	45	25	15.57
5	18.82	40	0.90	0.71	0.31	45	35	15.6
6	18.79	40	0.93	0.68	0.38	45	35	15.57
7	18.82	40	0.935	0.68	0.51	45	35	15.59
8	18.77	40	0.925	0.67	0.38	45	48	15.58
9	18.85	40	0.93	0.67	0	-	-	15.65

IV.B Experimental Apparatus

A schematic of the experimental apparatus is shown in Figure 21. The helically-finned test tube was the inside of a double-pipe counterflow heat exchanger. Heat was transferred from the hot water flowing inside the test tube to the cold water flowing in the annulus. The cold water was provided by the city at approximately 20°C. The hot water loop consisted of a large water tank with a 15-kW variable-output heater, a 1-hp pump, the test tube, and a set of ball valves used to adjust the velocity of the water in the test tube. The cold water side consisted of a 9-ft long, 1¼-in I.D. annulus and a set of ball valves used to adjust the cold water flow rate. The water tank and all the piping were insulated.

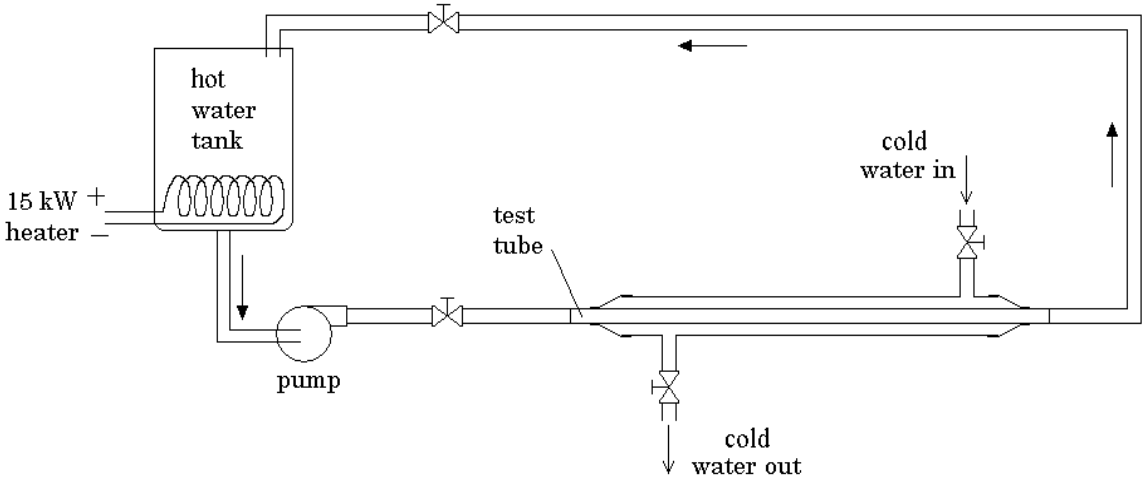

Figure 21. Experimental Apparatus Schematic.

Figure 22 shows a detailed schematic of the test section. Two pressure taps were attached to the test tube. The pressure taps were connected to a Sensotec model TJE differential pressure transducer with a 0.1% accuracy. The temperatures were measured with 3-in-long type-T thermocouples mounted inside tees. The hot water line thermocouples were installed inside 1¼-in I.D. expansions in order to promote mixing of the water coming out of the test tube (and, thus, to measure the "mixing-cup" temperature). The test tube velocity was obtained by measuring the hot water line flow rate with an Omega FP-5300 flow meter accurate to 0.2 ft/s. The chilled water flow rate was measured with a Hersey 1006 flow meter accurate to 1%.

Every transducer, after being carefully calibrated, was connected to an SCXI data acquisition system from National Instruments. The data acquisition system was composed of an SCXI-1102C module with an SCXI-1303 terminal block that measured temperatures and an SCXI-1100 module with an SCXI-1303 terminal block that measured flow rates and pressure drop. Both modules were installed in an SCXI-1000

chassis connected to a desktop computer via a PCI-MIO-16XE-50 data acquisition card. The hardware was controlled through a program written in LabVIEW 6.1. Figure 23 reproduces the front panel of the LabVIEW program written for this study.

IV.C Data Reduction

The Fanning friction factor was calculated according to the following data reduction equation:

$$f = \frac{\Delta P \cdot D}{2 \cdot L \cdot \rho \cdot V^2} \tag{71}$$

where L is the distance between pressure taps, ΔP is the pressure drop between pressure taps, D is the nominal inside diameter, ρ is the density at the mean bulk temperature, and V is the average velocity based on the nominal diameter.

The inside heat transfer coefficient required a more complex approach because information about heat transfer in the annulus had to be obtained first. The heat transfer in the double-pipe, counterflow heat exchanger is governed by the total thermal resistance equation:

$$\frac{1}{U_o A_o} = \frac{1}{U_i A_i} = \frac{1}{UA} = \frac{1}{h_i A_i} + \frac{\ln(D_o/D_i)}{2\pi k_{wall} L} + \frac{1}{h_o A_o} \tag{72}$$

where the areas are based on the nominal outside or inside tube diameters. Solving for the inside heat transfer coefficient yields the data reduction equation for the heat transfer coefficient measurement:

$$h_i = \frac{1}{\left(\frac{1}{U_o} - \frac{1}{h_o} - \frac{D_o \ln(D_o/D_i)}{2k_{wall}}\right)\frac{A_i}{A_o}} \tag{73}$$

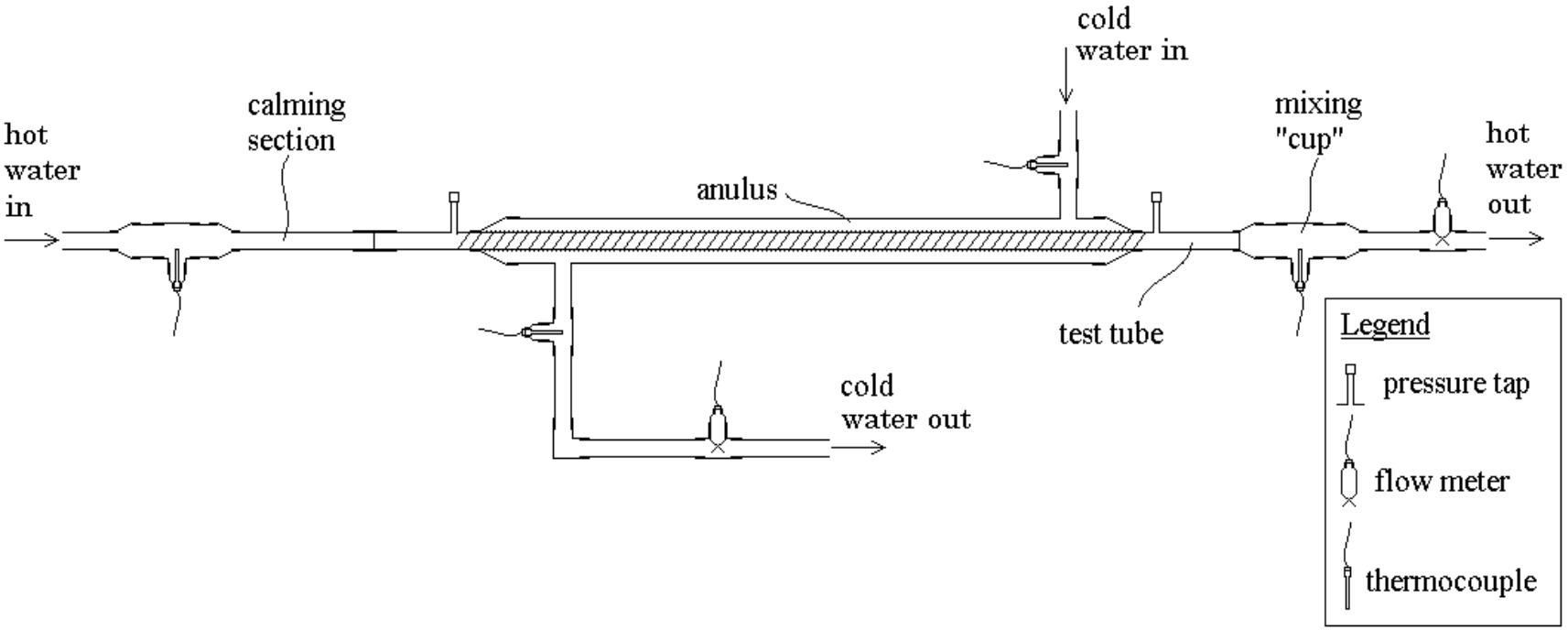

Figure 22. Detailed Test Section Schematic.

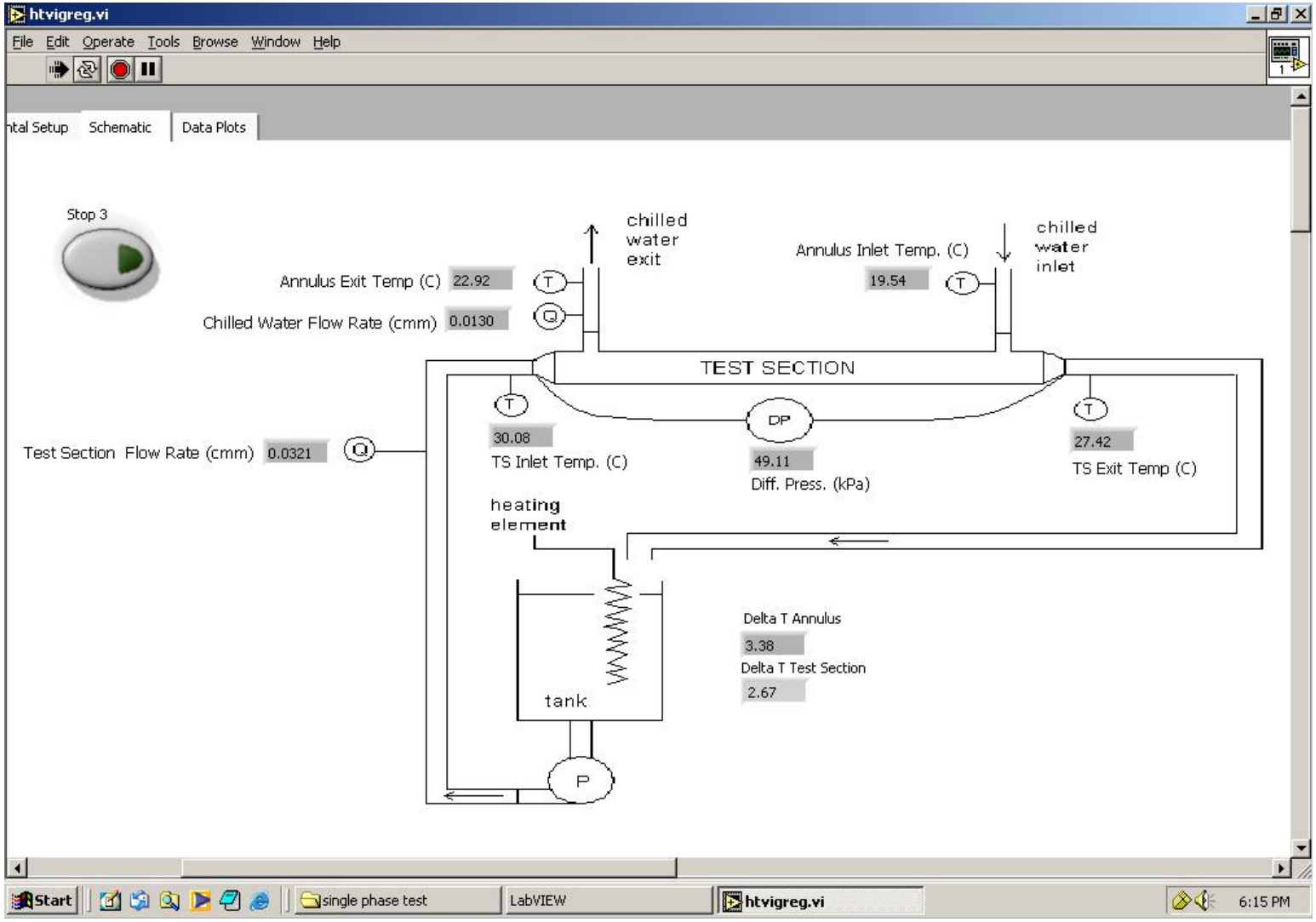

Figure 23. LabVIEW Program Front Panel.

In order to find h_i, U_o and h_o had to be known. U_o was calculated using an energy balance and the logarithmic mean temperature difference method. The mean heat transfer rate was used to find the overall heat transfer coefficient U_o:

$$\dot{Q}_o = \dot{m}_o c_{p_o} (T_{o,out} - T_{o,in}) \tag{74}$$

$$\dot{Q}_i = \dot{m}_i c_{p_i} (T_{i,in} - T_{i,out}) \tag{75}$$

$$\dot{Q}_{mean} = \frac{\dot{Q}_{in} + \dot{Q}_{out}}{2} \tag{76}$$

From the definition of the overall heat transfer coefficient:

$$U_o = \frac{\dot{Q}_{mean}}{A_o LMTD} \tag{77}$$

where *LMTD* is the logarithmic mean temperature difference.

The outside heat transfer coefficient, h_o, was obtained by means of the Wilson plot technique described in detail by Briggs and Young (1968). Basically, the heat transfer coefficient of the annulus is assumed to be represented by an equation of the following form (that is the same form as the Dittus-Boelter equation):

$$\frac{h_o D_{h,o}}{k_o} = C \,\mathrm{Re}_o^{\,n}\, \mathrm{Pr}_o^{\,0.4} \tag{78}$$

where $D_{h,o}$ is the annulus hydraulic diameter, C and n are arbitrary constants, and the properties are evaluated at the mean bulk temperature. The 0.4 exponential coefficient was chosen because the water in the annulus was being heated. Based on the above analysis, equation (72) can be represented in the following fashion:

$$\frac{1}{UA} = C_1 \,\mathrm{Re}_o^{\,-n} + C_2 \tag{79}$$

where $C_1 = \left(\frac{k_o}{D_{h,o}} C A_o \, \mathrm{Pr}_o^{\,0.4} \right)^{-1}$ and $C_2 = \frac{\ln(D_o/D_i)}{2\pi k_{wall} L} + \frac{1}{h_i A_i}$. Constants C_1 and n were found graphically, as described in section IV.E. With C and n known, h_o was determined from equation (78) and h_i from equation (73).

IV.D Uncertainty Analysis

An uncertainty analysis was performed according to the guidelines outlined in Coleman and Steele (1999). The uncertainties of the calculated variables were found with the propagation technique, which quantifies how the uncertainties in the measured variables propagate through the data reduction equation. In general, the uncertainties of the measured variables arise from the use of calibration data fits and finite accuracy of standards and equipment used during the calibration process. Table 2 lists the uncertainties of the measured variables and calculated variables.

Table 2. Uncertainties in Experimental Data.

Measured Variables		Calculated Variables	
Variable	Uncertainty	Variable	Uncertainty
T	0.23 K	f	15%
$\dot{m}_i$	7%	$\dot{Q}$	8%
$\dot{m}_o$	3%	h_o	10%
ΔP	150 Pa	h_i	10%
L	1/16 in	Nu_i	10%
D	0.01 mm		
properties	negligible		

The propagation of uncertainties associated with water and copper properties was neglected. The hot water flow meter was the largest contributor of uncertainty in the calculated variables. Therefore, the 15% uncertainty in the Fanning friction factor was

largely due to the 7% uncertainty in the test water mass flow rate. The Nu_i had an uncertainty of only 10% because the heat flux used to compute h_i was an average of $\dot{Q}_i$ and $\dot{Q}_o$, reducing the overall error. A physical manifestation of uncertainty in the measured variables was the discrepancy between $\dot{Q}_i$ and $\dot{Q}_o$ at steady-state conditions. These two values were measured within 10% of each other.

IV.E Experimental Procedure and Results

The objective of the first stage of the experiment was to obtain a correlation for the outside heat transfer coefficient, h_o. To achieve this objective, the Wilson plot technique was utilized. The plain tube was inserted into the apparatus, and the hot water line valves were opened to full speed ($Re_i \approx 56\,000$) and held constant. The heater setting remained at approximately 7 kW throughout the entire experiment. The cold water line (annulus) flow rate was varied and the overall heat transfer coefficient was recorded for each flow rate after steady-state conditions were reached. The data points acquired during this process were used to generate a plot of *1/UA* values versus Re_o^{-n}. The value of *n* was varied until the data points fell on a straight line. Once the correct *n* value was found, C_1 was the slope of this straight line and *C* was obtained via $C_1 = \left(\frac{k_o}{D_{h,o}} C A_o \, \mathrm{Pr}_o^{\,0.4} \right)^{-1}$. The plot generated by the Wilson Plot procedure is shown in Figure 24. The values of *C* and *n* were found to be 1.302×10^{-3} and 1.234, respectively.

The second stage consisted of validating the experimental apparatus. Isothermal friction factors and heat transfer coefficients were measured for the plain tube at Re_i ranging from 12 000 to 50 000. During the heat transfer test, the water heater was set at 7

kW, and the annulus flow rate was maintained constant at Re_o = 15 000. For consistency, these settings were used for all of the nine tubes tested. The plain tube results were compared with the Blasius and the Dittus-Boelter equations readily available in the heat transfer literature. The maximum percent difference between the measured and the theoretical values were 11% for the friction factor and 8% for the heat transfer coefficient. Once the experimental apparatus was validated, the helically-finned tubes were tested. The experimental results were cast in terms of the Fanning friction factor, f, and the Nusselt number, Nu_i (plotted, respectively, in Figure 25 and Figure 26). Heat transfer results were also cast in terms of the Colburn j-factor, for which the assumed dependence between Nu_i and Pr_i is

$$j = St_i \cdot \mathrm{Pr}_i^{2/3} = \frac{Nu_i}{\mathrm{Re}_i \cdot \mathrm{Pr}_i} \mathrm{Pr}_i^{2/3} = \frac{Nu_i}{\mathrm{Re}_i \cdot \mathrm{Pr}_i^{1/3}} \tag{80}$$

The Colburn j-factor results are plotted in Figure 27.

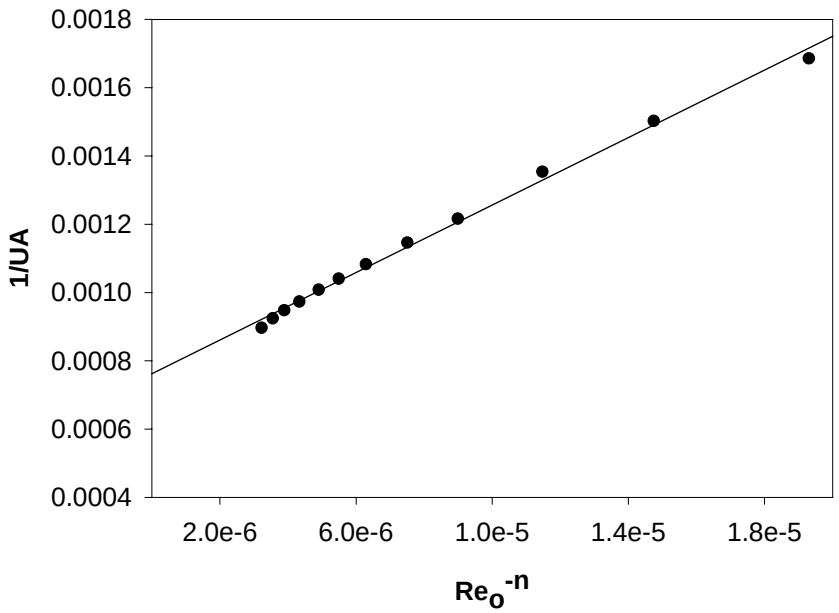

Figure 24. Wilson Plot.

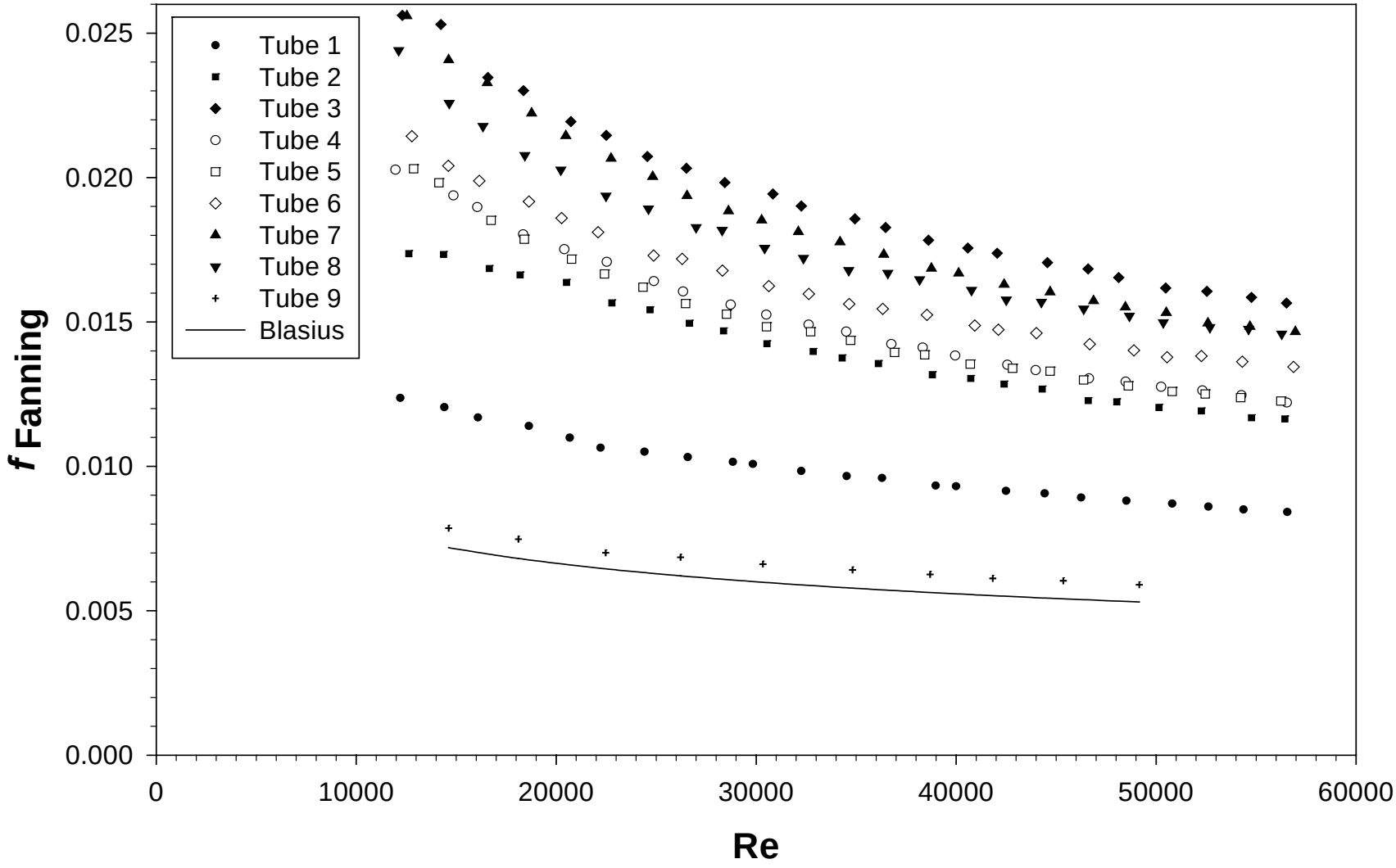

Figure 25. Current Study Fanning Friction Factor Comparison.

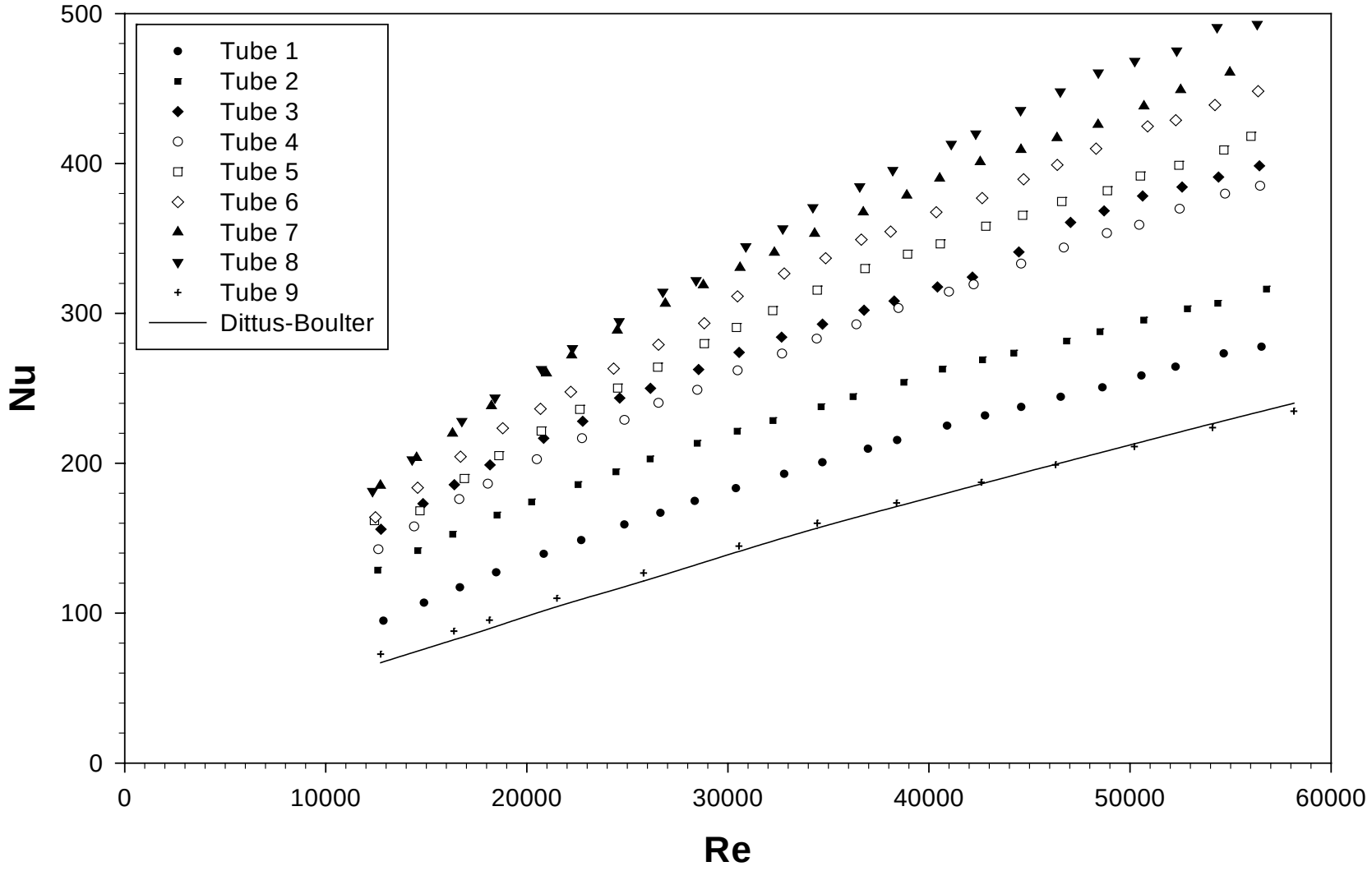

Figure 26. Current Study Nusselt Number Comparison.

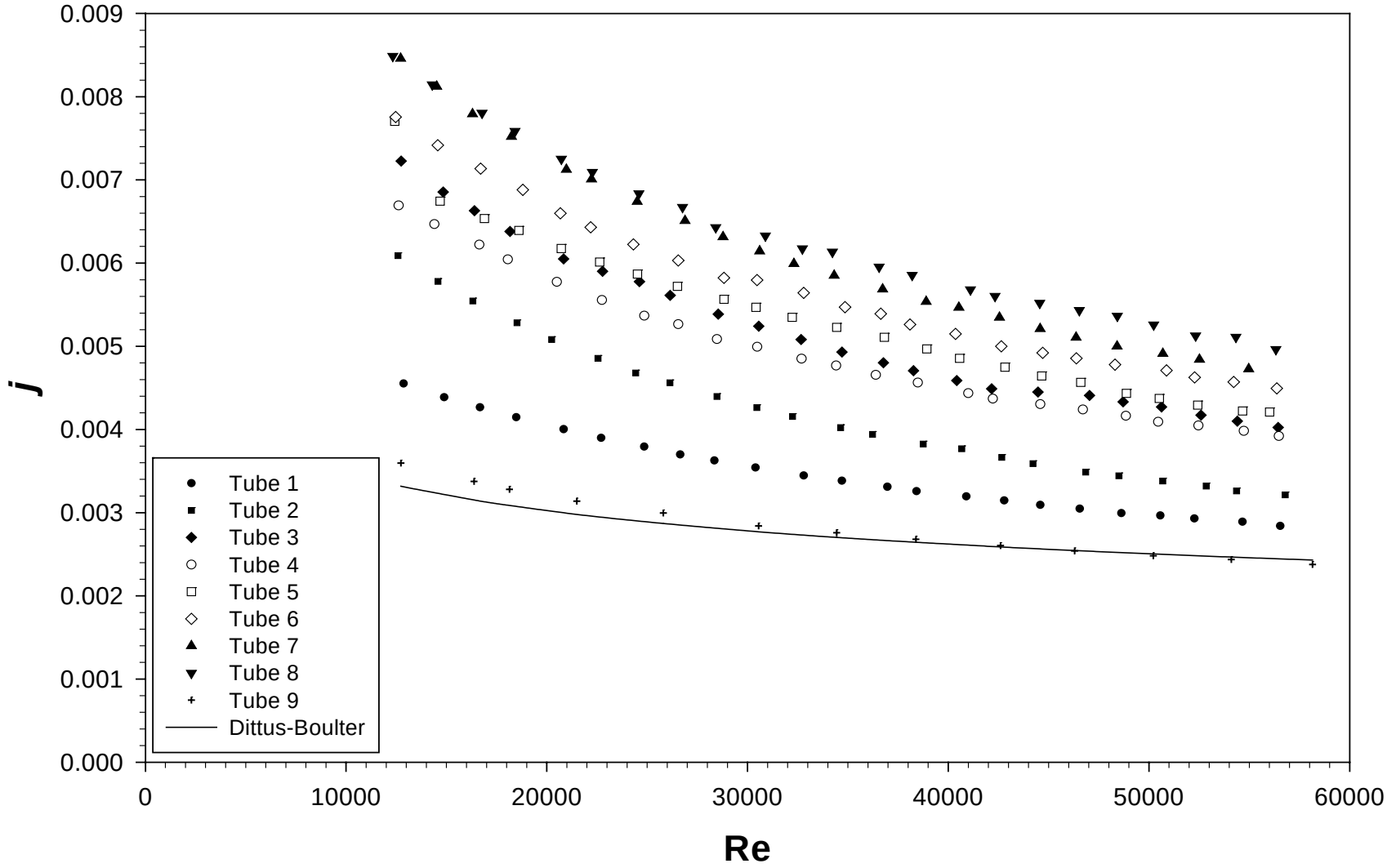

Figure 27. Current Study Colburn *j*- Factor Comparison.

IV.F Discussion of Results

The first topic of concern is the comparison of the plain tube performance with commonly available prediction equations. As stated in section IV.E, the plain tube measured friction factor was at most 11% higher than the Blasius solution, and the Nusselt number was at most 8% off from the Dittus-Boelter equation. The magnitudes of these errors are within the range obtained from the uncertainty analysis. Therefore, the plain tube results were considered acceptable, thus validating the experimental apparatus.

Before discussing the enhanced-tube results presented in Figure 25 and Figure 26, it is practical to convert the internal geometry of the tubes in Table 1 into dimensionless parameters. Table 3 was obtained by introducing the axial fin pitch, $p = \pi D/(N_s \tan \alpha)$ and calculating the dimensionless factors e/D, p/e, and p/D. These dimensionless parameters allow a more direct comparison between the tubes and provide more physical insight into the results (e.g., for a transverse fin reattachment occurs at $6 < p/e < 8$). Table 3 does not explicitly indicate that the helix angle and the number of starts are dimensionless parameters. However, since these parameters are unitless, they can be treated as such. Therefore, α and N_s can be used as direct parameters in any correlation.

The friction results shown in Figure 25 follow a rather predictable trend. The same can be said about the Nu_i results from Figure 26. The friction factor decreases and the Nusselt number increases with increasing Reynolds number. In order to study the influence of geometric parameters, tubes that vary in only one of the independent variables must identified and compared. This task is achieved qualitatively in Table 4, where each geometric parameter is listed and its influence on f and Nu_i is identified. For the most part, the results are consistent with rational expectations; that is, both f and Nu_i

increase with increasing *e/D*, N_s, and α. The only exception occurs in the comparison of the friction factor in tubes 3 and 8. This exception could be caused by the high helix angle (48°) and the consequent development of skimming flow (tubes 8 and 3 have a *p/e* ratio of 2.577 and 3.876, respectively) with a lower friction factor for tube 8 than for tube 3.

Table 3. Test Tube Dimensionless Parameters.

Tube #	Internal Structure					Dimensionless Factors		
	D **[mm]**	***e*** **[mm]**	***p*** **[mm]**	N_s	α [°]	***e/D***	***p/e***	***p/D***
1	15.64	0.38	10.54	10	25	0.0243	27.729	0.674
2	15.61	0.375	3.51	30	25	0.0240	9.348	0.225
3	15.62	0.38	1.47	30	48	0.0243	3.876	0.0941
4	15.57	0.38	2.33	45	25	0.0244	6.134	0.150
5	15.6	0.31	1.56	45	35	0.0199	5.017	0.100
6	15.57	0.38	1.55	45	35	0.0244	4.085	0.100
7	15.59	0.51	1.55	45	35	0.0327	3.048	0.100
8	15.58	0.38	0.98	45	48	0.0244	2.577	0.0629
9	15.65	plain						

Table 4. Qualitative Analysis of the Influence of Geometric Parameters on Friction and Heat Transfer Results.

Parameter under study	Tubes used for parameter study (in order of increasing parameter)	Tube numbers in order of increasing experimental *f*	Tube numbers in order of increasing experimental Nu_i
N_s or *p/e*	$1 \rightarrow 2 \rightarrow 4$	$1 \rightarrow 2 \rightarrow 4$	$1 \rightarrow 2 \rightarrow 4$
N_s or *p/e*	$3 \rightarrow 8$	$8 \rightarrow 3$	$3 \rightarrow 8$
e/D	$5 \rightarrow 6 \rightarrow 7$	$5 \rightarrow 6 \rightarrow 7$	$5 \rightarrow 6 \rightarrow 7$
α	$4 \rightarrow 6 \rightarrow 8$	$4 \rightarrow 6 \rightarrow 8$	$4 \rightarrow 6 \rightarrow 8$

Among the helically-finned tubes, the highest friction factor was displayed by tube 3 and the lowest by tube 1. In terms of the Nusselt number, the best performance was achieved by tube 8 and the worst by tube 1. Tube 1 has the smallest helix angle and

the smallest number of starts (N_s = 10; p/e = 27.729). Tubes 3 and 8 have the highest helix angle (α = 48°). Tube 7 is also worthy of note because of its highest e/D ratio (0.0327) with α = 35°. Except at Re_i = 12 000, tube 7 displayed the second highest friction factor and Nusselt number. At a Reynolds number of 12 000, tube 7 had the highest Nu_i and a friction factor nearly equal to that of tube 3.

The information presented so far would seem to confirm the theory that the helix angle is one of the most important parameters in determining the characteristics of flow in helically-finned tubes. Basically, the results obtained in this study do not contradict any of the assertions presented in CHAPTER II.

IV.G Empirical Correlation Development

The purpose of the current section is to obtain least-squares empirical correlations for prediction of *f*- and *j*-factors in helically-ribbed tubes. The reason for producing algebraic least-squares correlations is to have an ANN assessment criterion (or a benchmark). The ANN performance must be better than a least-squares correlation or the extra effort of developing the ANN is of no value.

A common and reasonable approach in correlating several variables is to use a power-law approach. Such an approach was utilized by Webb et al. (2000), as presented in CHAPTER II equations (15) and (16):

$$f = 0.108\,\mathrm{Re}^{-0.283}\,N_s^{0.221}(e/D)^{0.785}\alpha^{0.78} \tag{15}$$

$$j = \mathrm{St}\,\mathrm{Pr}^{2/3} = 0.00933\,\mathrm{Re}^{-0.181}\,N_s^{0.285}(e/D)^{0.323}\alpha^{0.505} \tag{16}$$

The process of least-squares regression consists of finding the power coefficients that make the prediction error minimal. Some preliminary algebraic manipulation can make

this task a linear algebra problem. Equations (15) and (16) can be represented by the following general form:

$$f = \chi_1 \,\mathrm{Re}^{\chi_2}\, N_s^{\chi_3} (e/D)^{\chi_4} \alpha^{\chi_5} \tag{81}$$

where χ_1 through χ_5 are constants to be determined, and the left-hand side could very well be replaced by j. Taking the natural logarithm of both sides yields:

$$\ln f = \ln \chi_1 + \ln \mathrm{Re}^{\chi_2} + \ln N_s^{\chi_3} + \ln(e/D)^{\chi_4} + \ln \alpha^{\chi_5} \tag{82}$$

or

$$\ln f = \ln \chi_1 + \chi_2 \ln \mathrm{Re} + \chi_3 \ln N_s + \chi_4 \ln(e/D) + \chi_2 \ln \alpha \tag{83}$$

The above equation can be formulated for each data point collected. When dealing with multiple equations, a matrix notation is preferred:

$$\begin{bmatrix} \ln f \\ \vdots \end{bmatrix} = \begin{bmatrix} 1 & \ln \mathrm{Re} & \ln N_s & \ln(e/D) & \ln \alpha \\ \vdots & \vdots & \vdots & \vdots & \vdots \end{bmatrix} \begin{bmatrix} \ln \chi_1 \\ \chi_2 \\ \chi_3 \\ \chi_4 \\ \chi_5 \end{bmatrix} \tag{84}$$

where the dots represent the repeating equations. There are as many equations as there are data points, so the linear algebra problem has the form:

$$\Psi = \Theta X \tag{85}$$

where X is the vector of unknown constants to be determined, Θ is the equation matrix, and Ψ is the vector of natural logarithms of experimentally determined friction factors or j factors.

The key point of the correlation development is to minimize the prediction error. The easiest error to monitor is the sum of the squared errors; hence, the name least-

squares regression. Using matrix algebra formulation, the sum of the squared errors associated with any given vector X is

$$\sum error_{\Psi}{}^{2} = (\Psi - \Theta \mathrm{X})^{T} (\Psi - \Theta \mathrm{X}) \tag{86}$$

In the current study, Mathcad software was used to minimize the error function introduced in the equation above. Mathcad analysis yielded the following equations:

$$f = 0.128\,\mathrm{Re}^{-0.305}\, N_s^{0.235} (e/D)^{0.319} \alpha^{0.397} \tag{87}$$

$$j = 0.029\,\mathrm{Re}^{-0.347}\, N_s^{0.253} (e/D)^{0.0877} \alpha^{0.362} \tag{88}$$

The best way to verify the performance of equations (87) and (88) is to plot the percent error between the predicted and experimental values. The error for the friction factor is plotted in Figure 28 (mean squared error: $MSE = 1.070\text{x}10^{-6}$) and the one for the j factor is depicted in Figure 29 ($MSE = 6.945\text{x}10^{-8}$). Both figures include the vast majority of the predicted data within 10% of the experimental results. Tube 3 shows the highest under-prediction for the friction factor case and the highest over-prediction of the j factor. Tube 8 has the highest over-prediction of the friction factor, and tube 7 exhibits the highest under-prediction of the j factor. Moreover, Figure 29 demonstrates wave-shaped variations of the error with respect to the Reynolds number. The mathematical form of the j factor correlation [equation (81)] proposed a priori is unable to represent such variation; a limitation that an artificial neural network does not possess.

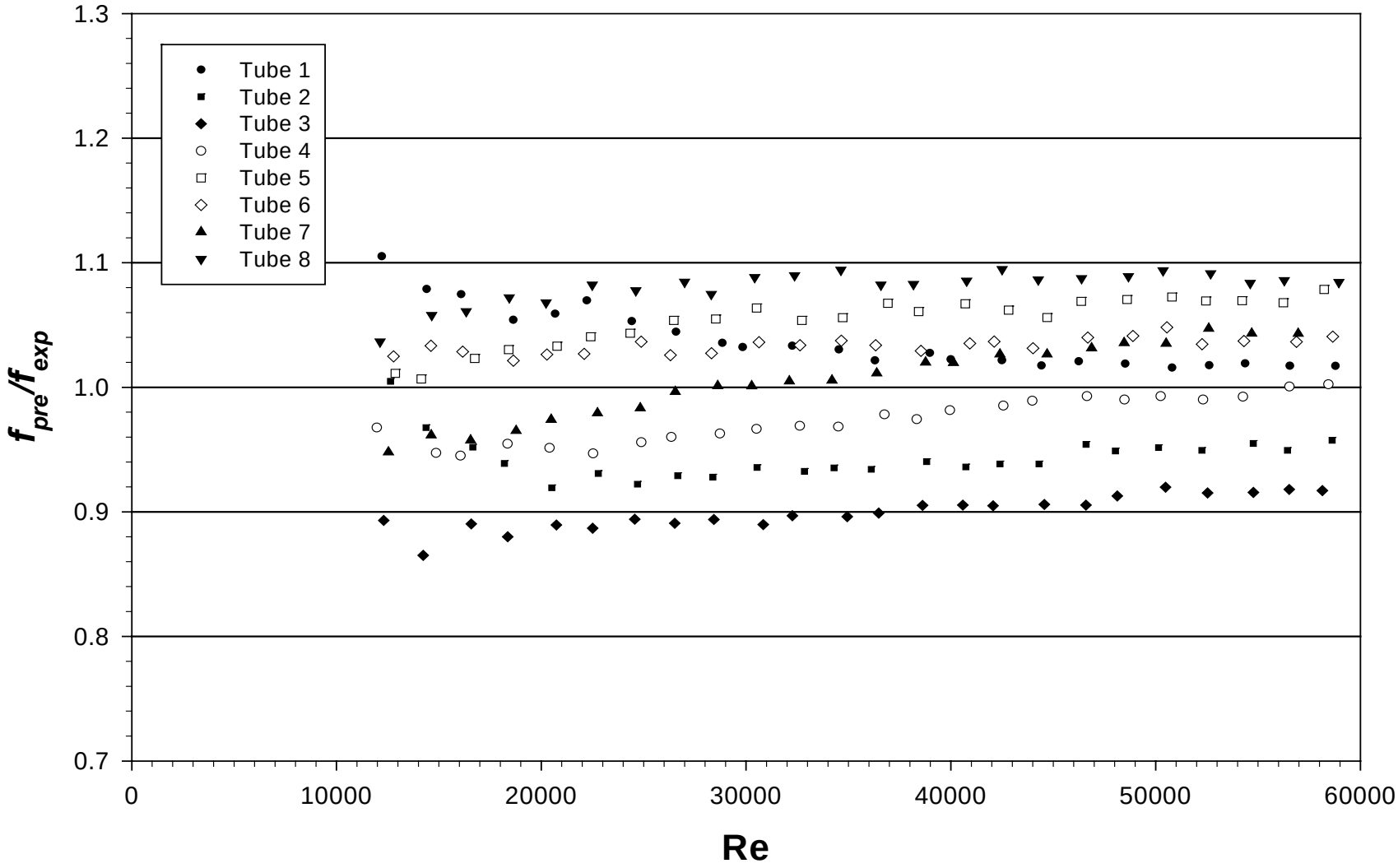

Figure 28. Evaluation of Friction Results with Equation (87).

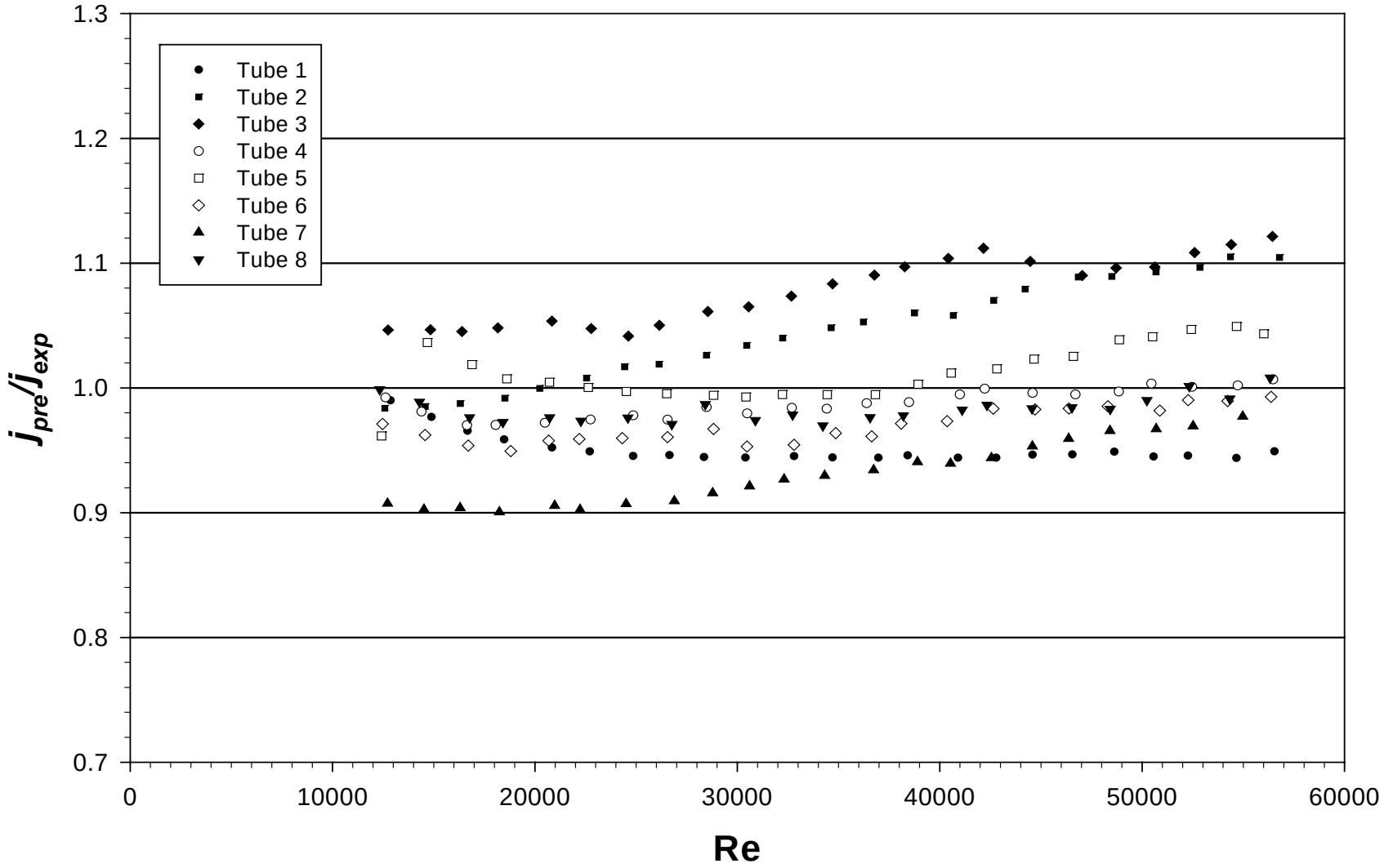

Figure 29. Evaluation of Heat Transfer Results with Equation (88).

IV.H Evaluation of Equations (87) and (88) with Experimental Data of Webb et al. (2000)

The purpose of the next two sections is to evaluate the correlations developed in equation (87) and (88) with independent experimental data. Table 5 presents the similarities and differences between the current study and that of Webb et al. (2000). Table 6 provides more detail about the internal geometries of the tubes tested by Webb et al. (2000). Table 6 tubes are numbered W1 through W8 in order to distinguish them from the tubes used in the current study. From the information provided in both tables, one can see that, on one hand, the experimental set-ups have enough similarities to suggest that comparison of results is possible and, on the other hand, there are some differences that could make the two data sets complimentary.

Table 5. Differences/Similarities Between Current Study and Webb et al. (2000).

	Current study	**Webb et al. (2000)**
Test fluid	Water	Water
Inside diameter	15.57 mm to 15.64 mm	15.54 mm
Heat transfer rate	±7 kW (cooling)	10.55 kW (cooling)
Helix angle	25° to 48°	25° to 45°
Number of starts	10 to 45	10 to 45
Fin thickness at base	0.48 mm	0.29 mm to 0.41 mm
Fin thickness at tip	0.2 mm	0.24 mm
Included angle	41°	41°
p/e	2.577 to 27.729	2.81 to 9.88
e/D	0.0199 to 0.0327	0.0210 to 0.0356
Re_i	12 000 to 56 000	20 000 to 80 000
Pr_i	4.25 to 5.47	5.08 to 6.29
Outside Conditions	Water at $T = \pm 20°C$ and $Re_o = 15\,000$ (counter-flow)	R-12 boiling at $P_{sat} = 517$ kPa ($T_{sat} = 16.8°C$)

The friction factor and *j*-factor data of Webb et al. (2000) have been digitized with DigXY software. The digitizing procedure consists of scanning the plotted results

into digital format and placing the mouse cursor on each data point to obtain numerical values for the X-Y pair under study. The friction factor and *j*-factor results obtained in the manner described above are plotted in Figure 30 and Figure 31, respectively.

Table 6. Tubes Tested by Webb et al. (2000).

Tube	**Manufac-**	**I.D.**	***E***	***p***	***t***	N_s	***α***	***e/D***	***p/e***	***p/D***
#	**Turer**	(mm)	(mm)	(mm)	(mm)	-				
W1	Wolverine	15.54	plain							
W2	Wolverine	15.54	0.327	1.08	0.265	45	45°	0.0210	2.81	0.0591
W3	Wolverine	15.54	0.398	1.63	0.28	30	45°	0.0256	3.50	0.0896
W4	Wolverine	15.54	0.43	4.88	0.325	10	45°	0.0277	9.88	0.273
W5	Wolverine	15.54	0.466	1.74	0.275	40	35°	0.0300	3.31	0.0993
W6	Wolverine	15.54	0.493	2.79	0.28	25	35°	0.0317	5.02	0.159
W7	Wolverine	15.54	0.532	4.19	0.28	25	25°	0.0342	7.05	0.241
W8	Wolverine	15.54	0.554	5.82	0.28	18	25°	0.0356	9.77	0.348

The next step was to evaluate both sets of data with equations (87) and (88). The prediction error for the friction factor with respect to equation (87) is shown in Figure 32 ($MSE = 1.345 \times 10^{-5}$) and the prediction error for the *j*-factor with respect to equation (88) is depicted in Figure 33 ($MSE = 3.886 \times 10^{-6}$). The plots demonstrate that equation (87) over-predicts Webb et al.'s (2000) friction data by an average 30% (see Figure 32) and equation (88) under-predicts Webb et al.'s *j*-factor data by an average 30%, with a visible error increase with increasing Reynolds number (see Figure 33).

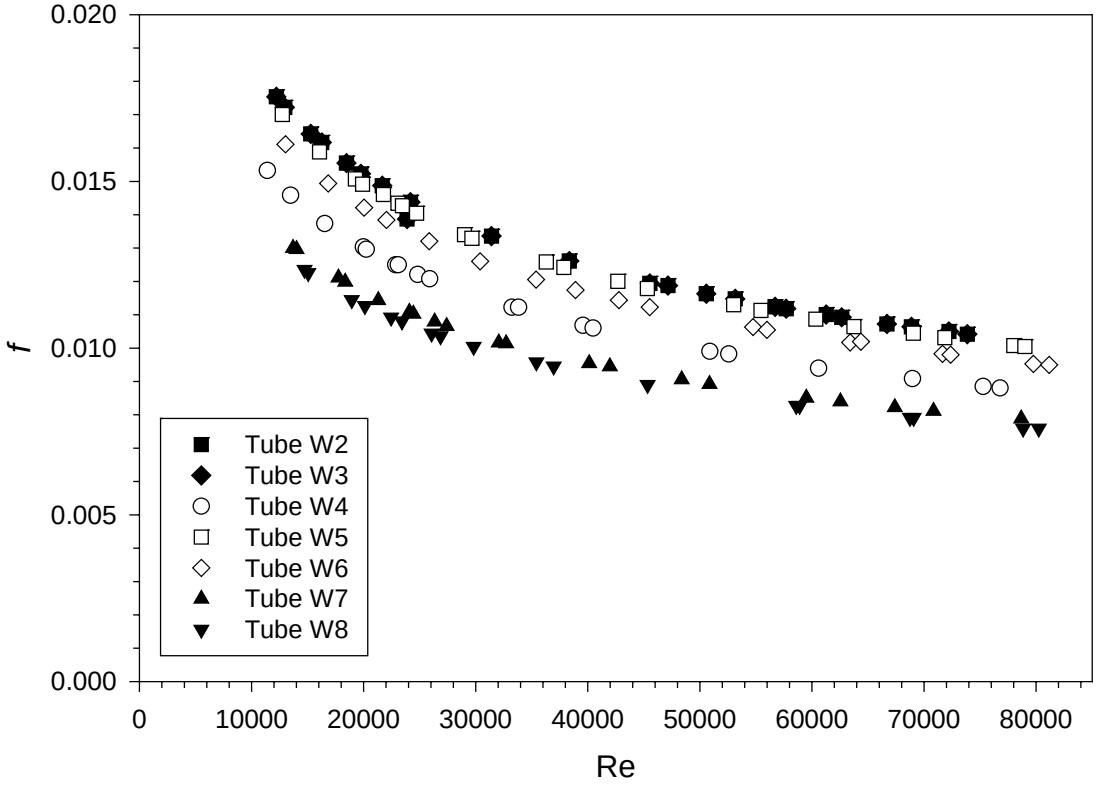

Figure 30. Friction Data of Webb et al. (2000).

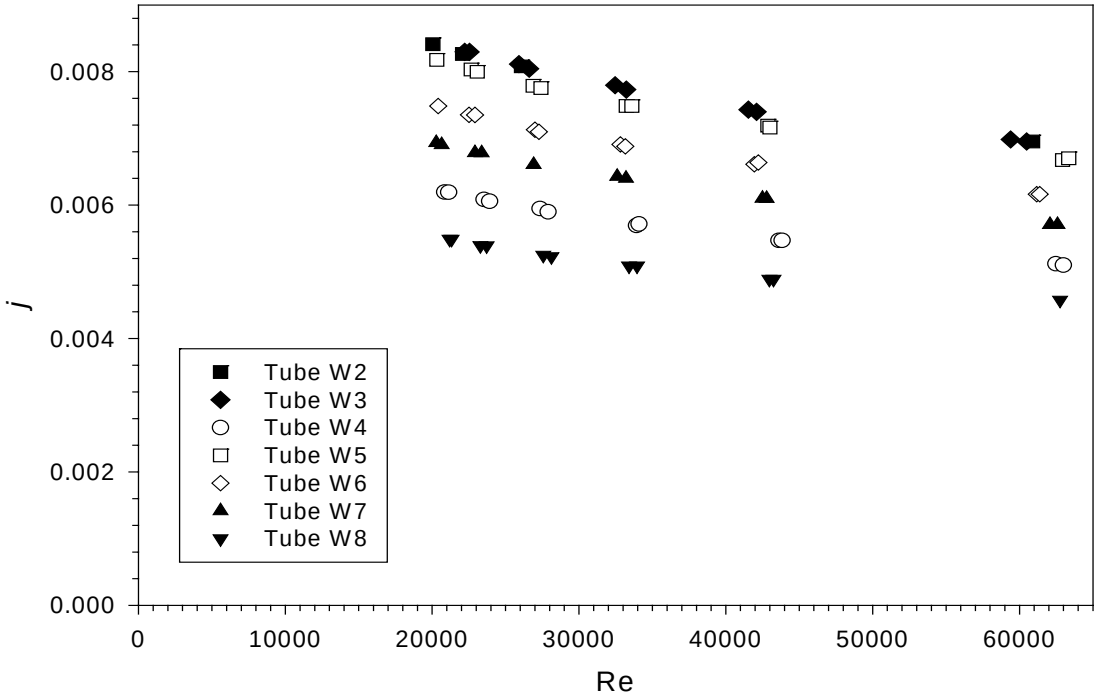

Figure 31. *j*- Factor Data of Webb et al. (2000).

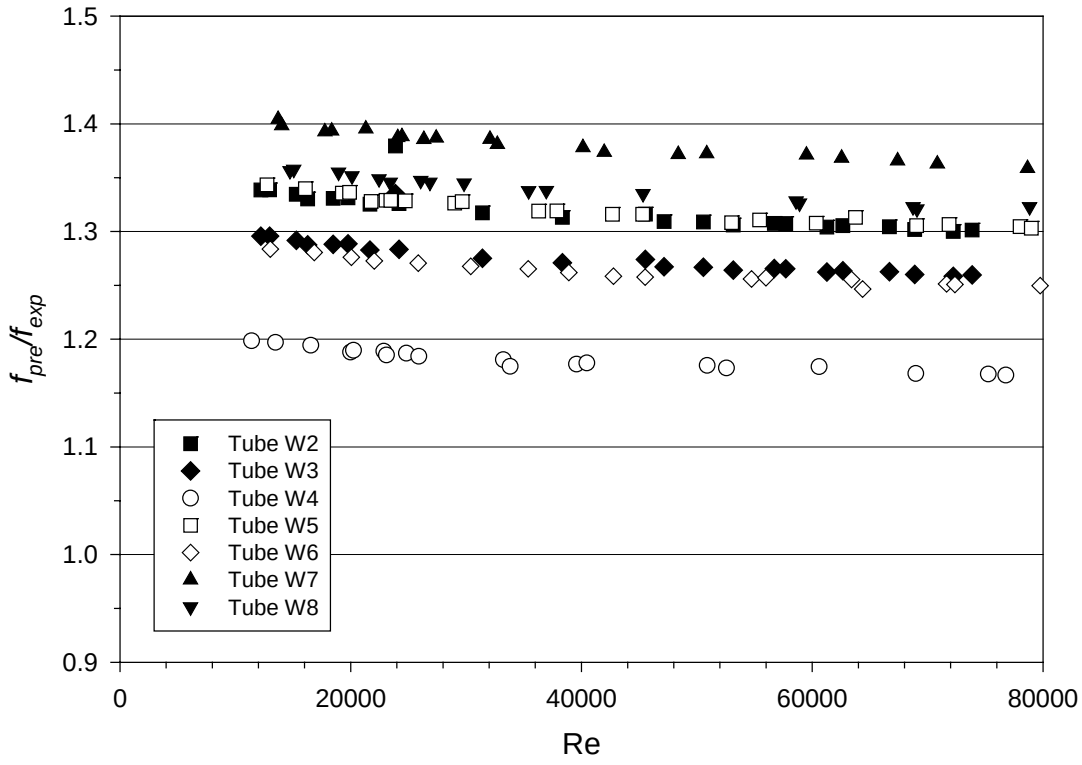

Figure 32. Evaluation of Equation (87) with Webb et al. (2000) *f* Data.

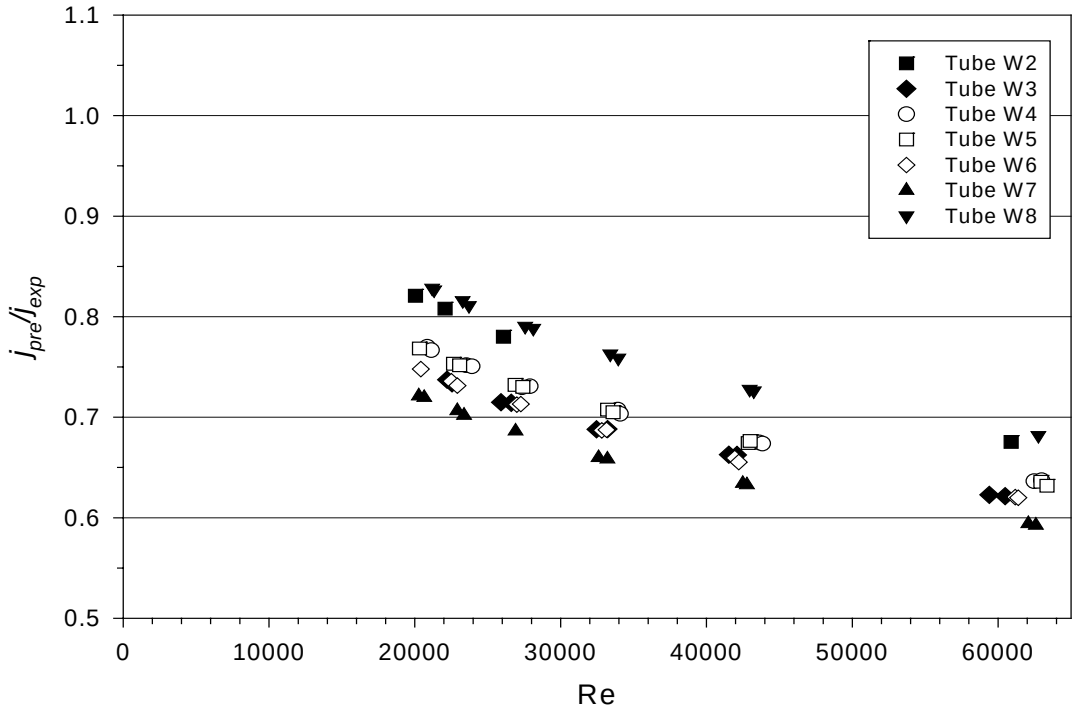

Figure 33. Evaluation of Equation (88) with Webb et al. (2000) *j* Data.

IV.I Evaluation of Equations (87) and (88) with Experimental Data of Jensen and Vlakancic (1999)

Jensen and Vlakancic (1999) reported experimental data of six helically-ribbed tubes outlined in Table 7. The tubes have been numbered JV1 through JV6 in order to distinguish them from the tubes tested in the current study. The tubes reported by Jensen and Vlakancic (1999) are different from the ones employed in this study. Firstly, their fin thickness is relatively large, and, secondly, there is always at least one geometric parameter outside of the range of the current study tubes.

Table 7. Tubes Reported by Jensen and Vlakancic (1999).

Tube #	**Manufacturer**	**I.D.** [mm]	***e*** [mm]	***p*** [mm]	***t*** [mm]	N_s -	α [°]	***e/D*** -	***p/e*** -	***p/D*** -
JV1	Wolverine	23.64	1.16	16.079	1.00	8	30	0.0491	13.861	0.680
JV2	Wolverine	23.78	1.20	9.243	1.02	14	30	0.0505	7.702	0.389
JV3	Wolverine	23.70	1.30	4.299	0.82	30	30	0.0549	3.307	0.181
JV4	Wieland	22.10	0.22	1.286	0.58	54	45	0.00996	5.844	0.0582
JV5	Wolverine	24.13	0.33	1.404	0.90	54	45	0.0137	4.254	0.0582
JV6	Wieland	22.08	0.44	1.285	0.54	54	45	0.0199	2.920	0.0582

Jensen and Vlakancic (1999) used two experimental test sections, one to obtain cooling results and one for heating results; however, only cooling results are considered here. Each test section was a double-pipe counterflow water-to-water heat exchanger 4.72-m long, which included a 1.52-m calming length.

Digitized friction and *j*-factor data of Jensen and Vlakancic (1999) are shown in Figure 34 and Figure 35, respectively. Experimental *Nu* numbers were converted into *j*-factor format (assuming a mean fluid and wall temperatures of 35°C and 20°C, respectively) to allow for evaluation of equations (87) and (88). The prediction errors associated with equations (87) and (88) are plotted in Figure 36 and Figure 37,

respectively. The mean squared errors associated with the prediction of *f* and *j*-factors were 2.666×10^{-5} and 5.355×10^{-6}, respectively.

Figure 36 demonstrates that equation (87) over-predicts Jensen and Vlakancic (1999) friction factors by roughly 30% except at low Reynolds numbers where tubes JV4, JV5, and JV6 show a high prediction error. Figure 37 illustrates that equation (88) under-predicts Jensen and Vlakancic (1999) *j*-factor data by roughly 30% except for tubes JV4 and JV5, which show a high over-prediction error at low Reynolds number and a small error at high Reynolds numbers. In general, the *f* and *j* prediction errors seem to be consistent with the ones depicted in Figure 32 and Figure 33, respectively. Other than experimental uncertainty, the sources of discrepancy between the data of the three studies are hard to identify, which only shows how little is known about heat transfer and fluid flow in helically-finned tubes.

The next chapter will use the Mississippi State University data set and also data of other researchers to develop ANNs for the prediction of friction factors and *j*-factors. As stated earlier, the purpose of CHAPTER IV correlations is to use them as benchmarks for the evaluation of ANNs performance.

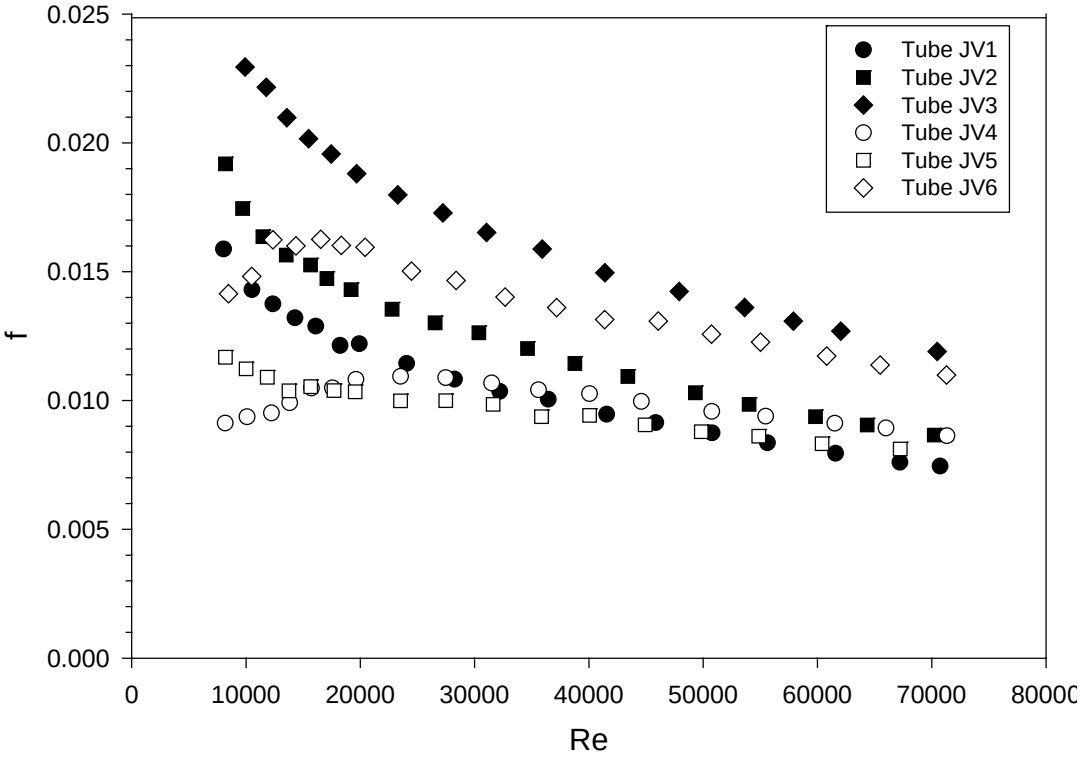

Figure 34. Friction Data of Jensen and Vlakancic (1999).

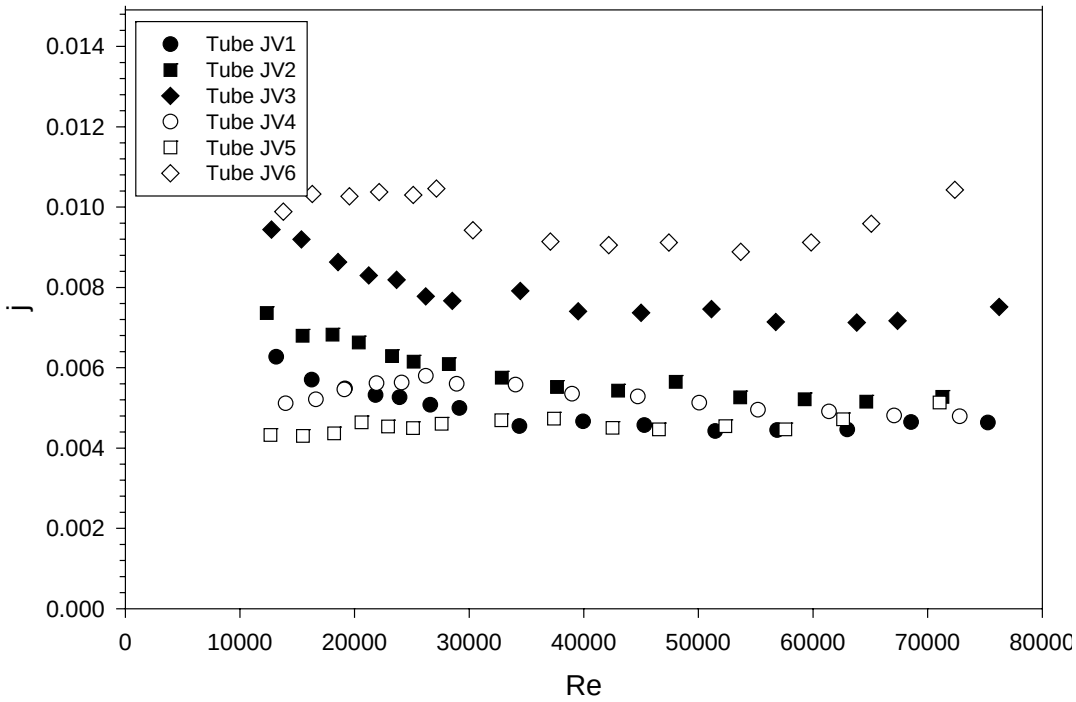

Figure 35. *j*- Factor Data of Jensen and Vlakancic (1999).

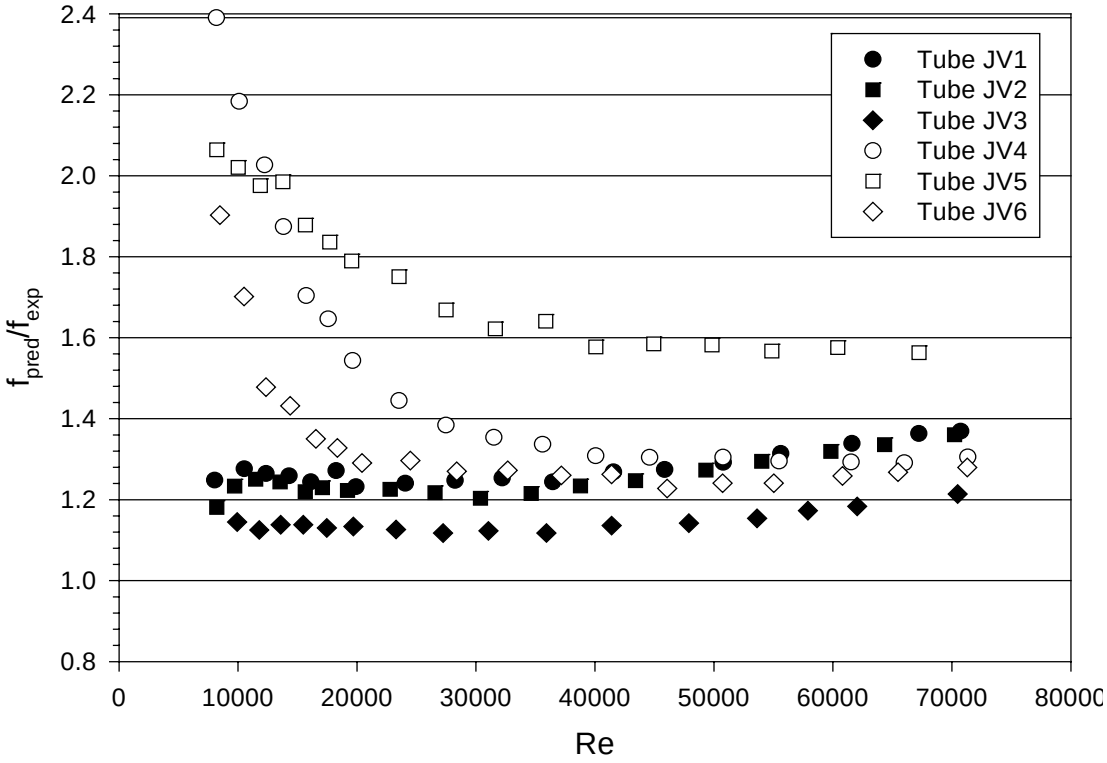

Figure 36. Evaluation of Equation (87) with Jensen and Vlakancic (1999) *f* Data.

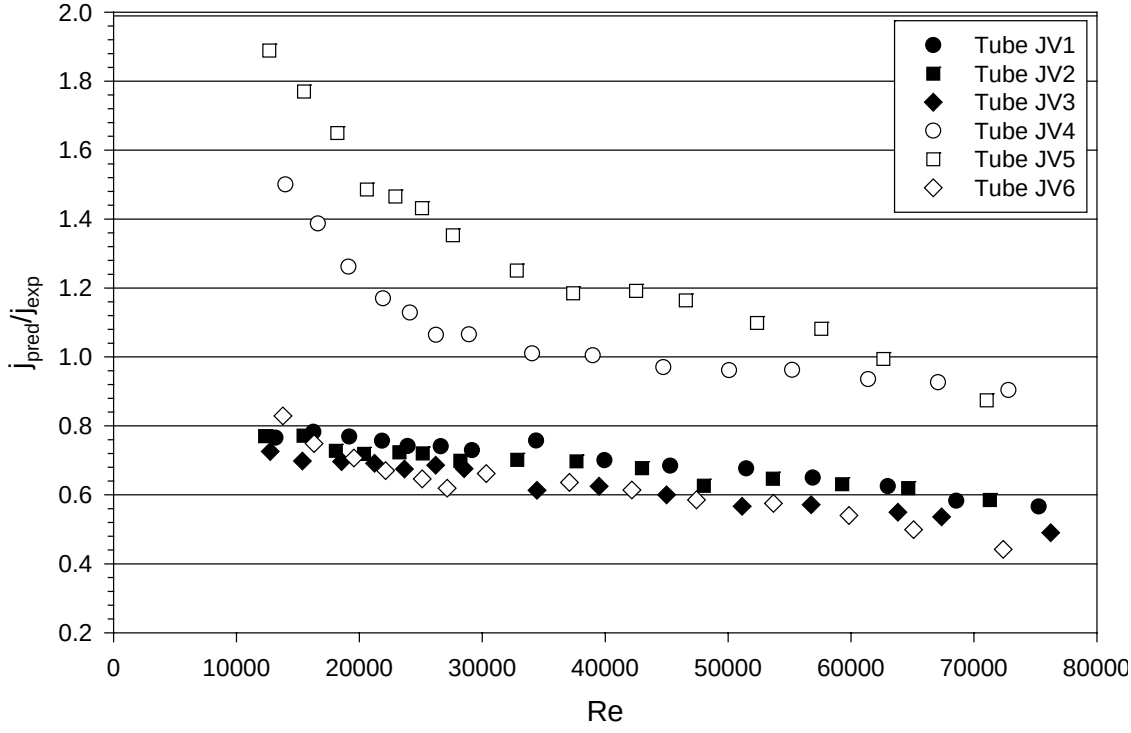

Figure 37. Evaluation of Equation (88) with Jensen and Vlakancic (1999) *j* Data.

CHAPTER V

ARTIFICIAL NEURAL NETWORK DEVELOPMENT

V.A Notation

Figure 38 shows a general three-layer ANN and the notation employed. Due to the large number of parameters involved, developing an unambiguous way of presenting the constants and functions that describe a neural network is important. In this study, the software employed for ANN development is MATLAB, so the notation presented here is almost identical to that used by MATLAB. The only difference is that MATLAB indexing must start at 1 and not 0; so in MATLAB, all the 0-indexed variables are essentially replaced by a different variable. The consistency of the notation presented herein allows MATLAB to execute computations at each layer rapidly because of its matrix algebra capability [Hagan et al. (1996)].

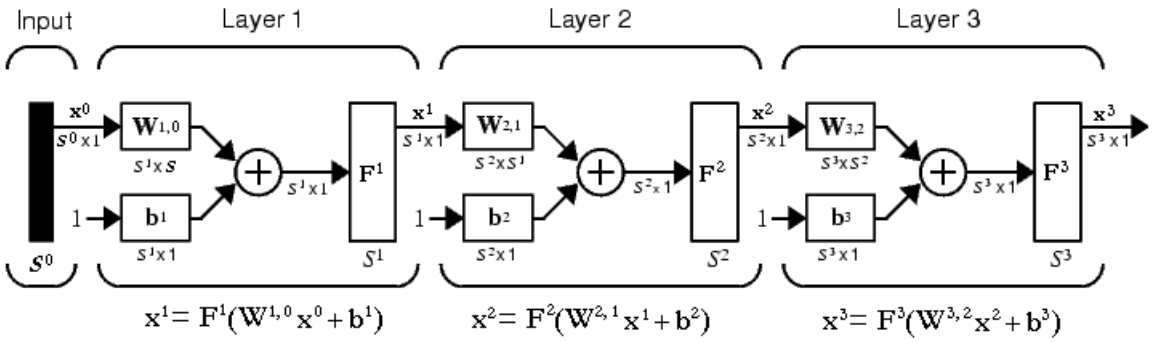

Figure 38. Neural Network Notation.

The index-0 layer represents inputs (see Figure 38). $\boldsymbol{x}^0$ is a column vector of inputs of size S^0; whereas, S^1, S^2, and S^3 are the number of nodes in layer 1, 2, and 3, respectively. $\boldsymbol{W}^{1,0}$ is a weight matrix feeding the inputs to layer 1. The weight matrix is constructed such that entry $\boldsymbol{W}^{1,0}{}_{j,k}$ multiplies input k and feeds it into node j in layer 1. In general, $\boldsymbol{W}^{l,m}{}_{j,k}$ multiplies output k from layer m and feeds it into node j in layer l. $\boldsymbol{b}$ is the bias column vector. Its size corresponds to the number of nodes in a given layer. $\boldsymbol{F}$ is a vector of node functions (MATLAB feed-forward backpropagation networks utilize either linear, log-sigmoid, or tan-sigmoid functions) and generally, the same function is used for the entire layer.

APPENDIX A presents the different ANNs that were trained in this study. Weights and biases are reported as matrices and vectors, respectively, in the notation presented above. Furthermore, the name of the ANN also contains the description of the network's architecture. For example, "f_ANN_4LS_3LS_1LIN" stands for a friction factor network with 4 nodes in layer 1 using log-sigmoid functions [in MATLAB: $logsig(x) = 1 / (1 + exp(-x))$], 3 nodes in layer 2 using log-sigmoid functions, and 1 node in layer 3 using a linear function [in MATLAB: $purelin(x) = x$].

V.B Normalization of Experimental Data

When training ANNs, normalizing the inputs and targets to ensure that all the weights are within the same order of magnitude is advantageous. The normalized data will be denoted with the symbol "*." The data from the current study have been normalized in the following fashion:

$$\mathrm{Re}^* = \left(\frac{\mathrm{Re} - 1800}{\mathrm{Re} + 1800} \right)^2 \tag{89}$$

$$N_s^* = \frac{N_s}{100} \tag{90}$$

$$e/D^* = 10 \cdot e/D \tag{91}$$

$$\alpha^* = \sin(\alpha) \tag{92}$$

$$f^* = 10 \cdot f \tag{93}$$

$$j^* = 100 \cdot j \tag{94}$$

The significance of equation (89) is that it forces *Re** to go to zero if *Re* = 1 800 (critical Reynolds number for transition) and to one if *Re* is large. The other normalizing equations have been chosen for their simplicity. Moreover, the inputs to every neural network in this study have been organized in the following manner:

$$x^0 = \begin{Bmatrix} N_s^* \\ \alpha^* \\ e/D^* \\ \mathrm{Re}^* \end{Bmatrix} \tag{95}$$

V.C Determination of Optimal Network Architecture

The performance of an ANN depends on its architecture. Large networks can learn complex functions, but require more effort to train and to report. Hence, the network selection process is a compromise between a small network size and a minimal prediction error. The architecture of the optimal network to be used for prediction of friction and *j*-factors in helically-ribbed tubes was determined for this study by training different networks and evaluating their performance with the mean squared error (*MSE*)

criterion. Half of the experimental data (every other Reynolds number) from each tube was put into a training basket, while the entire data set was used for validation. The Levenberg-Marquardt algorithm [Levenberg (1944) and Marquardt (1963)] was used for the training process. Training was stopped when the *MSE* of the entire data set reached a minimum. The training results were compiled in Table 8, which lists the *MSE*s of all networks trained with 50% of experimental data. Additional information about each network (i.e., weights, biases, training curves, and performance plots) is included in APPENDIX A. The idea behind the selection of the various networks in Table 8 was to start out with an arbitrary 4-3-1 network and to remove nodes and layers to see what happens to the network's performance. Initially, one node was removed from each of the first two layers to yield a 3-2-1 network. Next, the second layer was removed to yield a 4-1 network. Then, a 2-1 network was constructed. For the 2-1 case, a log-sigmoid output node function was also tested, but showed no improvement in performance.

Table 8. Mean Squared Errors of ANNs Trained With 50% of Data.

f		***j***	
Network	***MSE***	**Network**	***MSE***
f_4LS_3LS_1LIN	7.7760×10^{-9}	j_4LS_3LS_1LIN	1.0062×10^{-9}
f_3LS_2LS_1LIN	1.6848×10^{-8}	j_3LS_2LS_1LIN	2.2488×10^{-9}
f_4LS_1LIN	8.3616×10^{-9}	j_4LS_1LIN	1.9653×10^{-9}
f_2LS_1LIN	1.0061×10^{-7}	j_2LS_1LIN	6.3833×10^{-9}
f_2LS_1LS	1.1755×10^{-7}	j_2LS_1LS	6.5631×10^{-9}

Table 8 reveals that even the worst performing networks, f_2LS_1LS and j_2LS_1LS, have a smaller mean squared error than the power-law regression presented in the previous chapter [equations (87) and (88) showed, respectively, a *MSE* of 1.070×10^{-6} for *f* and a *MSE* of 6.945×10^{-8} for *j*). The 4-3-1 architecture exhibited the

smallest *MSE*. Removing one node from the first two layers deteriorated the networks' performance more than removing the second layer. For this reason, the 4-1 network appears to be more suitable for prediction of *f* and *j* in helically-ribbed tubes.

The use of the *MSE* is an excellent numerical criterion for evaluating the performance of a prediction tool. Nevertheless, a visual inspection of the error behavior is also very important. Figure 28 and Figure 29 in CHAPTER IV visualized the performance of the power-law regressions developed in the previous chapter. For comparison purposes, these visualizations are redrawn in Figure 39 and Figure 40 in a slightly different manner, which will be employed throughout the rest of the chapter.

Now, consider the performance of the f_4LS_1LIN network depicted in Figure 41 and the j_4LS_1LIN network in Figure 42. Both networks were trained with 50% of experimental data as described earlier. Both figures clearly show that the 4-1 network geometry works very well, and, more importantly, that the neural network performance is superior to the power-law regression performance. Based on this visual inspection and the *MSE* values of Table 8, the prediction (or "regression") error associated with the 4-1 ANNs trained with 50% of data can be taken as negligible. Thus, the only error associated with the use of these networks is the experimental uncertainty.

The information presented so far reinforces the statement that the ANN does not know and does not have to know what the physics of the problem are. The ANN completely bypasses simplifying assumptions such as the use of a power-law equation. On the other hand, any unintended and biased errors in the training data set are also picked up by the ANN. The trained ANN, therefore, is not better than the training data, but not worse either.

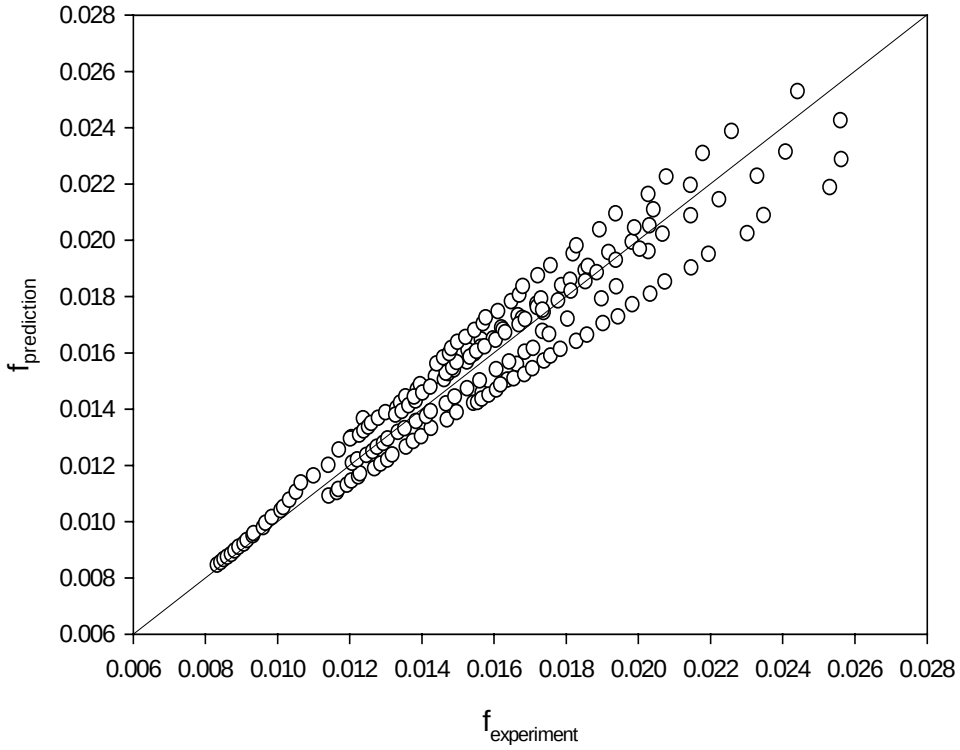

Figure 39. Performance of Equation (87).

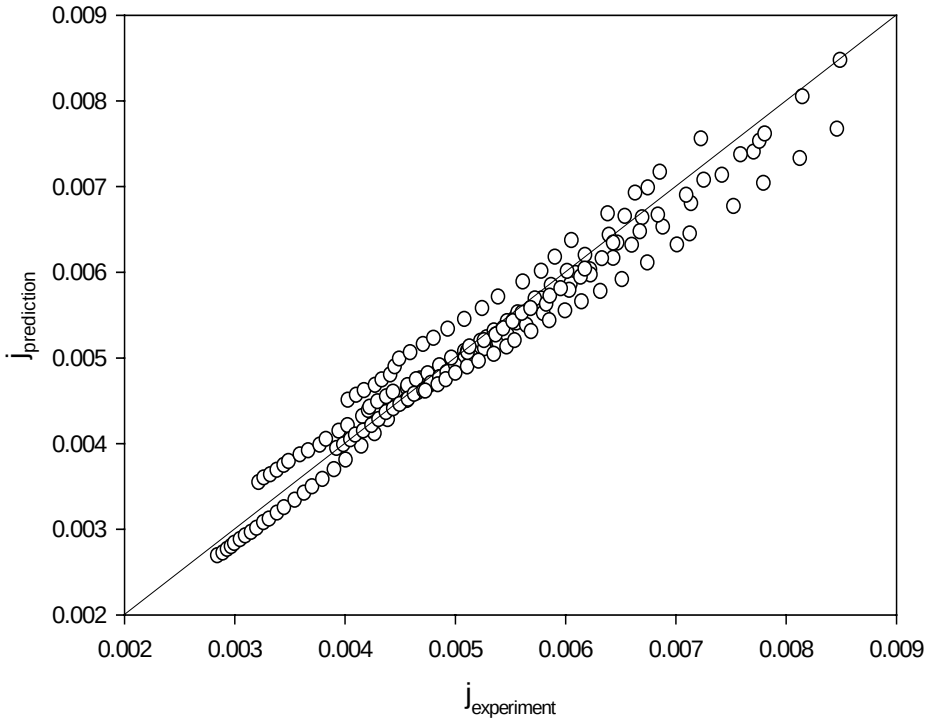

Figure 40. Performance of Equation (88).

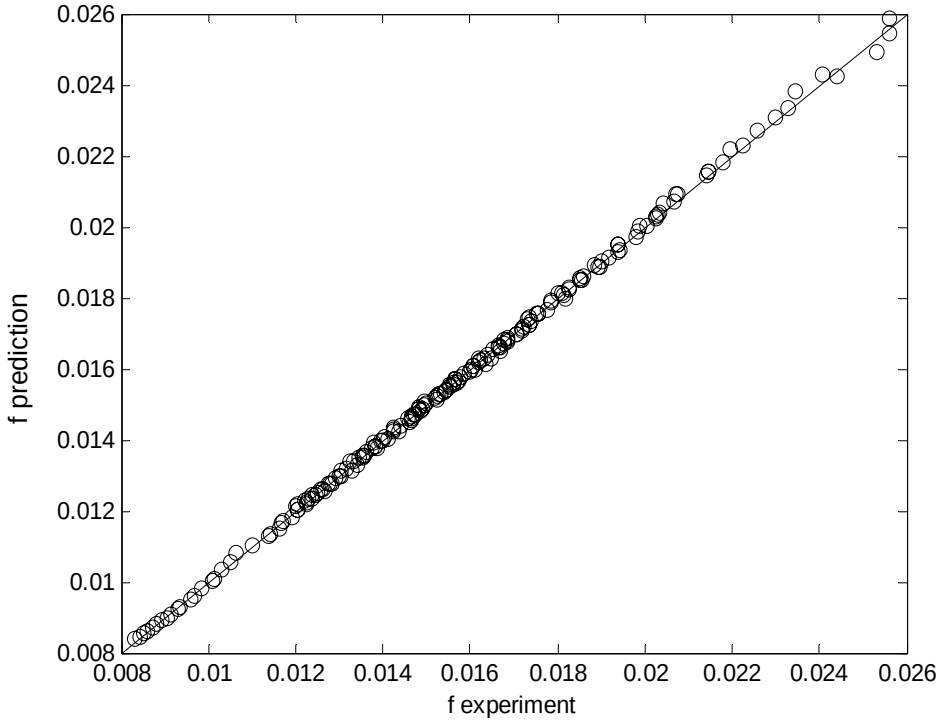

Figure 41. Performance of the f_4LS_1LIN ANN Trained With 50% Data.

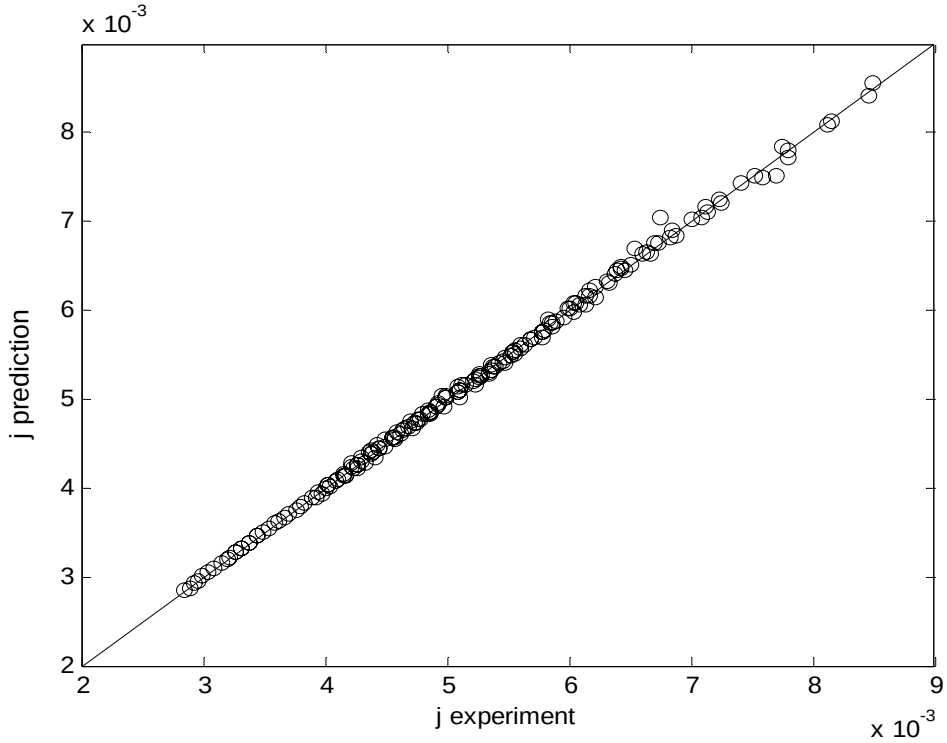

Figure 42. Performance of the j_4LS_1LIN ANN Trained With 50% Data.

V.D Assessment of the Networks' Ability to Generalize

The ANNs developed so far were trained with 50% of data from all tubes. One can postulate that such networks only learn to "interpolate" between the *Re* numbers they were trained with and are unable to predict the performance of unknown geometries. The current section attempts to prove that the 4-1 networks are indeed able to generalize.

Table 9 delineates the mean squared errors (*MSE*) of f_4LS_1LIN and j_4LS_1LIN networks trained with data from 2, 3, 4, 5, and 6 tubes and evaluated with all of the experimental data (8 tubes). Table 9 implies that the ANNs trained with selected tube data performed worse than the networks trained with 50% of data from all 8 tubes (see Table 8). However, if enough tubes were provided for training, the ANNs performed better than correlations (87) and (88). As expected, the network performance generally improved as additional tubes were put in the training basket. In the case of the f_4LS_1LIN network, 6 training tubes were needed to obtain satisfactory performance. The j_4LS_1LIN network was more perceptive and showed outstanding results with 4 training tubes. The networks' performance was sensitive to the randomly-generated initial guess, so the training procedure was repeated 10 to 20 times for each case, and only the best results were considered.

Table 9. *MSE*'s of Networks Trained with Selected Tube Data.

Training Tubes	***MSE***	
	f_4LS_1LIN	**j_4LS_1LIN**
1 and 5	1.321×10^{-5}	3.329×10^{-7}
1, 3, and 5	9.290×10^{-7}	2.324×10^{-7}
1, 3, 5, and 7	6.438×10^{-7}	8.794×10^{-9}
1, 3, 4, 5, and 7	7.060×10^{-7}	1.668×10^{-8}
1, 3, 4, 5, 7, and 8	4.713×10^{-8}	6.442×10^{-9}

The results summarized in Table 9 prove that the 4LS-1LIN networks recommended in the previous section are able to generalize and correctly predict the performance of unknown geometries. Additional details including performance and training curves of the Table 9 networks are given in APPENDIX A.

V.E Evaluation of *f*- and *j*- Networks with Experimental Data of Webb et al. (2000)

In section IV.H, equations (87) and (88) were evaluated with the experimental data of Webb et al. (2000). In this section, the Webb et al. (2000) experimental data are used to evaluate the performance of two f_4LS_1LIN and j_4LS_1LIN networks. Because of their superior performance on the current data set, ANNs trained with 50% of experimental data from all tubes and ANNs trained with 6 out of 8 tubes were chosen for evaluation. The evaluation results are summarized in Table 10.

Table 10. Evaluation of *f*- and *j*- Networks with Data of Webb et al. (2000).

f			***j***		
ANN	***MSE***	**Performance shown on**	**ANN**	***MSE***	**Performance shown on**
f_4LS_1LIN (trained w/ 50% of data from all tubes)	1.216×10^{-5}	Figure 43	j_4LS_1LIN (trained w/ 50% of data from all tubes)	4.600×10^{-6}	Figure 45
f_4LS_1LIN (trained w/ tubes 1, 3, 4, 5, 7, and 8)	2.756×10^{-5}	Figure 44	j_4LS_1LIN (trained w/ tubes 1, 3, 4, 5, 7, and 8)	4.198×10^{-6}	Figure 46

The first conclusion drawn from the inspection of the figures listed in Table 10 is that the neural networks do not predict the data of Webb et al. (2000) very well. In fact, the mean squared errors (*MSE*) associated with the neural networks are in most cases higher than the ones associated with using equations (87) and (88) [$MSE = 1.345 \times 10^{-5}$ using equation (87) and $MSE = 3.886 \times 10^{-6}$ using equation (88)]. Furthermore, as was the

case with the power-law correlations, Webb et al.'s (2000) friction data are over-predicted and heat transfer data under-predicted by the neural networks. Basically, there seems to be a difference in the experimental results between the current study and that of Webb et al. (2000). Finally, Table 10 reveals that there is no clear advantage of using networks trained with all of the tubes or with data from selected tubes.

V.F Evaluation of *f*- and *j*- Networks with Experimental Data of Jensen and Vlakancic (1999)

In section IV.I, equations (87) and (88) were evaluated with experimental data of Jensen and Vlakancic (1999). In this section, the Jensen and Vlakancic (1999) experimental data are used to evaluate the performance of the f_4LS_1LIN and j_4LS_1LIN networks. As in the previous section, ANNs trained with 50% of experimental data from all tubes and ANNs trained with 6 out of 8 tubes were chosen for evaluation. The evaluation results are summarized in Table 11.

Table 11. Evaluation of *f*- and *j*- Networks with Data of Jensen and Vlakanic (1999).

f			***j***		
ANN	***MSE***	**Performance shown on**	**ANN**	***MSE***	**Performance shown on**
f_4LS_1LIN (trained w/ 50% of data from all tubes)	2.798×10^{-4}	Figure 47	j_4LS_1LIN (trained w/ 50% of data from all tubes)	5.389×10^{-6}	Figure 49
f_4LS_1LIN (trained w/ tubes 1, 3, 4, 5, 7, and 8)	1.995×10^{-5}	Figure 48	j_4LS_1LIN (trained w/ tubes 1, 3, 4, 5, 7, and 8)	4.709×10^{-6}	Figure 50

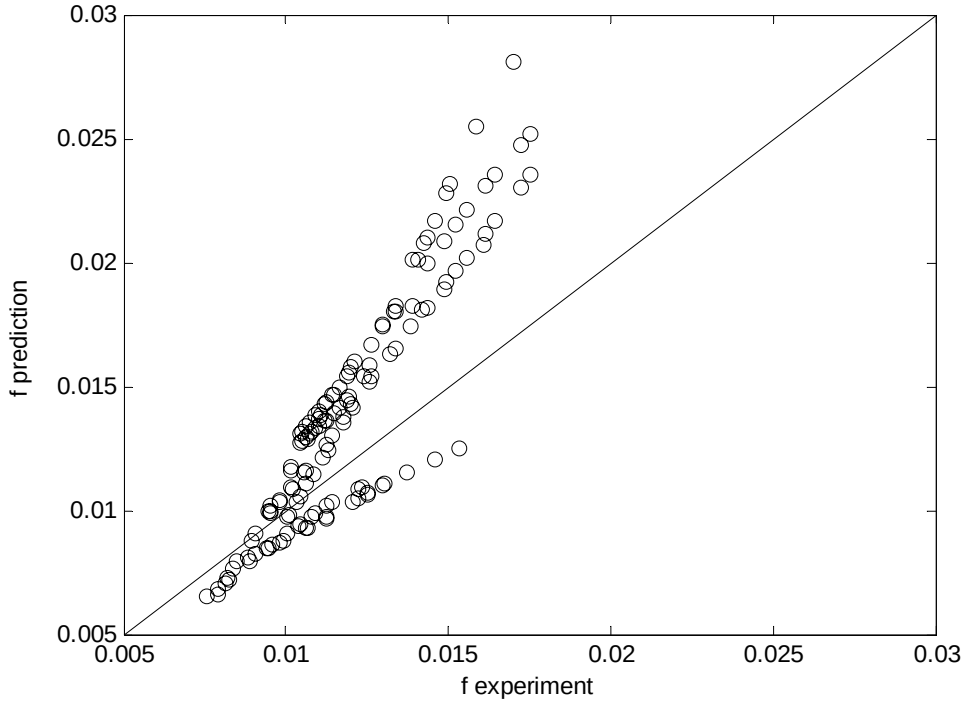

Figure 43. Evaluation of the f_4LS_1LIN ANN (Trained w/ 50% Data) with Data of Webb et al. (2000).

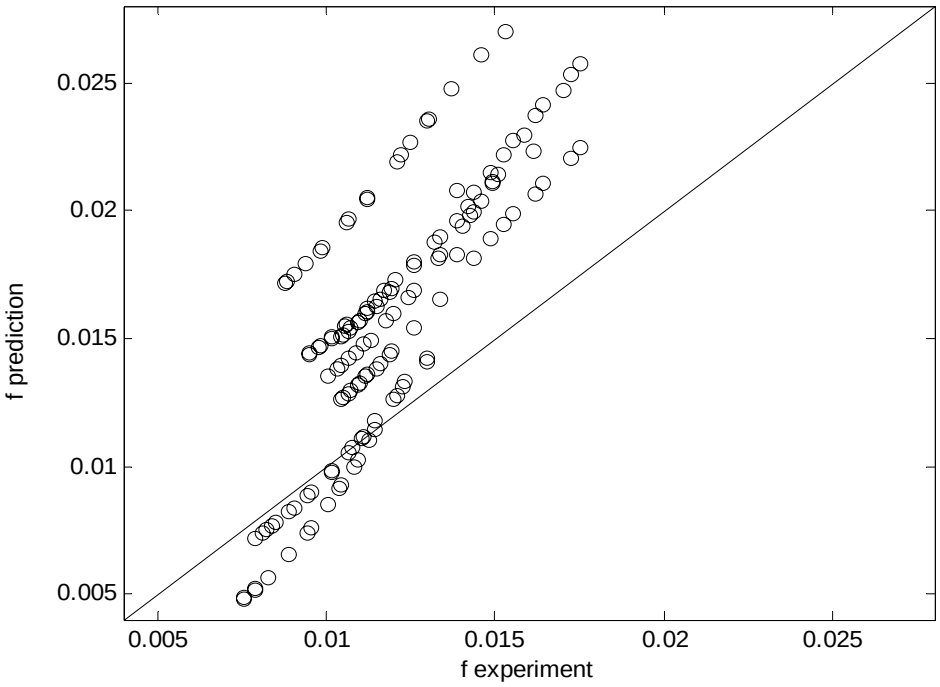

Figure 44. Evaluation of the f_4LS_1LIN ANN (Trained w/ Tubes 1, 3, 4, 6, 7, and 8) with Data of Webb et al. (2000).

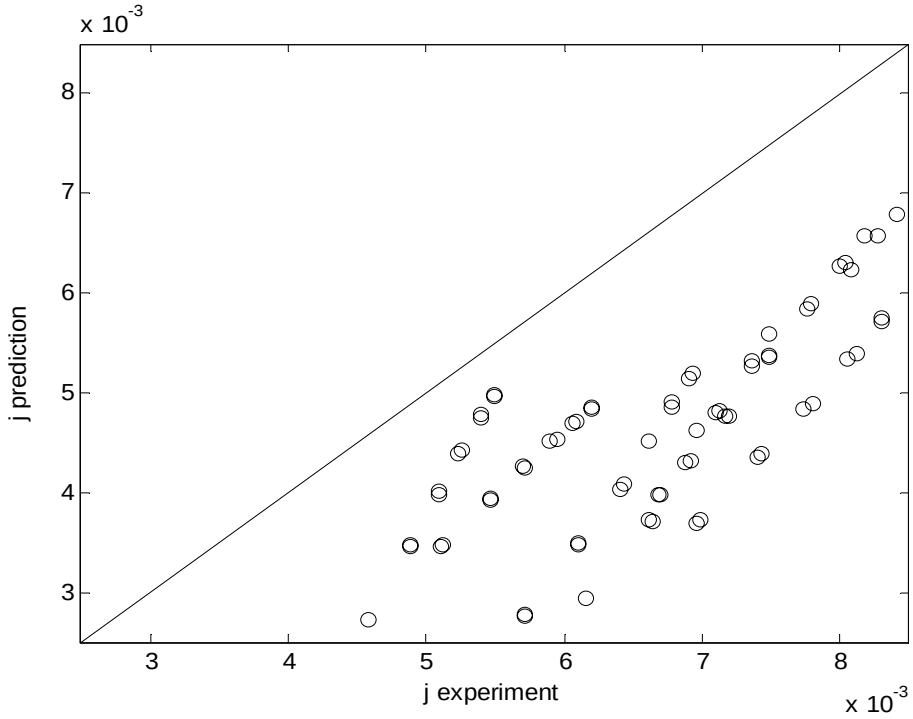

Figure 45. Evaluation of the j_4LS_1LIN ANN (Trained w/ 50% Data) with Data of Webb et al. (2000).

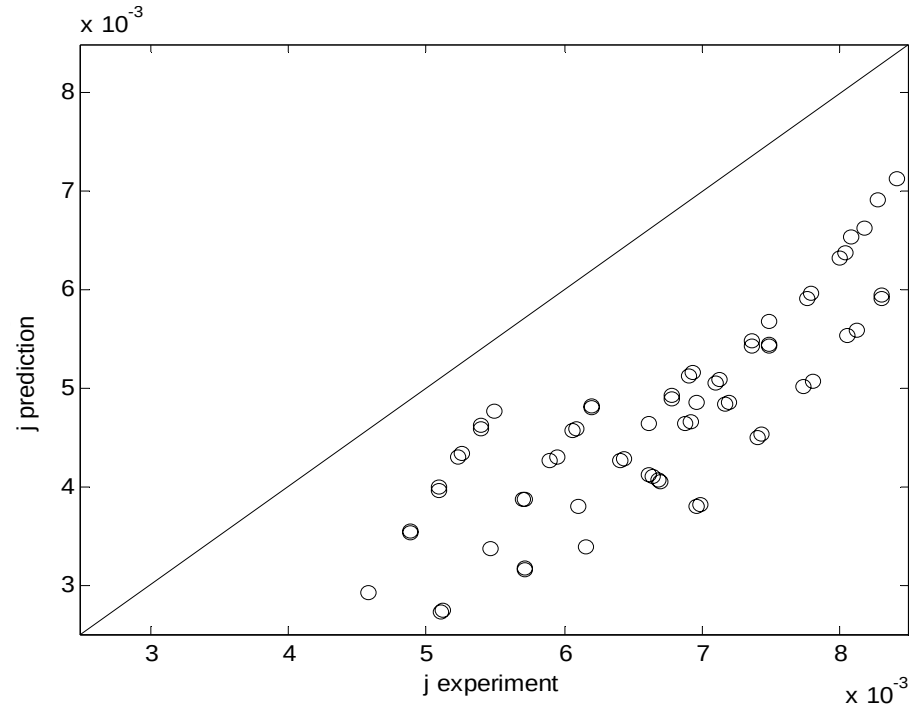

Figure 46. Evaluation of the j_4LS_1LIN ANN (Trained w/ Tubes 1, 3, 4, 6, 7, and 8) with Data of Webb et al. (2000).

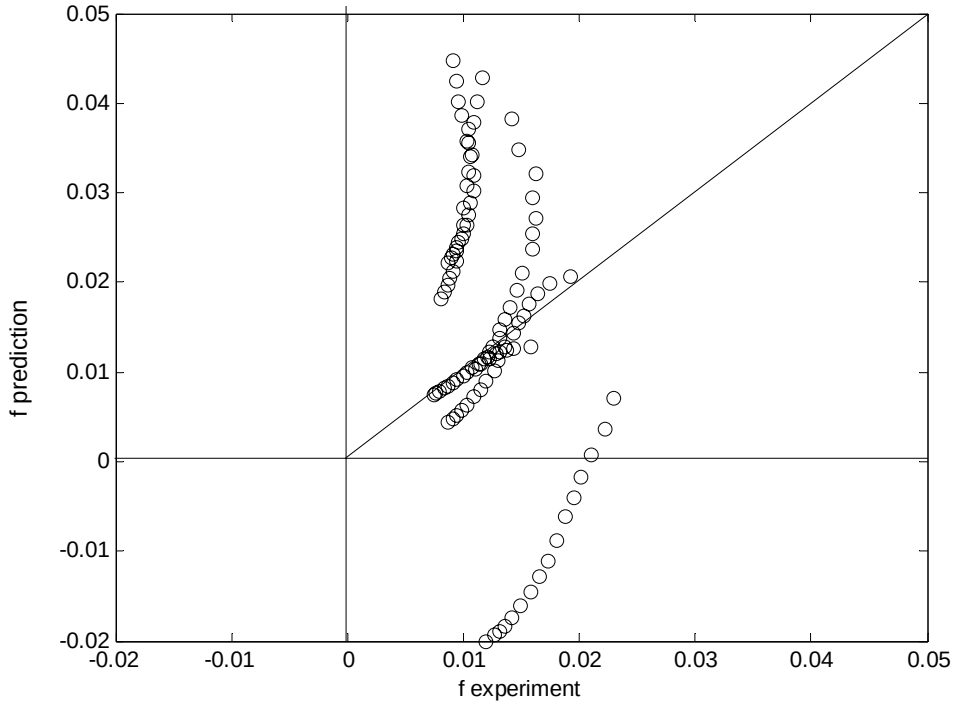

Figure 47. Evaluation of the f_4LS_1LIN ANN (Trained w/ 50% Data) with Data of Jensen and Vlakancic (1999).

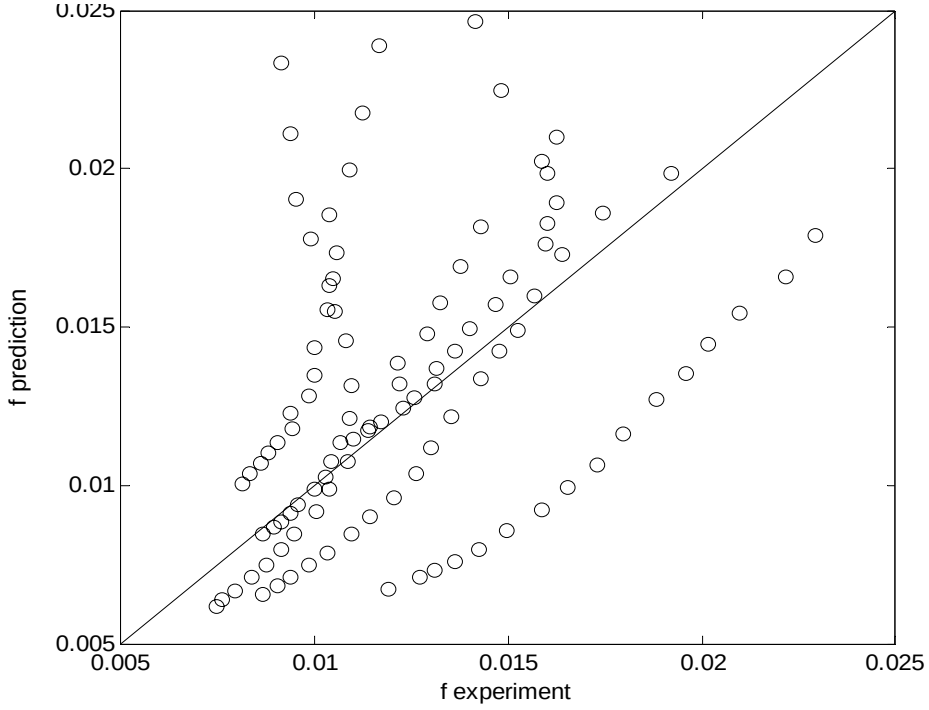

Figure 48. Evaluation of the f_4LS_1LIN ANN (Trained w/ Tubes 1, 3, 4, 6, 7, and 8) with Data of Jensen and Vlakancic (1999).

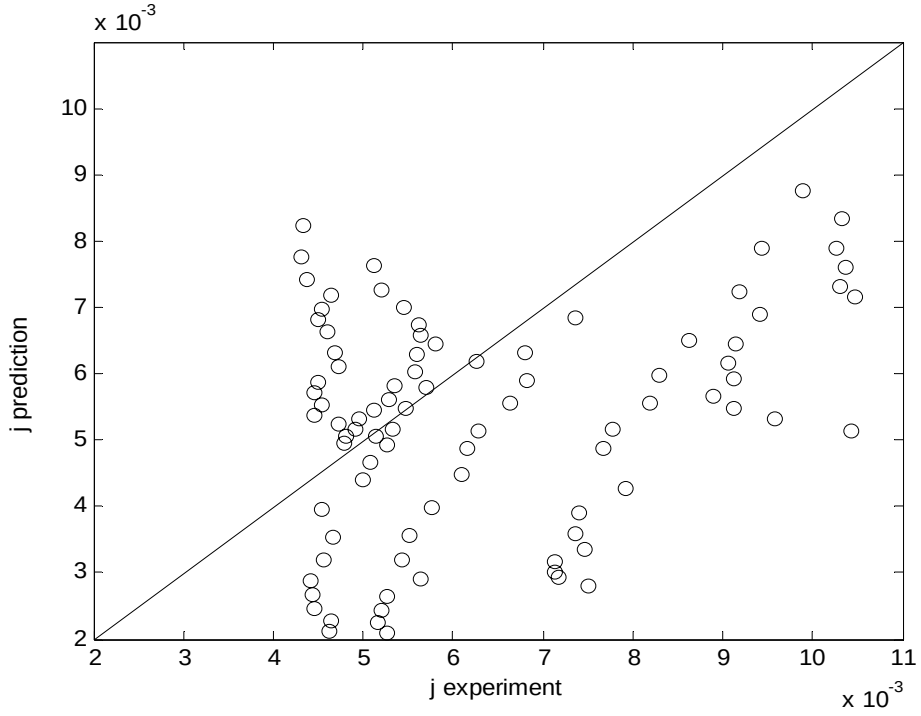

Figure 49. Evaluation of the j_4LS_1LIN ANN (Trained w/ 50% Data) with Data of Jensen and Vlakancic (1999).

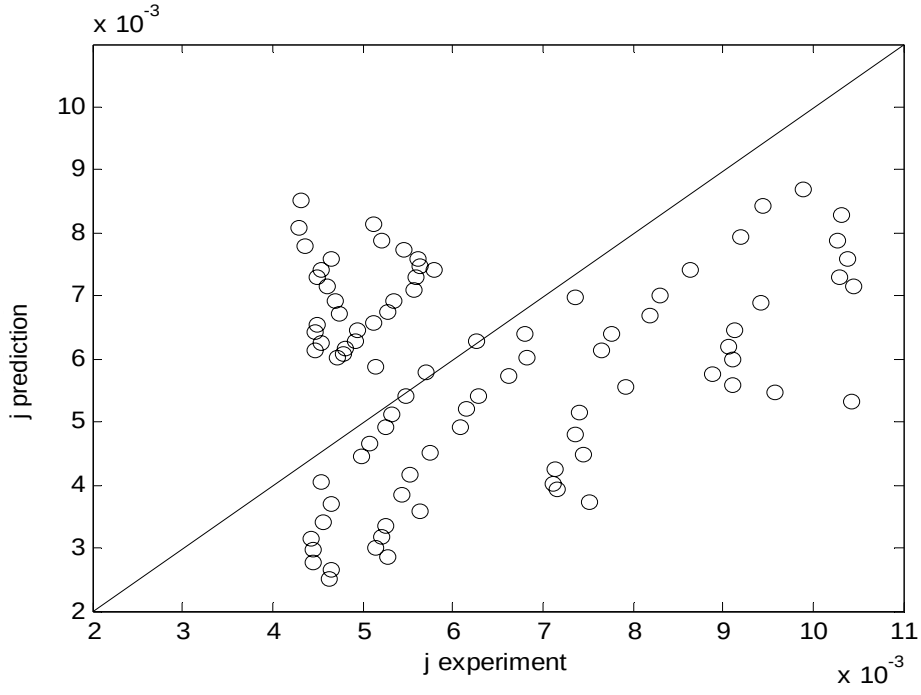

Figure 50. Evaluation of the j_4LS_1LIN ANN (Trained w/ Tubes 1, 3, 4, 6, 7, and 8) with Data of Jensen and Vlakancic (1999).

Table 11 implies that the ANNs trained with data of tubes 1, 3, 4, 5, 7, and 8 predict Jensen and Vlakancic's (1999) data slightly better than equations (87) and (88) in terms of the mean squared errors [$MSE = 2.666 \times 10^{-5}$ using equation (87) and $MSE = 5.355 \times 10^{-6}$ using equation (88)]. Generally though, the performance of the ANNs on the Jensen and Vlakancic (1999) data was poor. The f_4LS_1LIN network trained with 50% of data from all tubes predicted negative friction factors for tube JV3 and over-predicted tube JV4's friction by as much as 400% (see Figure 47). Finally, the errors associated with the *f*- and *j*-networks suggest that the results of Jensen and Vlakancic (1999) demonstrate a different Reynolds number dependence than the current study results.

V.G ANNs Trained with a Combined Database

A common engineering practice is to average multiple measurements to obtain the "best" value. Therefore, a network trained with a database combining the results of Jensen and Vlakancic (1999), Webb et al. (2000), and the current study would be a useful prediction tool.

To create such a tool, an f_4LS_1LIN and a j_4LS_1LIN network were trained with 50% of data points (every other Reynolds number) from a database combining the experimental results of Webb et al. (2000), Jensen and Vlakancic (1999), and the current study. The performance of these two networks is depicted respectively on Figure 51 and Figure 52, with additional details included in APPENDIX A. The mean squared errors (*MSE*) of the f_4LS_1LIN and j_4LS_1LIN networks are 4.553×10^{-7} and 7.671×10^{-8}, respectively, and are lower than the ones associated with equations (87) and (88) applied to any of the data sets. The network prediction errors were also plotted as a function of

Re^* on Figure 53 for the friction factor and on Figure 54 for the Colburn j-factor. Both figures show that the majority of data points from the combined set are predicted within plus or minus 10%. Based on the information presented so far, the f_4LS_1LIN and j_4LS_1LIN networks trained with 50% of data points from the combined database appear to be the best prediction tool friction and heat transfer in helically-ribbed tubes.

The current chapter showed that ANNs perform extremely well on the data sets that they are trained with, but poorly on independent data, with experimental discrepancies being a probable reason for disagreement. Several ANNs were capable of outperforming algebraic correlations, but the key aspect (other than the network's geometry and node functions) affecting the network performance was the selection of the training data set. This selection must be carried out carefully, so that there is enough variation in the inputs for the network to establish trends. The more data is used in training process the better the network performance. However, using too many data points during the training process can affect the network's ability to generalize.

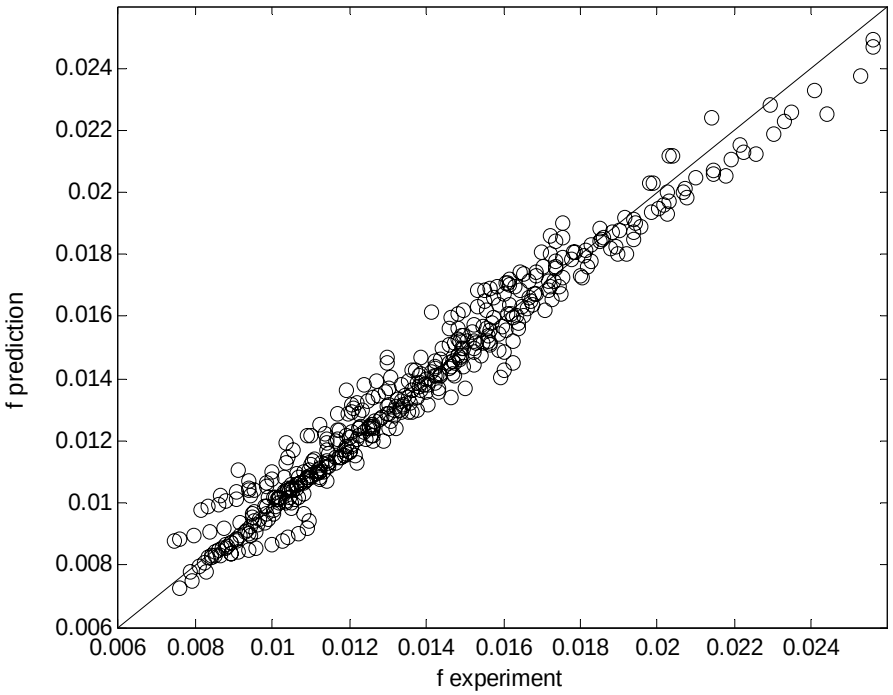

Figure 51. Performance of f_4LS_1LIN ANN Trained with 50% Combined Data.

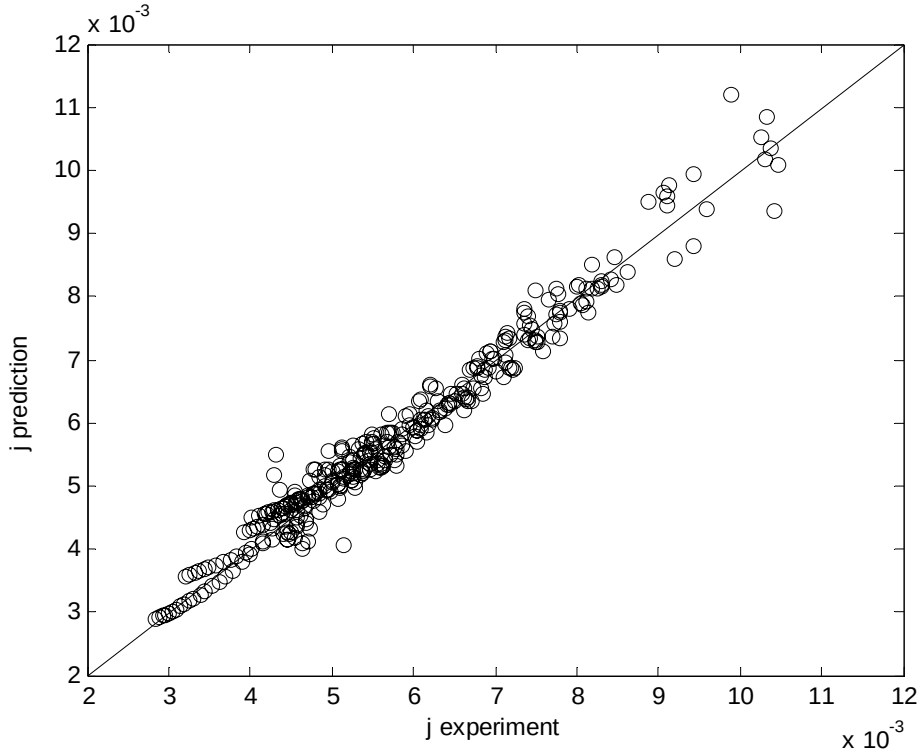

Figure 52. Performance of j_4LS_1LIN ANN Trained with 50% Combined Data.

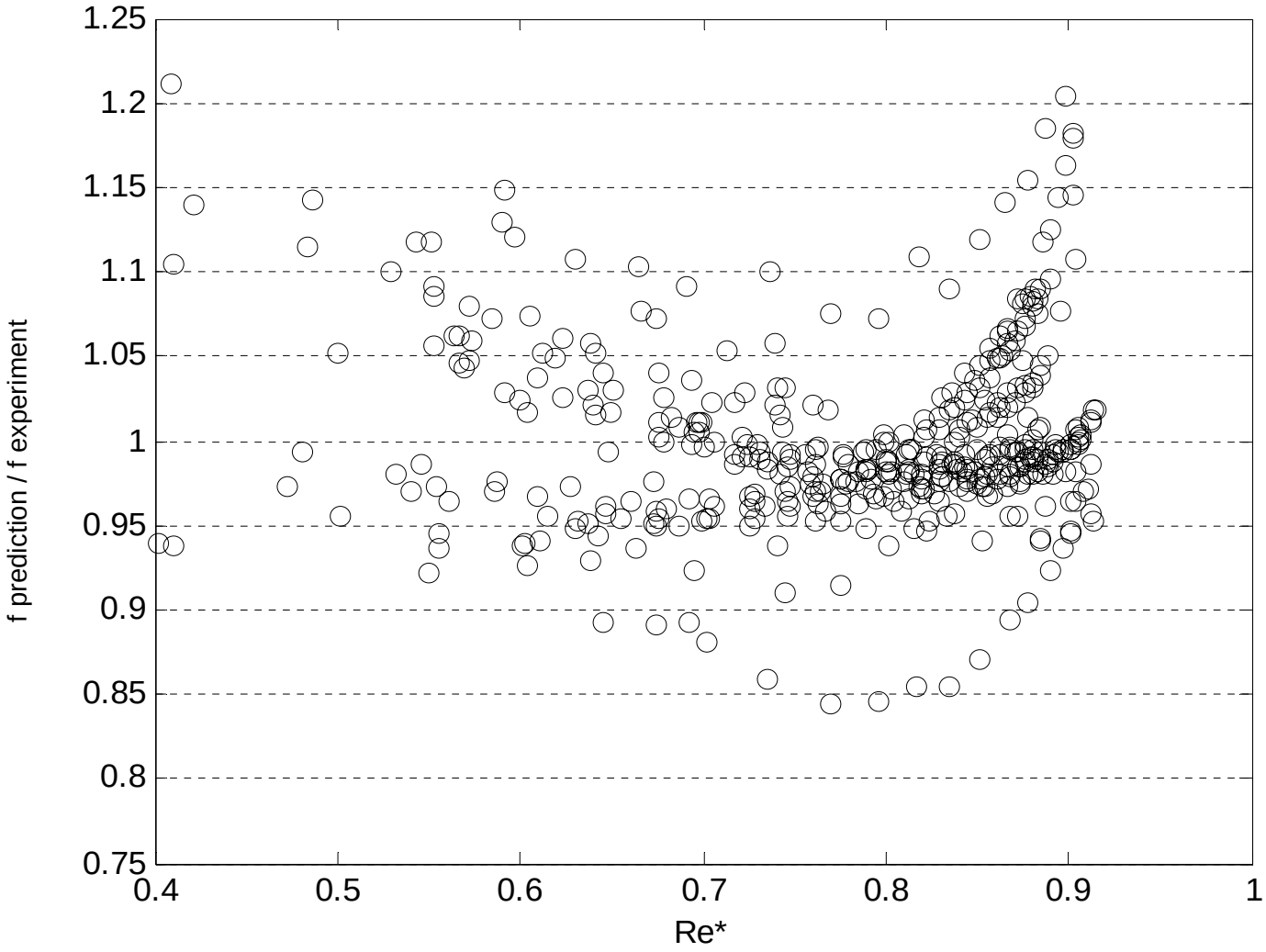

Figure 53. f_4LS_1LIN (Trained with 50% Combined Data) Prediction Errors.

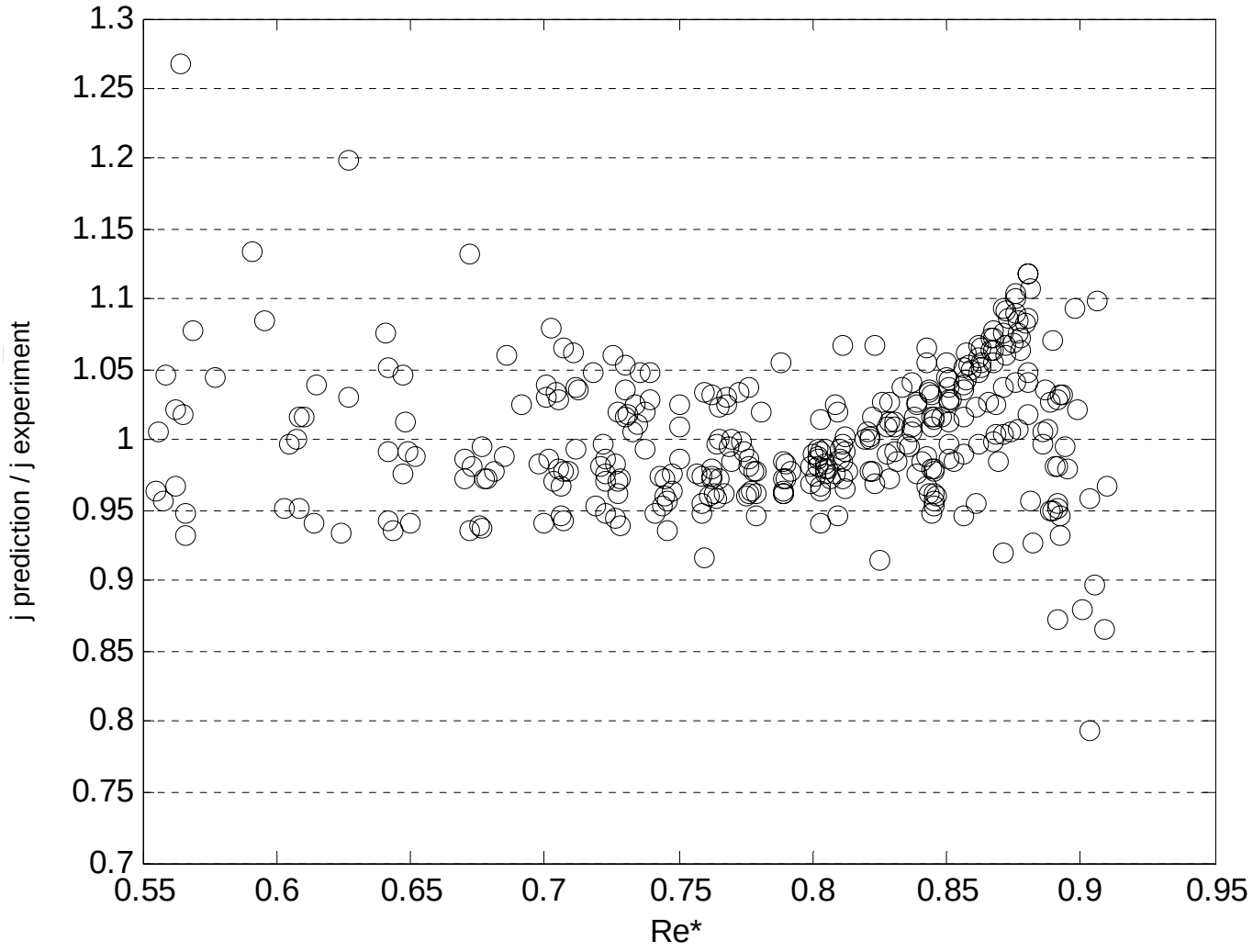

Figure 54. j_4LS_1LIN (Trained with 50% Combined Data) Prediction Errors.

CHAPTER VI

CONCLUSIONS

VI.A Synopsis

This dissertation first introduced heat transfer enhancements techniques. A literature review of heat transfer and friction in tubes with helical enhancements (indentations, ribs, fins, wire inserts, or spiral tapes) was performed, and available prediction methods were reported. The current understanding of complex secondary flows in the interfin region was discussed. An introduction to artificial neural networks (ANNs) was presented, and a literature review of the use of ANNs in heat transfer and fluid flow was conducted.

Next, heat transfer coefficients and friction factors were determined experimentally for eight helically-finned tubes and one smooth tube using liquid water at 12 000 < Re_i < 60 000. An uncertainty analysis was completed and plain-tube results were compared to the Blasius and Dittus-Boelter equations with satisfactory agreement. The highest j-factor was achieved by tube 8 (N_s = 45, α = 48°, e/D = 0.0244) and the lowest f-factor by tube 1 (N_s = 10, α = 48°, e/D = 0.0244). Power-law correlations for f and j-factors were developed using a least-squares regression. The performance of the correlations was evaluated with independent data of Webb et al. (2000) and Jensen and Vlakancic (1999).

Several ANNs were trained with 50% of friction and heat transfer data points from all tubes to determine the optimal network architecture. The best architecture was a two-layer network with four log-sigmoid nodes in the first layer and one linear node in the output layer (networks f_4LS_1LIN and j_4LS_1LIN). Then, this architecture was trained with friction and heat transfer data of 2, 3, 4, 5, then 6 tubes to check whether or not the ANN had the ability to generalize. Networks trained with 50% of data points from all tubes and networks trained with data of 6 tubes were evaluated with independent data of Webb et al. (2000) and Jensen and Vlakancic (1999). Finally, a friction network and a heat transfer network were trained with 50% of combined experimental data of Webb et al. (2000), Jensen and Vlakancic (1999), and the current study. The performance of these two networks was reported graphically and in terms of the mean squared error.

VI.B Recommendations

Measurements of friction and heat transfer imply that tube 8 (N_s = 45, α = 48°, e/D = 0.0244) can be recommended for heat exchange applications because of its high j-factors and moderate f-factors at all Reynolds numbers. Conversely, the considerable increase in Nusselt number with respect to the friction factor shown by tube 3 (N_s = 30, α = 48°, e/D = 0.0243) does not justify the use of this enhancement geometry.

The various network architectures tested in CHAPTER V suggest the 4-1 feed-forward network with log-sigmoid node functions in the first layer and a linear node function in the output layer to be the most advantageous architecture to use for prediction of helically-ribbed tube performance. The 4LS_1LIN networks were accurate and were able to generalize, given adequate training data. Problems were encountered with data of

other researchers, but these problems were not necessarily the network's fault. The three data sets contain possible bias errors, and ANNs learn to predict data without being capable of isolating measurement errors. Moreover, the power-law correlations (obtained with a least-squares regression that takes into account 100% of data points) also lacked appropriate accuracy.

Considering the limited availability of heat transfer and friction data in helically-finned tubes, the recommended prediction tool for this type of tube is the f_4LS_1LIN and j_4LS_1LIN network trained with the combined results of Webb et al. (2000), Jensen and Vlakancic (1999), and the current study. These two networks are fully described in APPENDIX A.

The ultimate ANN would be trained with thousands of accurately-measured data points from hundreds of different tubes and could predict friction factors and Colburn *j*-factors with virtually no error. Hence, neural network applications are well-suited for manufacturers of heat exchange equipment, who can tap into their extensive databases to train state-of-the-art ANNs.

VI.C Future Work

Disagreements in experimental results of Webb et al. (2000), Jensen and Vlakancic (1999), and the current study imply that a broader database of heat transfer and friction characteristics of flow in helically-ribbed tubes is desirable. Moreover, due to the gaps in understanding of the flow in spirally-finned tubes, more research should be performed on the influence of geometric parameters on flow patterns, especially in the

interfin region. Such research could be achieved with modern flow visualization techniques or perhaps proven computational fluid dynamics (CFD) tools.

Other artificial intelligence techniques such as genetic algorithms are also good candidates for fitting data of helically-finned tubes. In fact, preliminary efforts have already commenced at Mississippi State University to utilize genetic algorithms to determine optimal mathematical expressions suited for curve fits of friction and heat transfer data in helically-ribbed tubes, and initial results look promising.

Finally, prediction tools developed in the current study can be used to complement existing optimization techniques in discovering the ultimate helical fin geometry (that is one with the highest heat transfer coefficient but lowest friction factor). In such endeavors, the advantage of ANNs' low prediction errors and applicability of matrix algebra are valuable.

REFERENCES

Ashforth-Frost, S., Fontama, V.N., Jambunathan, K., and Hartle, S.L., "The Role of Neural Networks in Fluid Mechanics and Heat Transfer," Proceedings of the 1995 IEEE Instrumentation and Measurement Technology Conference, Vol. 1, April 1995, 6-9.

Belyakov, I.I., Migai, V.K., and Sokolov, V.V., "Heat Transfer and Hydraulic Resistance of Tubes with Internal Helical Finning," Thermal Engineering, Vol. 36, No. 8, August 1989, 444-448.

Briggs, D.E., and Young, E.H., Modified Wilson Plot Techniques for Obtaining Heat Transfer Correlation for Shell-and-Tube Heat Exchangers, Presented at the 10th National Heat Transfer Conference in Philadelphia, Pennsylvania, American Institute of Chemical Engineers, August 11-14, 1968, 2-25.

Carnavos, T.C., "Heat Transfer Performance of Internally Finned Tubes in Turbulent Flow," Heat Transfer Engineering, Vol. 1, No. 4, 1980, 32-37.

Chen, X.D., Xu, X.Y., Nguang, S.K., and Bergles, A.E., "Characterization of the Effect of Corrugation Angles on Hydrodynamic and Heat Transfer Performance of Four-Start Spiral Tubes," Transactions of the ASME: Journal of Heat Transfer, Vol. 123, 2001, 1149-1158.

Coleman, H.W., and Steele, W.G., Experimentation and Uncertainty Analysis for Engineers, John Wiley & Sons, New York, 1999.

Date, A.W., "Prediction of Fully-Developed Flow in a Tube Containing a Twisted-Tape," International Journal of Heat and Mass Transfer, Vol. 17, 1974, 845-859.

Diaz, G., Sen, M., McClain, R.L., and Yang, K.T., "On-line Training of Artificial Neural Networks for Control of a Heat Exchanger Test Facility," Proceedings of the National Heat Transfer Conference, Vol. 1, 2001a, 359-365.

Diaz, G., Sen, M., Yang, K.T., and McClain, R.L., "Dynamic Prediction and Control of Heat Exchangers Using Artificial Neural Networks," International Journal of Heat and Mass Transfer, Vol. 44, 2001b, 1671-1679.

Diaz, G., Sen, M., Yang, K.T., and McClain, R.L., "Simulation of Heat Exchanger Performance by Artificial Neural Networks," HVAC&R Research, Vol. 5, No. 3, 1999, 195-208.

Diaz, G., Yanes, J., Sen, M., Yang, K.T., and McClain, R.L., "Analysis of Data from Single-row Heat Exchanger Experiments Using an Artificial Neural Network," American Society of Mechanical Engineers Fluids Engineering Division (FED), Vol. 242, 1996, 45-52

Dipprey, D.F., and Sabersky, R.H., "Heat and Momentum Transfer in Smooth and Rough Tubes at Various Prandtl Numbers," International Journal of Heat and Mass Transfer, Vol. 6, 1963, 329-353.

Ganeshan, S., and Rao, M.R., "Studies of Thermohydraulics of Single- and Multi-start Spirally Corrugated Tubes for Water and Time-independent Power Law Fluids," International Journal of Heat and Mass Transfer, Vol. 25, No. 7, 1982, 1013-1022.

Gee, D.L., and Webb, R.L., "Forced Convection Heat Transfer in Helically Rib-roughened Tubes," International Journal of Heat and Mass Transfer, Vol. 23, 1980, 1127-1136.

Ghajar, A.J., Tam, L.M., and Tam, S.C., "Improved Heat Transfer Correlation in the Transition Region for a Circular Tube with Three Inlet Configurations Using Artificial Neural Networks," Heat Transfer Engineering, Vol. 25, No. 2, 2004, 30-40.

Goldberg, U., Peroomain, O., and Chakravarthy, S., "A Wall-distance-free k-ε Model with Enhanced Near-wall Treatment," Transactions of the ASME: Journal of Fluids Engineering, Vol. 120, No. 3, 1998, 457-462.

Gupta, R.K., and Rao, M.R., Heat Transfer and Friction Characteristics of Newtonian and Power-law Type of Non-newtonian Fluids in Smooth and Spirally Corrugated Tubes, Presented at the 18th National Heat Transfer Conference in San Diego, California, American Society of Mechanical Engineers, August 6-8, 1979, 103-113

Hagan, M., Demuth, H., and Beale M., Neural Network Design, Martin/Hagan (Distributed by the University of Colorado), 1996.

Han, J.C., Glicksman, L.R., and Rohsenow, W.M., "An Investigation of Heat Transfer and Friction for Rib-Roughened Surfaces," International Journal of Heat and Mass Transfer, Vol. 21, 1978, 1143-1156.

Haykin, S., Neural Networks: A Comprehensive Foundation, Macmillan, New York, 1994.

Islamoglu, Y., "A New Approach for the Prediction of the Heat Transfer Rate of the Wire-on-tube Type Heat Exchanger - Use of an Artificial Neural Network Model," Applied Thermal Engineering, Vol. 23, 2003, 243-249.

Islamoglu, Y., and Kurt, A., "Heat Transfer Analysis Using ANNs with Experimental Data for Air Flowing in Corrugated Channels," International Journal of Heat and Mass Transfer, Vol. 47, 2004, 1361-1365.

Ivanović, M., Prediction of Flow and Heat Transfer in Internally Finned Tubes, Ph.D. Thesis, University of Minnesota, Twin Cities, July 1978.

Jambunathan, K., Hartle, S.L., Ashforth-Frost, S., and Fontama, V.N., "Evaluating Convective Heat Transfer Coefficients Using Neural Networks," International Journal of Heat and Mass Transfer, Vol. 39, No. 11, 1996, 2329-2332.

Jensen M.K., and Vlakancic, A., "Experimental Investigation of Turbulent Heat Transfer and Fluid Flow in Internally Finned Tubes," International Journal of Heat and Mass Transfer, Vol. 42, 1999, 1343-1351.

Kalogirou, S.A., "Applications of Artificial Neural Networks in Energy Systems. A Review," Energy Conversion & Management, Vol. 40, 1999, 1073-1087.

Kays, W.M., and Crawford, M.E., Convective Heat and Mass Transfer, McGraw-Hill, New York, 1980, 40.

Kelleher, M.D., Cronley, T.J., Yang, K.T., and Sen, M., "Using Artificial Neural Networks to Develop a Predictive Method from Complex Experimental Heat Transfer Data," American Society of Mechanical Engineers Heat Transfer Division (HTD), Vol. 369, No. 5, 2001, 11-34.

Kim, J.H., Jansen, K.E., and Jensen, M.K., "Simulation of Three-dimensional Incompressible Turbulent Flow Inside Tubes With Helical Fins," Numerical Heat Transfer, Part B, Vol. 46, 2004, 195-221.

Lam, C.K.G, and Bremhorst, K.A., "A Modified Form of k-ε Model for Predicting Wall Turbulence," Transactions of the ASME: Journal of Fluids Engineering, Vol. 103, No. 3, 1981, 456-460.

Levenberg, K., "A Method for the Solution of Certain Problems in Least Squares," Quarterly of Applied Mathematics, Vol. 2, 1944, 164-168.

Li, H.M., Ye, K.S., Tan, Y.K., and Deng, S.J., "Investigation on Tube-side Flow Visualization, Friction Factors, and Heat Transfer Characteristics of Helical-ridging Tubes," Heat Transfer 1982; Proceedings of the 7th International Heat Transfer Conference, Munich, Vol. 3, 1982, 75-80.

Marquardt, D., "An Algorithm for Least-Squares Estimation of Nonlinear Parameters," SIAM Journal on Applied Mathematics, Vol. 11, 1963, 431-441.

Mehrotra, K., Mohan, C.M., and Ranka, S., Elements of Artificial Neural Networks (Complex Adaptive Systems), The MIT Press, Cambridge, Mass., 1996.

Menter, F.R., "Two-equation Eddy-viscosity Turbulence Models for Engineering Applications," AIAA Journal, Vol. 32, No. 8, 1994, 1598-1605.

Migai, V.K., "Friction and Heat Exchange in a Swirled Stream Inside a Pipe," Izvestiya Akademii Nauk SSSR, Energetika i Transport, No. 5, 1966, 143-151.

Migai, V.K., "Intensification of Convective Heat Transfer in Tubes with Swirl Generators," Thermal Engineering, Vol. 15, No. 11, 1968, 46-49.

Migai, V.K., and Uporov, A.P., "Calculation of Heat Exchange in Pipes with Spiral Sheet Intensifiers," Journal of Engineering Physics, Vol. 37, No. 6, December 1979, 1385-1388.

Nakayama M., Takahashi, K., and Daikoku, T., "Spiral Ribbing to Enhance Single-phase Heat Transfer Inside Tubes," Proceedings of the ASME-JSME Thermal Engineering Joint Conference, Honolulu, 1983, 365-372.

Newson, I.H., and Hodgson, T.D., "The Development of Enhanced Heat Transfer Condenser Tubing," Desalination, Vol. 14, 1974, 291-323.

Nikuradse, J., Laws of Flows in Pipes, NACA-TM-1292, 1950.

Pacheco-Vega, A., Sen, M., Yang, K.T., and McClain, R.L., "Heat Rate Predictions in Humid Air-water Heat Exchangers Using Correlations and Neural Networks," Transactions of the ASME: Journal of Heat Transfer, Vol. 123, No. 3, 2001a, 348-354.

Pacheco-Vega, A., Sen, M., Yang, K.T., and McClain, R.L., "Neural Network Analysis of Fin-tube Refrigerating Heat Exchanger with Limited Experimental Data," International Journal of Heat and Mass Transfer, Vol. 44, 2001b, 763-770.

Pacheco-Vega, A., Sen, M., Yang, K.T., and McClain, R.L., "Prediction of Humid Air Heat Exchanger Performance Using Artificial Neural Networks," American Society of Mechanical Engineers Heat Transfer Division (HTD), Vol. 364-3, 1999, 307-314.

Ravigururajan, T.S., "A Comparative Study of Thermal Design Correlations for Turbulent Flow in Helical-Enhanced Tubes," Heat Transfer Engineering, Vol. 20, No. 1, 1999, 54-70.

Ravigururajan, T.S., and Bergles, A.E., "Visualization of Flow Phenomena Near Enhanced Surfaces," Transactions of the ASME: Journal of Heat Transfer, Vol. 116, February 1994, 54-57.

Scalabrin, G., and Piazza, L., "Analysis of Forced Convection Heat Transfer to Supercritical Carbon Dioxide Inside Tubes Using Neural Networks," International Journal of Heat and Mass Transfer, Vol. 46, 2003, 1139-1154.

Schlichting, H., Boundary-Layer Theory, 7th ed., McGraw Hill, St. Louis, 1979.

Sen, M., and Yang, K.T., "Applications of Artificial Neural Networks and Genetic Algorithms in Thermal Engineering" in The CRC Handbook of Thermal Engineering, 2000, 620-661.

Sethumadhavan, R., and Rao, M.R., "Turbulent Flow Friction and Heat Transfer Characteristics of Single- and Multistart Spirally Enhanced Tubes," Transactions of the ASME: Journal of Heat Transfer, Vol. 108, 1986, 55-61.

Shome, B., Experimental and Numerical Investigation of Variable Property/Mixed Convection Laminar Flow in Internally Finned Tubes, Ph.D. Thesis, Rensselaer Polytechnic Institute, Troy, New York, December 1995.

Shome, B., and Jensen, M.K., "Experimental Investigation of Laminar Flow and Heat Transfer in Internally Finned Tubes," Journal of Enhanced Heat Transfer, Vol. 4, No. 1, 1996a, 53-70.

Shome, B., and Jensen, M.K., "Numerical Investigation of Laminar Flow and Heat Transfer in Internally Finned Tubes," Journal of Enhanced Heat Transfer, Vol. 4, No. 1, 1996b, 35-51.

Spalart, P.R., and Allmaras, S.R., "A One-equation Turbulence Model for Aerodynamic Flows," AIAA Paper 92-0439, 1992.

Thibault, J., and Grandjean, B.P.A., "A Neural Network Methodology for Heat Transfer Data Analysis," International Journal of Heat and Mass Transfer, Vol. 34, No. 8, 1991, 2063-2070.

Vicente, P.G., García, A., and Viedma, A., "Experimental Investigation on Heat Transfer and Frictional Characteristics of Spirally Corrugated Tubes in Turbulent Flow at Different Prandtl Numbers," International Journal of Heat and Mass Transfer, Vol. 47, 2004, 671-681.

Webb, R.L., "Performance, Cost Effectiveness, and Water-side Fouling Considerations of Enhanced Tube Heat Exchangers for Boiling Service with Tube-Side Water Flow," Heat Transfer Engineering, Vol. 3, 1982, 84-98.

Webb, R.L, Eckert, E.R.G., and Goldstein, R.J., "Heat Transfer and Friction in Tubes with Repeated-rib Roughness," International Journal of Heat and Mass Transfer, Vol. 14, 1971, 601-617.

Webb, R.L., Narayanamurthy R., and Thors, P., "Heat Transfer and Friction Characteristics of Internal Helical-rib Roughness," Transactions of the ASME: Journal of Heat Transfer, Vol. 122, February 2000, 134-142.

Withers, J.G., "Tube-side Heat Transfer and Pressure Drop for Tubes Having Helical Internal Ridging with Turbulent/Transitional Flow of Single-phase Fluid. Part 1. Single-Helix Ridging," Heat Transfer Engineering, Vol. 2, No. 1, 1980a, 48-58.

Withers, J.G., "Tube-side Heat Transfer and Pressure Drop for Tubes Having Helical Internal Ridging with Turbulent/Transitional Flow of Single-phase Fluid. Part 2. Multiple-Helix Ridging," Heat Transfer Engineering, Vol. 2, No. 2, 1980b, 43-50.

APPENDIX A

NEURAL NETWORKS

A1. Friction Factor Networks Trained with Half of Data Points

- **f_2LS_1LIN**

Training curve

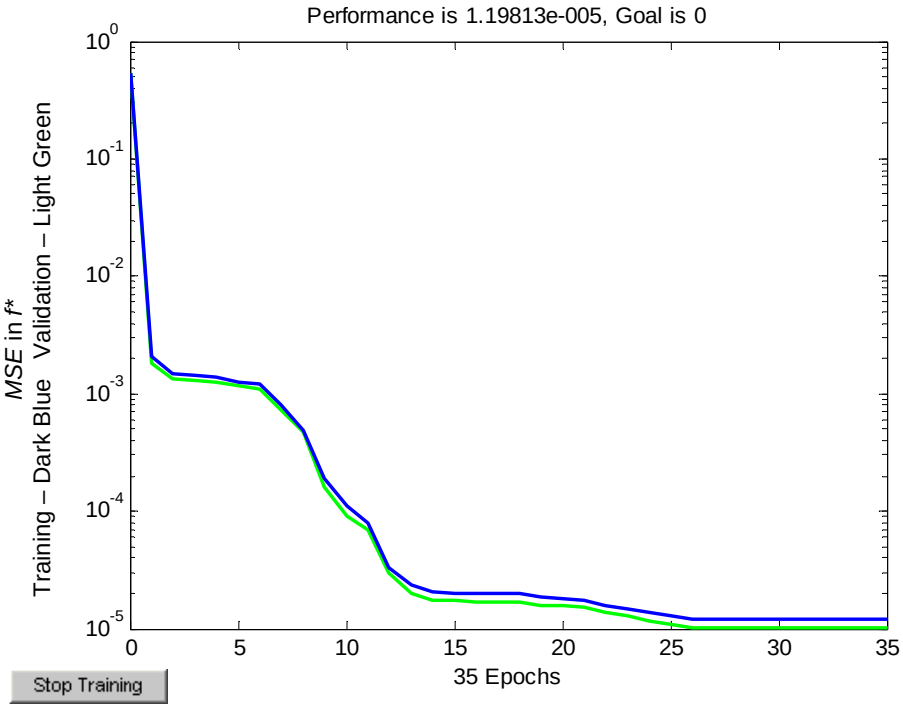

Performance curve

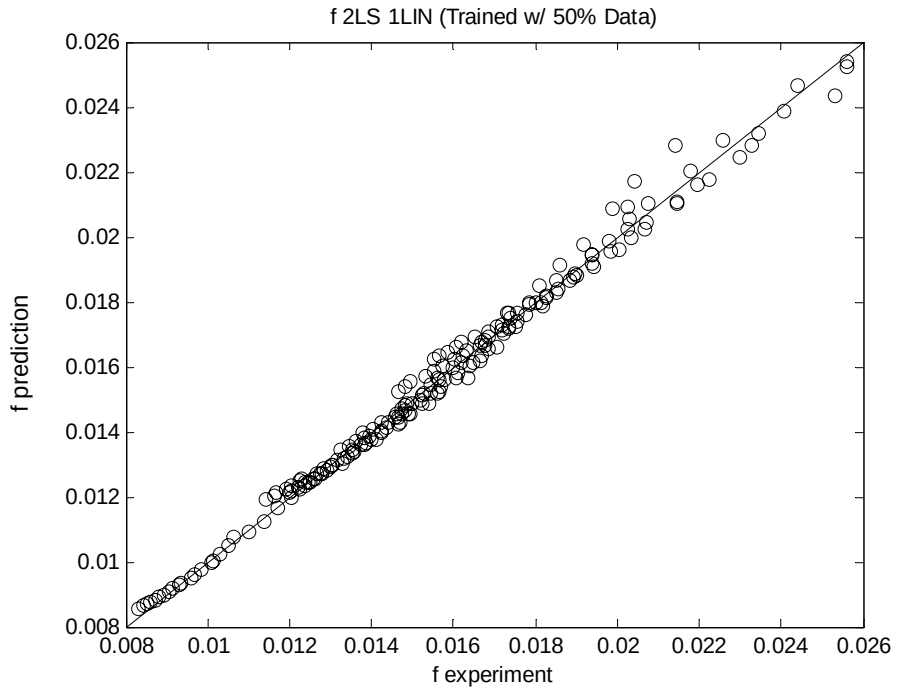

Training Set

103 data points (53.9 % of entire data set)

Validation Set

191 data points (entire data set)

Mean Squared Error

$MSE = 1.0061 \text{x} 10^{-7}$

Architecture

1st layer: 2 nodes, log-sigmoid node functions
2nd layer: 1 node, linear node function

Weight Matrices

$$W^{1,0} = \begin{bmatrix} 1.4913 & -0.2947 & -1.5270 & 3.2261 \\ 7.3003 & 6.1527 & 17.6097 & 3.2685 \end{bmatrix}$$

$$W^{2,1} = \begin{bmatrix} -0.4151 & 0.2292 \end{bmatrix}$$

Bias Vectors

$$b^1 = \begin{bmatrix} -2.6481 \\ -10.2984 \end{bmatrix} \qquad b^2 = \begin{bmatrix} 0.1525 \end{bmatrix}$$

- **f_2LS_1LS**

Training curve

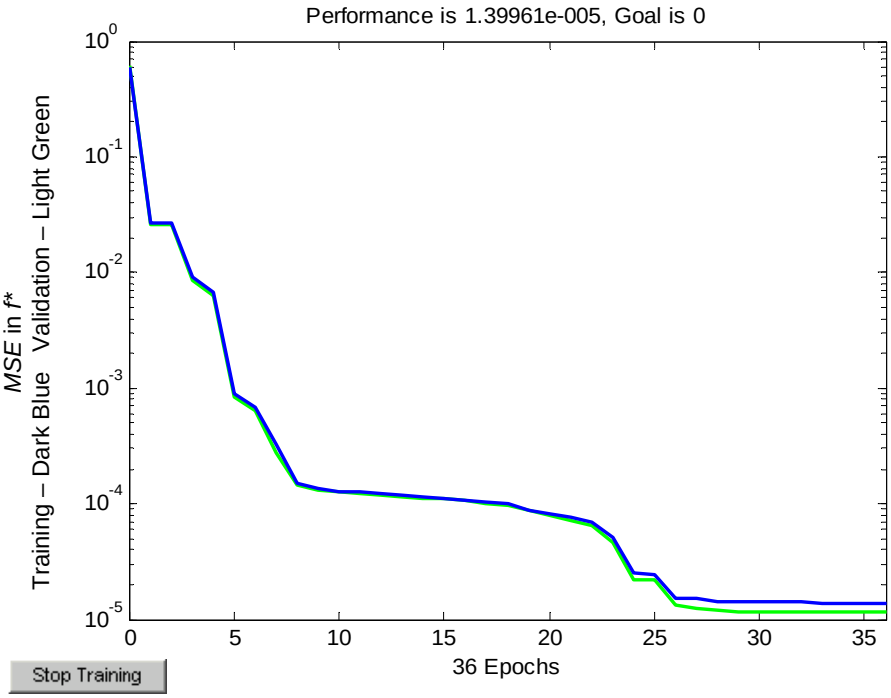

Performance curve

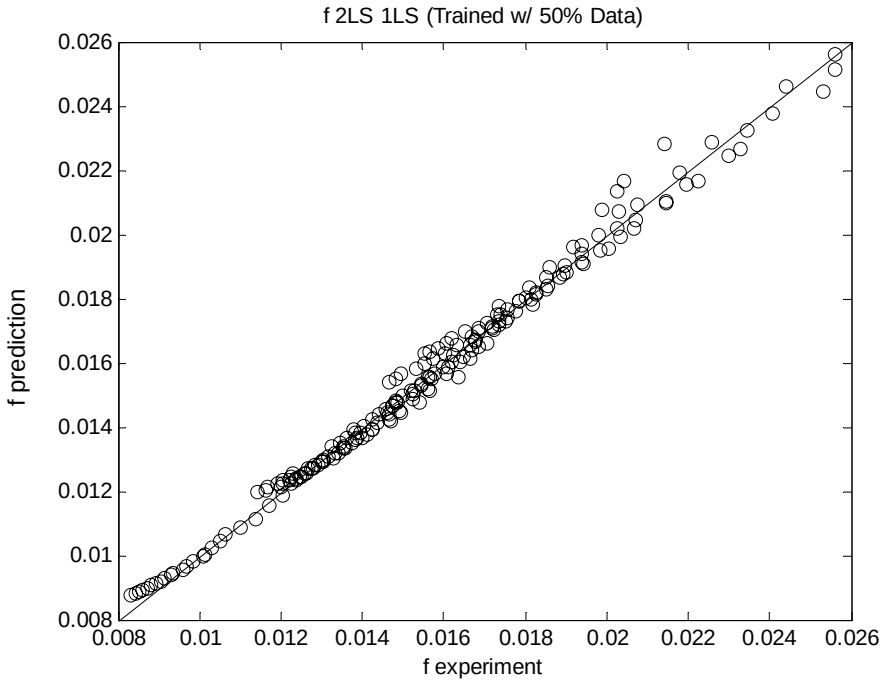

Training Set

103 data points (53.9 % of entire data set)

Validation Set

191 data points (entire data set)

Mean Squared Error

$MSE = 1.1755\text{x}10^{-7}$

Architecture

1st layer: 2 nodes, log-sigmoid node functions
2nd layer: 1 node, log-sigmoig node function

Weight Matrices

$$W^{1,0} = \begin{bmatrix} 0.8973 & -0.3481 & -1.3508 & 2.0413 \\ 10.2470 & 7.9032 & 25.4097 & 2.2485 \end{bmatrix}$$

$$W^{2,1} = \begin{bmatrix} -7.9688 & 1.2513 \end{bmatrix}$$

Bias Vectors

$$b^1 = \begin{bmatrix} -3.0794 \\ -13.0827 \end{bmatrix} \qquad b^2 = \begin{bmatrix} -1.5230 \end{bmatrix}$$

- **f_4LS_1LIN**

Training curve

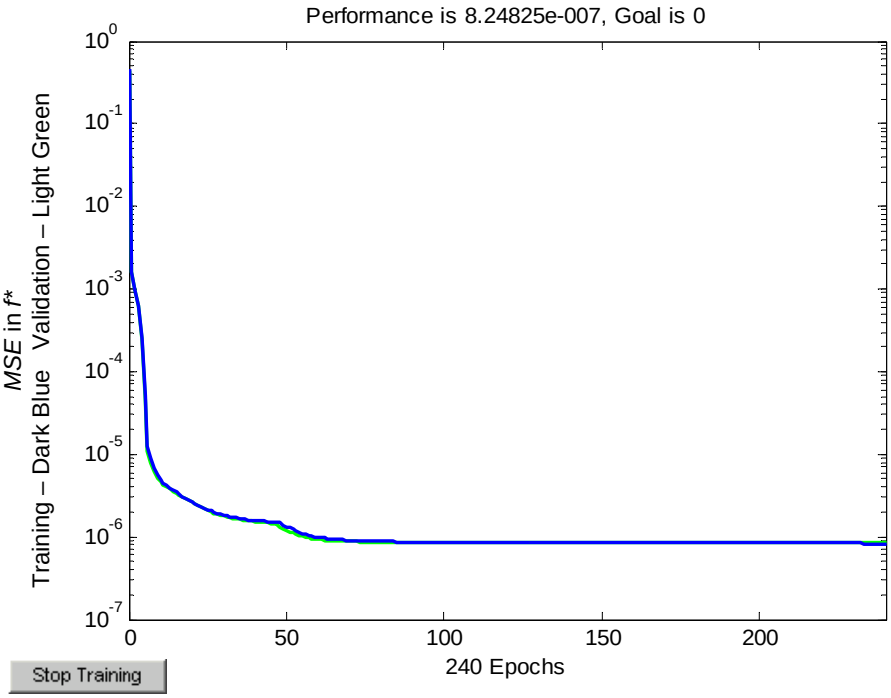

Performance curve

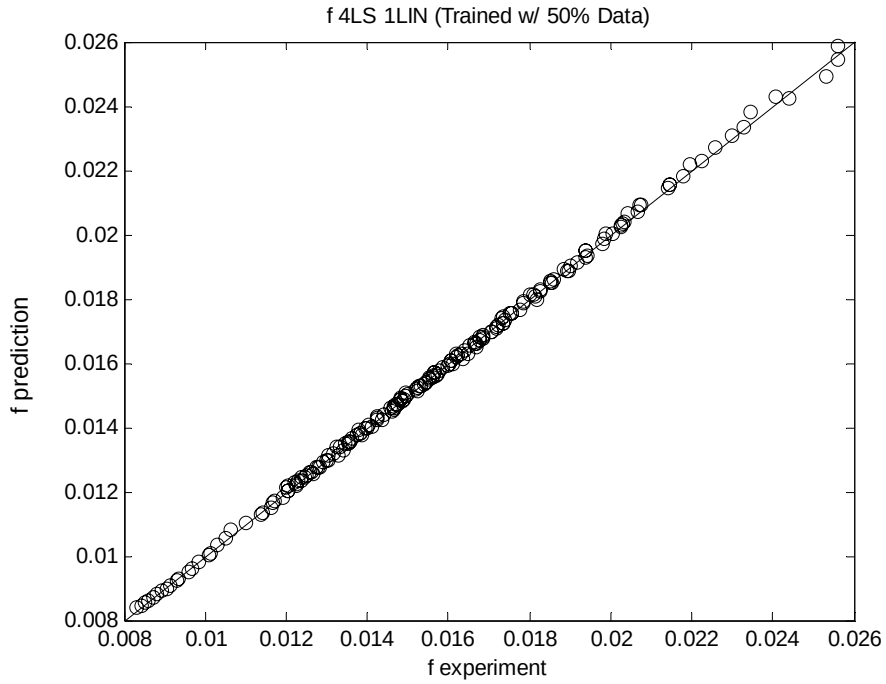

Training Set

103 data points (53.9 % of entire data set)

Validation Set

191 data points (entire data set)

Mean Squared Error

$MSE = 8.3616 \times 10^{-9}$

Architecture

1st layer: 4 nodes, log-sigmoid node functions
2nd layer: 1 node, linear node function

Weight Matrices

$$W^{1,0} = \begin{bmatrix} -32.8574 & -2.4751 & 5.9108 & 1.6128 \\ -34.8444 & -2.5732 & 7.1624 & 1.9103 \\ -6.1853 & 0.2941 & -5.4456 & -3.1627 \\ -42.7473 & -8.9839 & -30.8192 & -5.0258 \end{bmatrix}$$

$$W^{2,1} = \begin{bmatrix} -5.8421 & 5.5992 & 0.8483 & -0.1613 \end{bmatrix}$$

Bias Vectors

$$b^1 = \begin{bmatrix} 13.2446 \\ 13.6567 \\ 7.1212 \\ 26.6088 \end{bmatrix} \qquad b^2 = \begin{bmatrix} -0.2965 \end{bmatrix}$$

- **f_3LS_2LS_1LIN**

Training curve

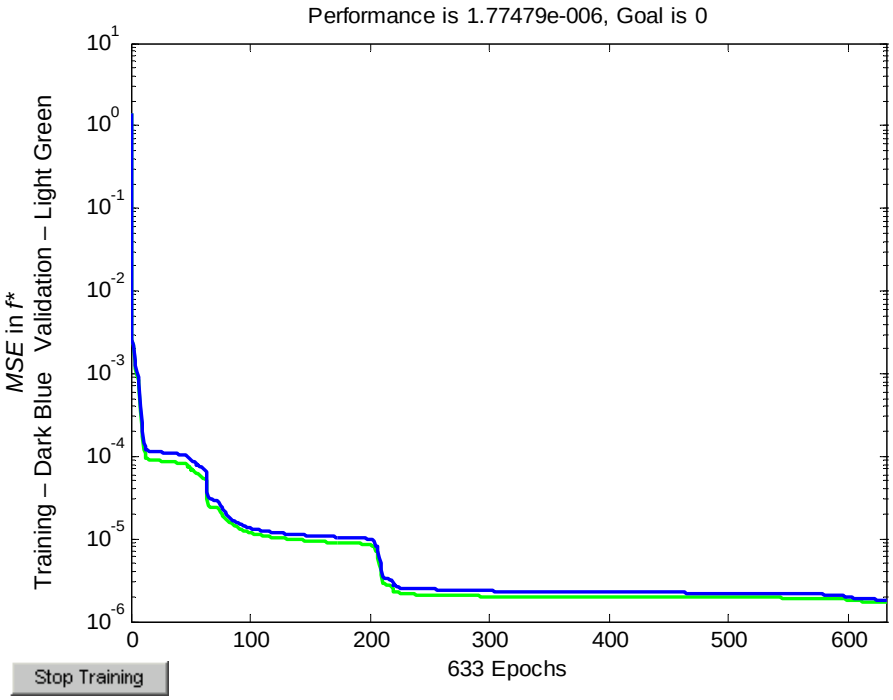

Performance curve

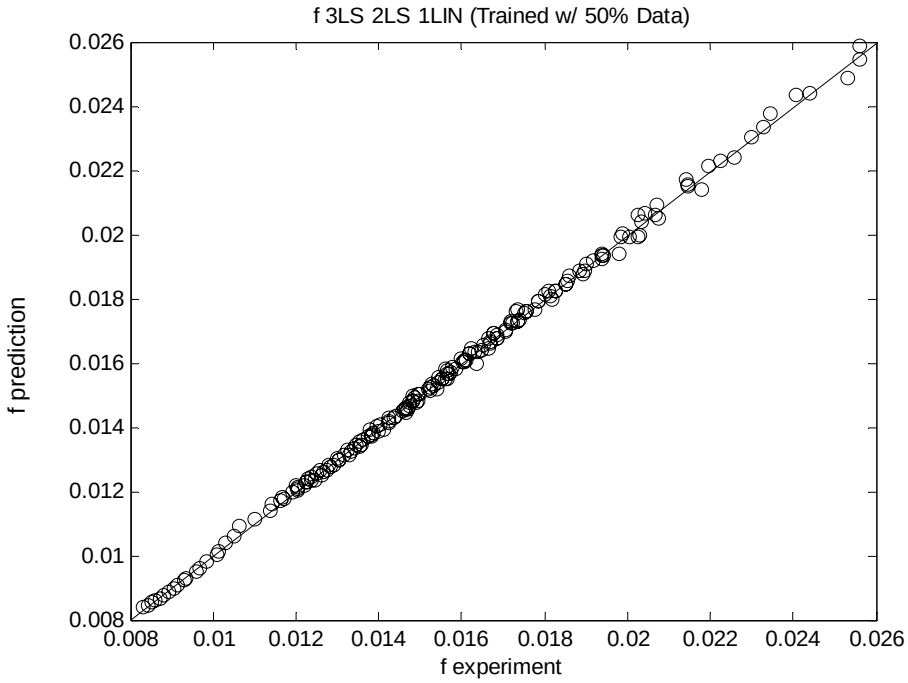

Training Set

103 data points (53.9 % of entire data set)

Validation Set

191 data points (entire data set)

Mean Squared Error

$MSE = 1.6848 \times 10^{-8}$

Architecture

1st layer: 3 nodes, log-sigmoid node functions
2nd layer: 2 nodes, log-sigmoid node functions
3rd layer: 1 node, linear node function

Weight Matrices

$$W^{1,0} = \begin{bmatrix} 5.6075 & -2.0743 & -10.3032 & 5.5460 \\ 4.8434 & -2.2012 & -36.3249 & -7.4247 \\ 23.8180 & 8.9315 & -27.1121 & -0.2415 \end{bmatrix}$$

$$W^{2,1} = \begin{bmatrix} -4.7054 & 6.4116 & 2.0242 \\ 33.2594 & 11.6171 & -19.7003 \end{bmatrix}$$

$$W^{3,2} = \begin{bmatrix} 0.1964 & -0.4994 \end{bmatrix}$$

Bias Vectors

$$b^1 = \begin{bmatrix} -4.3671 \\ 17.4521 \\ -3.7782 \end{bmatrix} \qquad b^2 = \begin{bmatrix} -7.0847 \\ 8.9007 \end{bmatrix} \qquad b^3 = \begin{bmatrix} 0.5629 \end{bmatrix}$$

- **f_4LS_3LS_1LIN**

Training curve

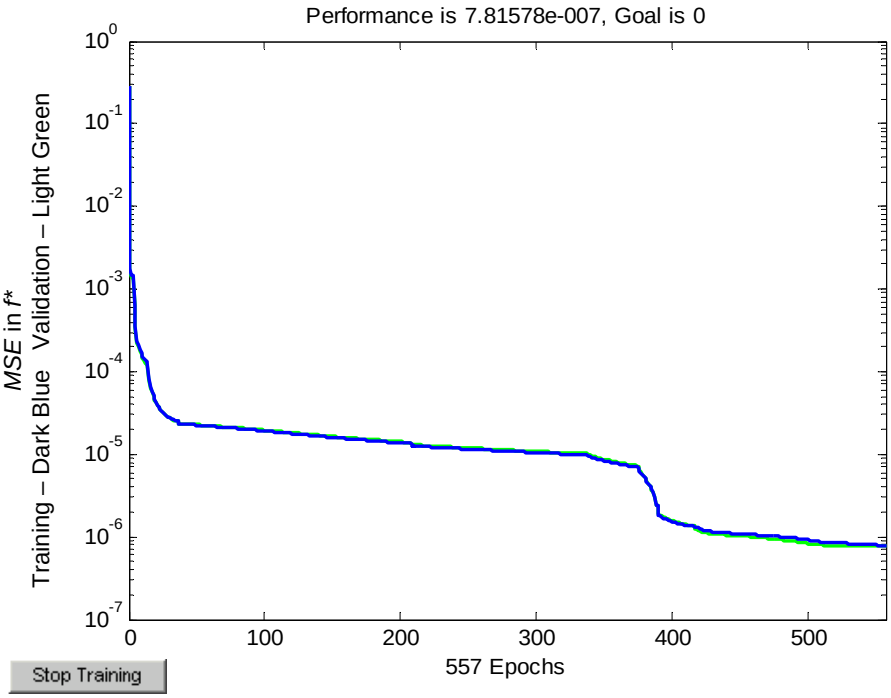

Performance curve

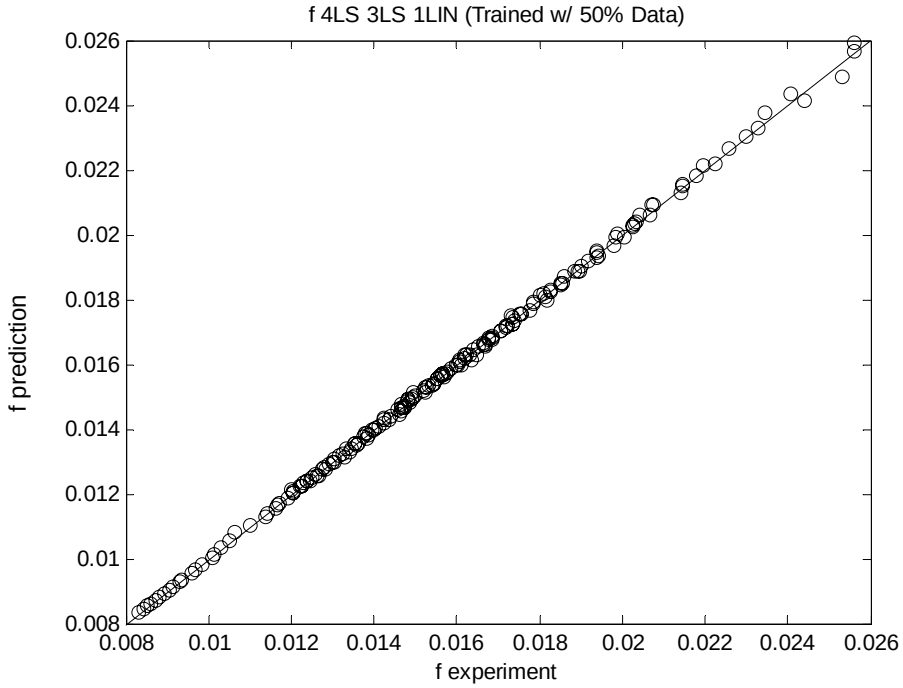

Training Set

103 data points (53.9 % of entire data set)

Validation Set

191 data points (entire data set)

Mean Squared Error

$MSE = 7.7760 \times 10^{-9}$

Architecture

1st layer: 4 nodes, log-sigmoid node functions
2nd layer: 3 nodes, log-sigmoid node functions
3rd layer: 1 node, linear node function

Weight Matrices

$$W^{1,0} = \begin{bmatrix} 0.3268 & -14.5815 & 39.1829 & 2.5444 \\ 3.0687 & 30.8963 & 19.5763 & -1.1098 \\ -4.3748 & 3.0079 & 0.4148 & 1.9940 \\ -14.9266 & -16.6241 & 31.6417 & 1.3000 \end{bmatrix}$$

$$W^{2,1} = \begin{bmatrix} 0.5734 & 4.4838 & -4.4526 & 2.6621 \\ 1.7147 & 3.7863 & -7.9068 & -2.2088 \\ -4.6517 & 12.3448 & 6.0003 & -3.5944 \end{bmatrix}$$

$$W^{3,2} = \begin{bmatrix} 7.9818 & -3.7096 & -4.9051 \end{bmatrix}$$

Bias Vectors

$$b^1 = \begin{bmatrix} -1.1447 \\ -16.9410 \\ -3.6307 \\ -16.1583 \end{bmatrix} \qquad b^2 = \begin{bmatrix} -2.5850 \\ -2.1324 \\ -3.8526 \end{bmatrix} \qquad b^3 = \begin{bmatrix} 1.4356 \end{bmatrix}$$

A2. *j*-Factor Networks Trained with Half of Data Points

- **j_2LS_1LIN**

Training curve

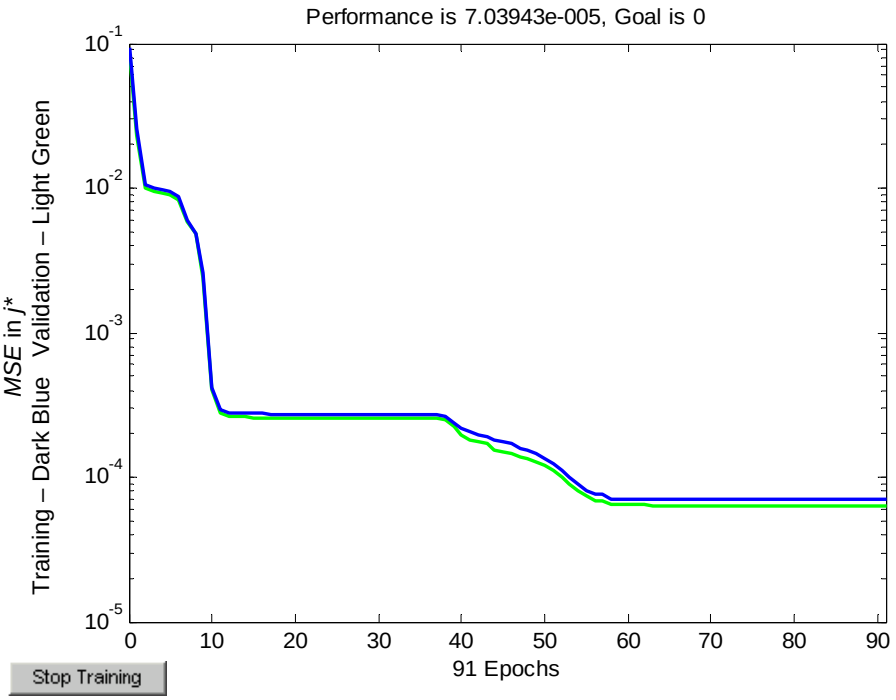

Performance curve

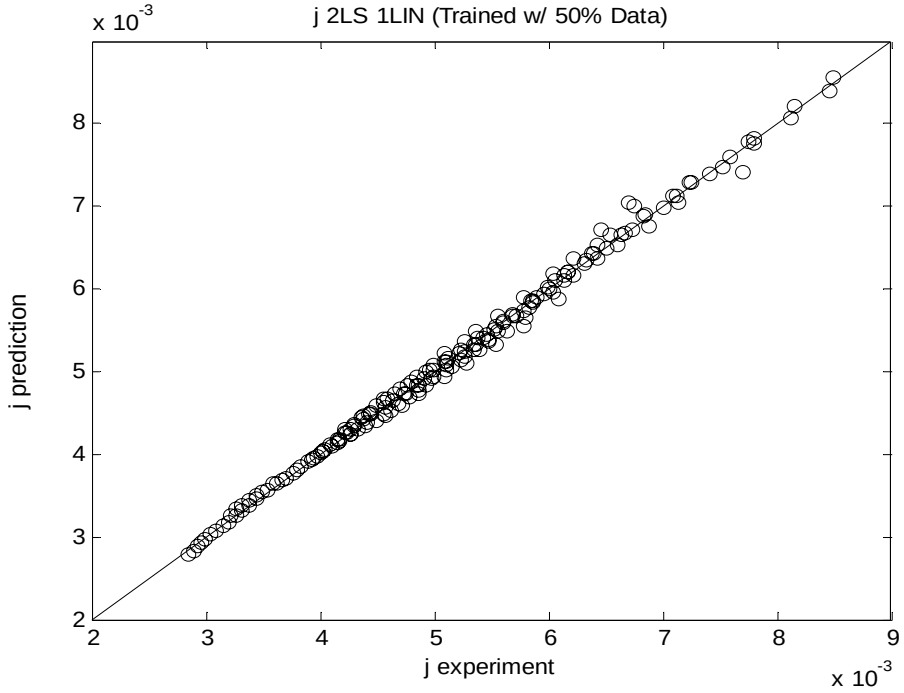

Training Set

96 data points (52.5 % of entire data set)

Validation Set

183 data points (entire data set)

Mean Squared Error

$MSE = 6.3833 \text{x} 10^{-9}$

Architecture

1st layer: 2 nodes, log-sigmoid node functions
2nd layer: 1 node, linear node function

Weight Matrices

$$W^{1,0} = \begin{bmatrix} 0.4207 & 0.4510 & 3.0941 & 8.8906 \\ 3.9855 & 2.2982 & 4.1999 & -3.4249 \end{bmatrix}$$

$$W^{2,1} = \begin{bmatrix} -1.4448 & 0.8170 \end{bmatrix}$$

Bias Vectors

$$b^1 = \begin{bmatrix} -11.3178 \\ -2.0000 \end{bmatrix} \qquad b^2 = \begin{bmatrix} 0.3324 \end{bmatrix}$$

- **j_2LS_1LS**

Training curve

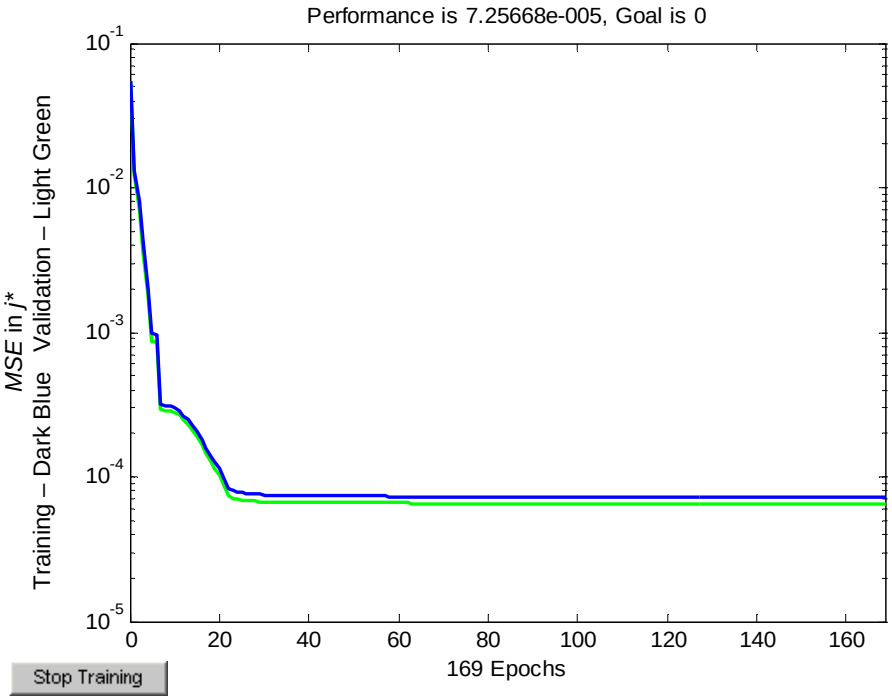

Performance curve

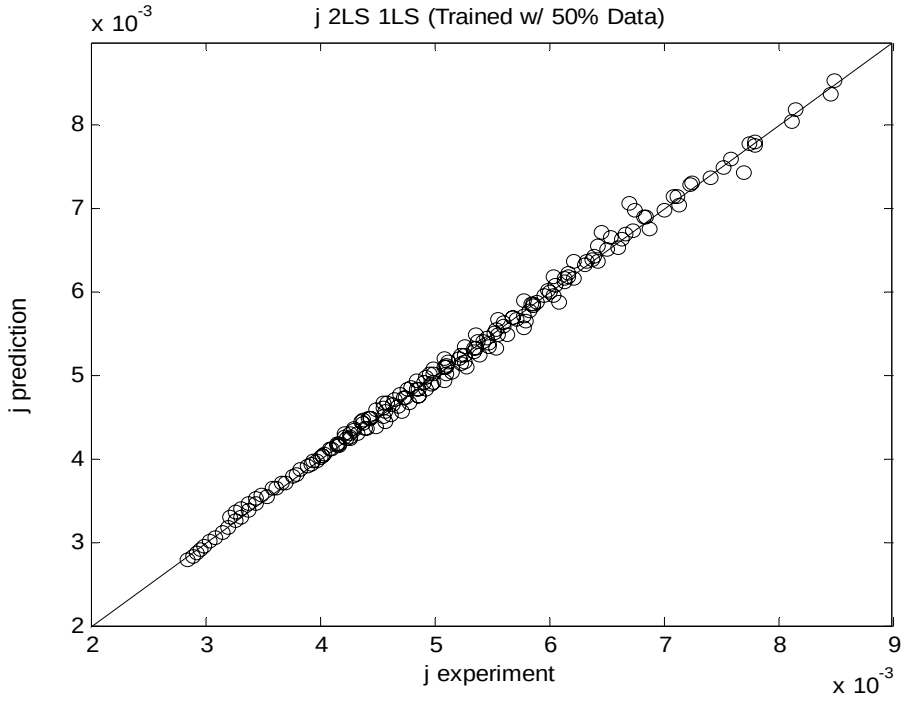

Training Set

96 data points (52.5 % of entire data set)

Validation Set

183 data points (entire data set)

Mean Squared Error

$MSE = 6.5631\text{x}10^{-9}$

Architecture

1st layer: 2 nodes, log-sigmoid node functions
2nd layer: 1 node, log-sigmoid node function

Weight Matrices

$$W^{1,0} = \begin{bmatrix} -0.0584 & -0.2588 & -4.3719 & -14.0916 \\ -2.2563 & -1.2836 & -2.2815 & 2.2179 \end{bmatrix}$$

$$W^{2,1} = \begin{bmatrix} 1.2662 & -22.2090 \end{bmatrix}$$

Bias Vectors

$$b^1 = \begin{bmatrix} 14.3584 \\ -3.2414 \end{bmatrix} \qquad b^2 = \begin{bmatrix} 19.9363 \end{bmatrix}$$

- **j_4LS_1LIN**

Training curve

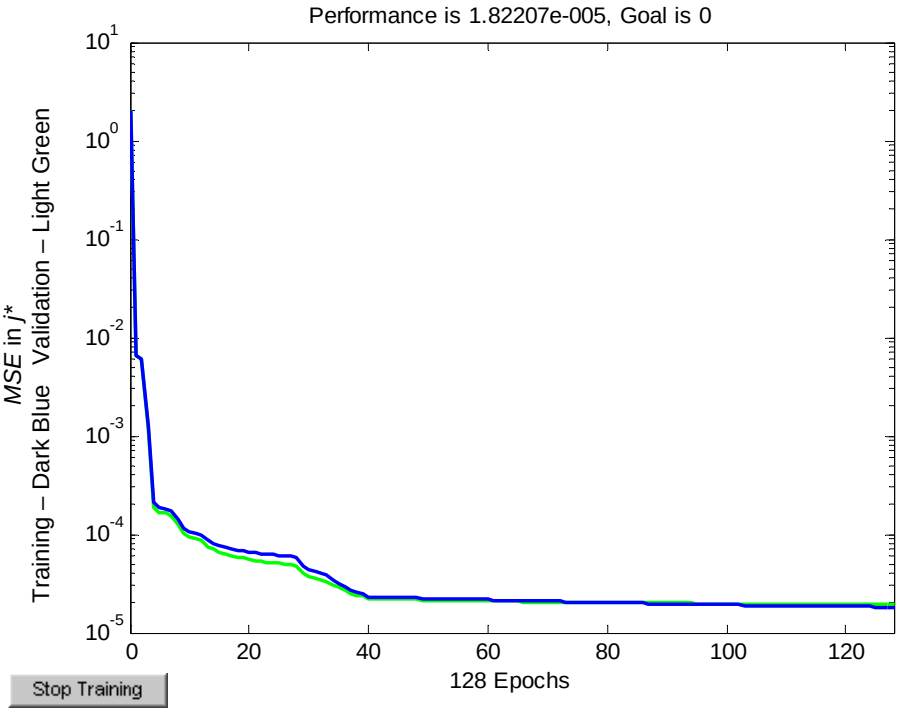

Performance curve

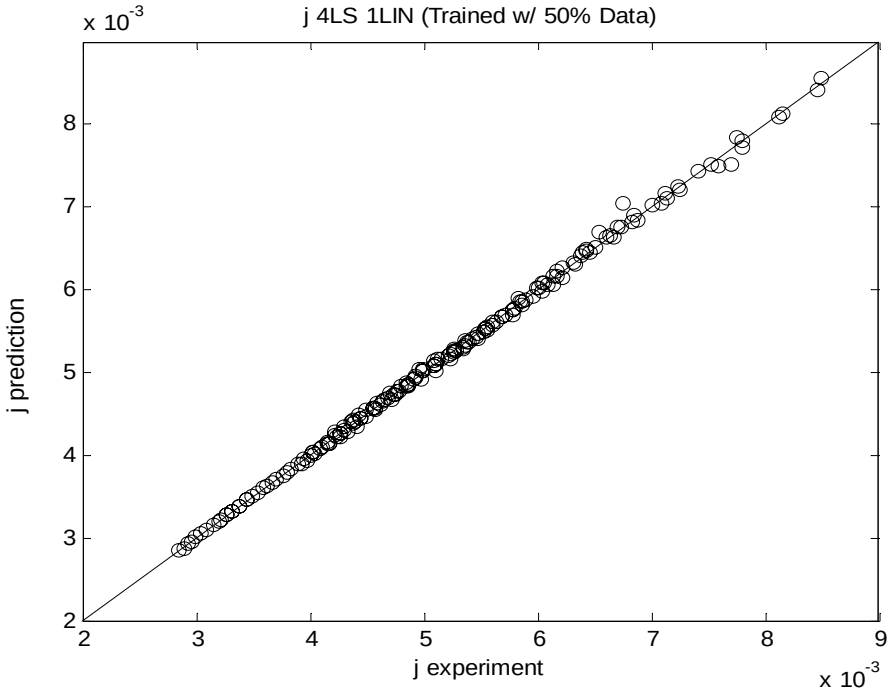

Training Set

96 data points (52.5 % of entire data set)

Validation Set

183 data points (entire data set)

Mean Squared Error

$MSE = 1.9653 \times 10^{-9}$

Architecture

1st layer: 4 nodes, log-sigmoid node functions
2nd layer: 1 node, linear node function

Weight Matrices

$$W^{1,0} = \begin{bmatrix} -2.1481 & -1.2490 & -1.5292 & 0.7638 \\ 3.8512 & 0.6101 & 8.1524 & 11.8902 \\ 16.8777 & -0.2062 & 8.2827 & 9.5099 \\ -17.7782 & 30.5651 & -24.3131 & 7.1959 \end{bmatrix}$$

$$W^{2,1} = \begin{bmatrix} -3.7124 & -0.4287 & -0.1577 & -0.0828 \end{bmatrix}$$

Bias Vectors

$$b^1 = \begin{bmatrix} 2.9582 \\ -15.2708 \\ -13.8116 \\ -10.6127 \end{bmatrix} \qquad b^2 = \begin{bmatrix} 3.8442 \end{bmatrix}$$

- **j_3LS_2LS_1LIN**

Training curve

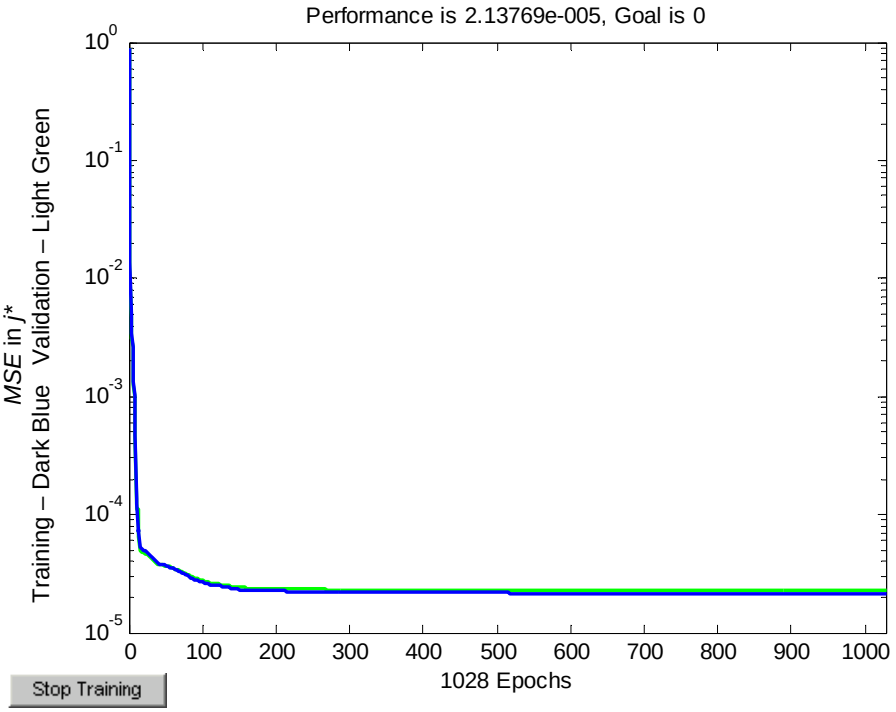

Performance curve

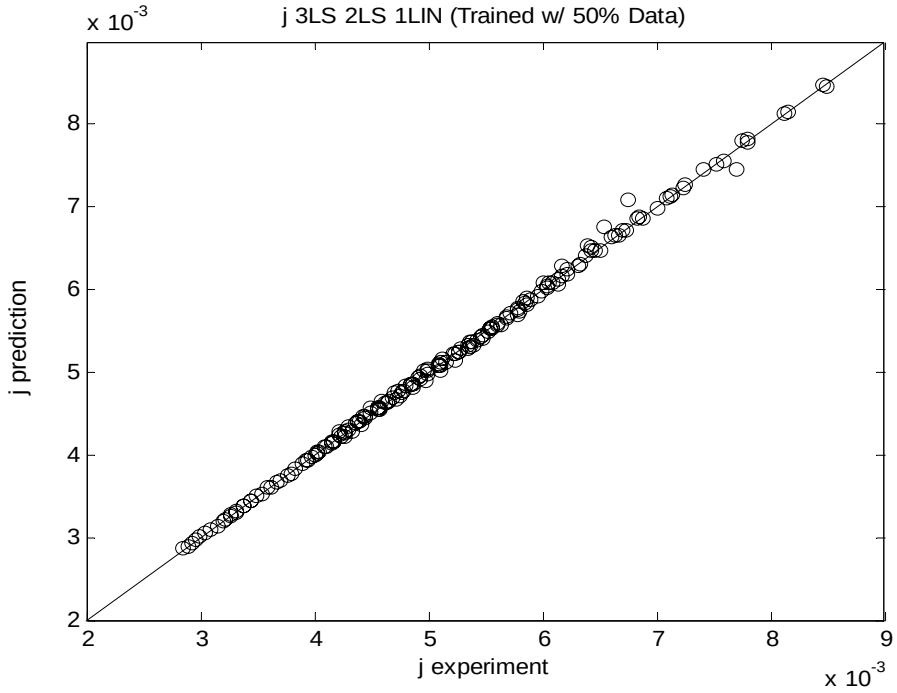

Training Set

96 data points (52.5 % of entire data set)

Validation Set

183 data points (entire data set)

Mean Squared Error

$MSE = 2.2488 \times 10^{-9}$

Architecture

1st layer: 3 nodes, log-sigmoid node functions
2nd layer: 2 nodes, log-sigmoid node functions
3rd layer: 1 node, linear node function

Weight Matrices

$$W^{1,0} = \begin{bmatrix} -0.9034 & -0.6046 & -0.6516 & -0.9446 \\ 22.7059 & 15.9023 & 11.6221 & -1.1728 \\ -22.1450 & -0.2982 & 82.3783 & -1.3694 \end{bmatrix}$$

$$W^{2,1} = \begin{bmatrix} 37.9980 & 0.5193 & -16.3731 \\ 18.4855 & -63.6930 & -40.4826 \end{bmatrix}$$

$$W^{3,2} = \begin{bmatrix} 54.4963 & -22.0067 \end{bmatrix}$$

Bias Vectors

$$b^1 = \begin{bmatrix} 4.4739 \\ -16.9441 \\ -20.5881 \end{bmatrix} \qquad b^2 = \begin{bmatrix} -31.9131 \\ 50.4233 \end{bmatrix} \qquad b^3 = \begin{bmatrix} -31.4323 \end{bmatrix}$$

- **j_4LS_3LS_1LIN**

Training curve

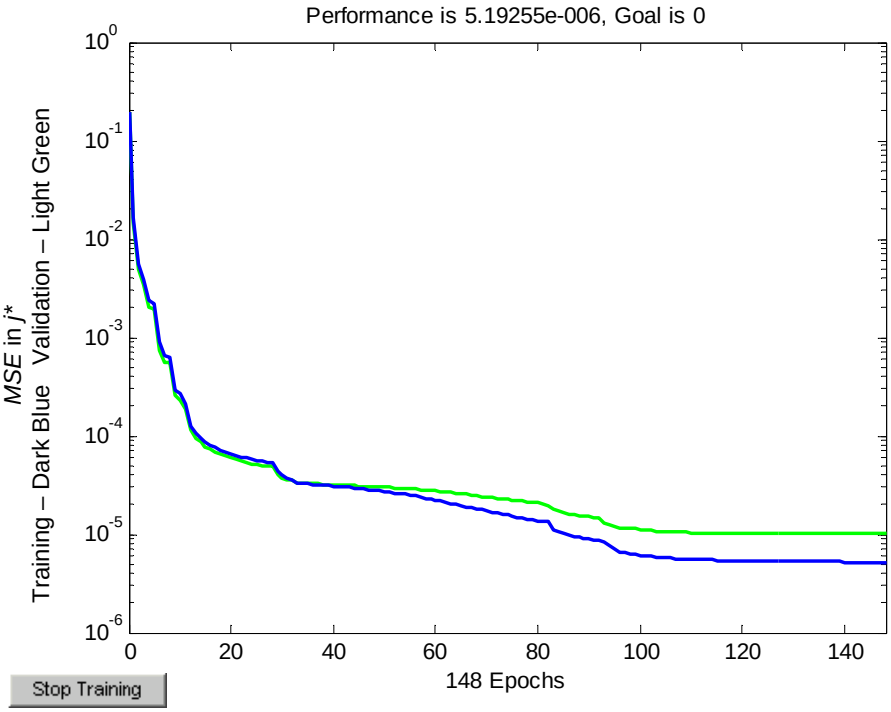

Performance curve

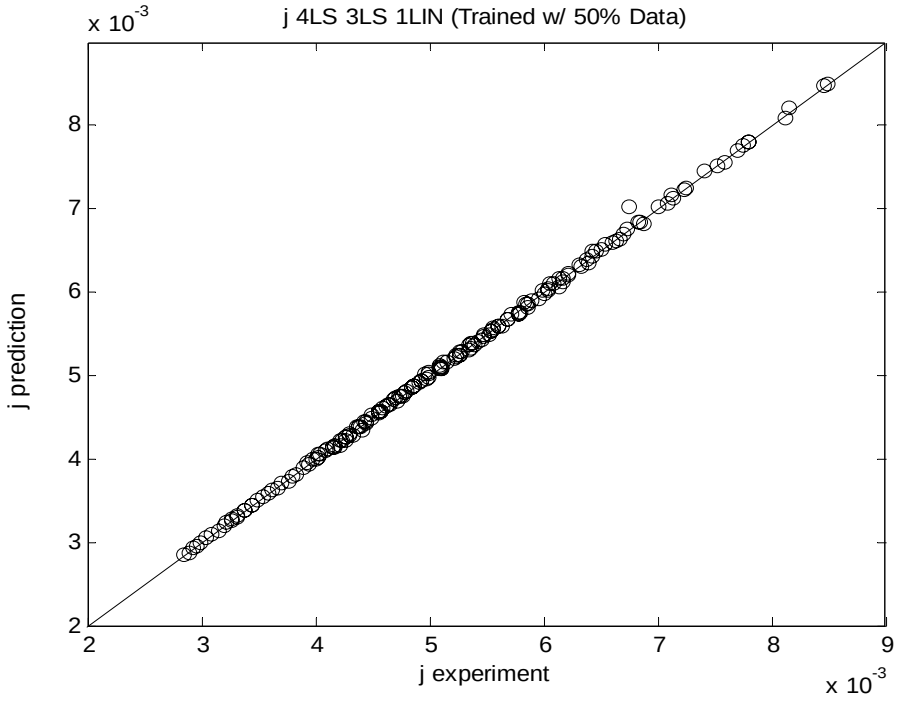

Training Set

96 data points (52.5 % of entire data set)

Validation Set

183 data points (entire data set)

Mean Squared Error

$MSE = 1.0062 \times 10^{-9}$

Architecture

1st layer: 4 nodes, log-sigmoid node functions
2nd layer: 3 nodes, log-sigmoid node functions
3rd layer: 1 node, linear node function

Weight Matrices

$$W^{1,0} = \begin{bmatrix} 19.0167 & 8.9751 & 25.6407 & 14.3683 \\ -11.3185 & 20.9943 & -4.2650 & 5.9369 \\ 2.9668 & 5.2661 & 23.4843 & -11.5113 \\ 0.4415 & -25.8971 & 31.0997 & -2.1375 \end{bmatrix}$$

$$W^{2,1} = \begin{bmatrix} 8.2539 & -3.1088 & 8.5495 & -0.1561 \\ 0.1754 & -7.2184 & -2.1861 & -9.2542 \\ 0.2503 & 1.9816 & 0.2221 & 2.5477 \end{bmatrix}$$

$$W^{3,2} = \begin{bmatrix} 0.2857 & -1.6033 & -3.6997 \end{bmatrix}$$

Bias Vectors

$$b^1 = \begin{bmatrix} -29.1609 \\ -12.1566 \\ -1.8474 \\ -5.8078 \end{bmatrix} \qquad b^2 = \begin{bmatrix} -6.0923 \\ 5.8834 \\ -1.4754 \end{bmatrix} \qquad b^3 = \begin{bmatrix} 3.0794 \end{bmatrix}$$

A3. f_4LS_1LIN Networks Trained with Selected Tube Data

- **f_4LS_1LIN (Trained with Tubes 1 and 5)**

Training curve

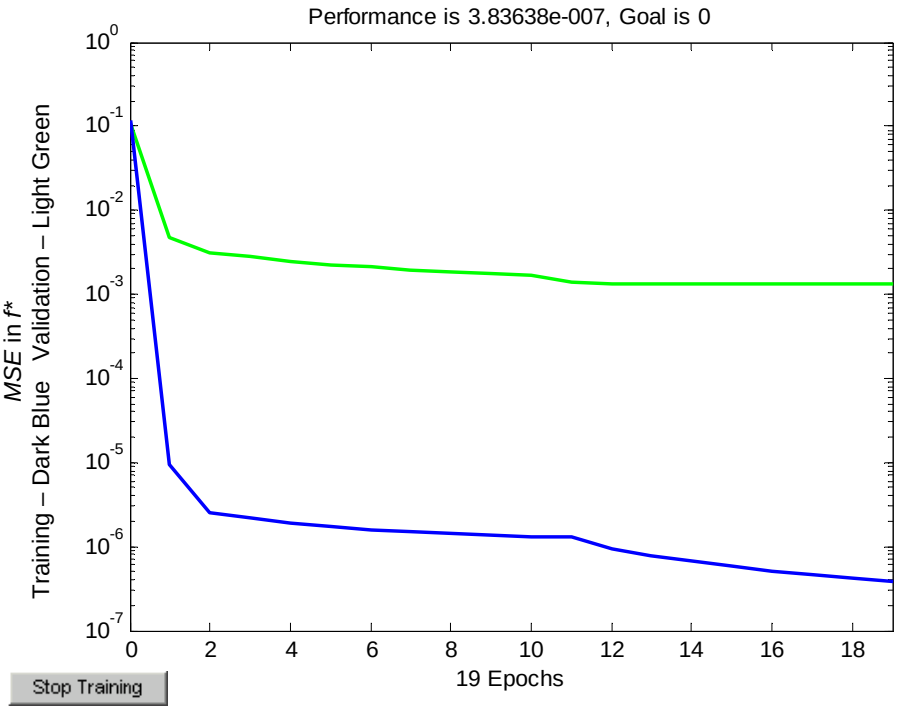

Performance curve

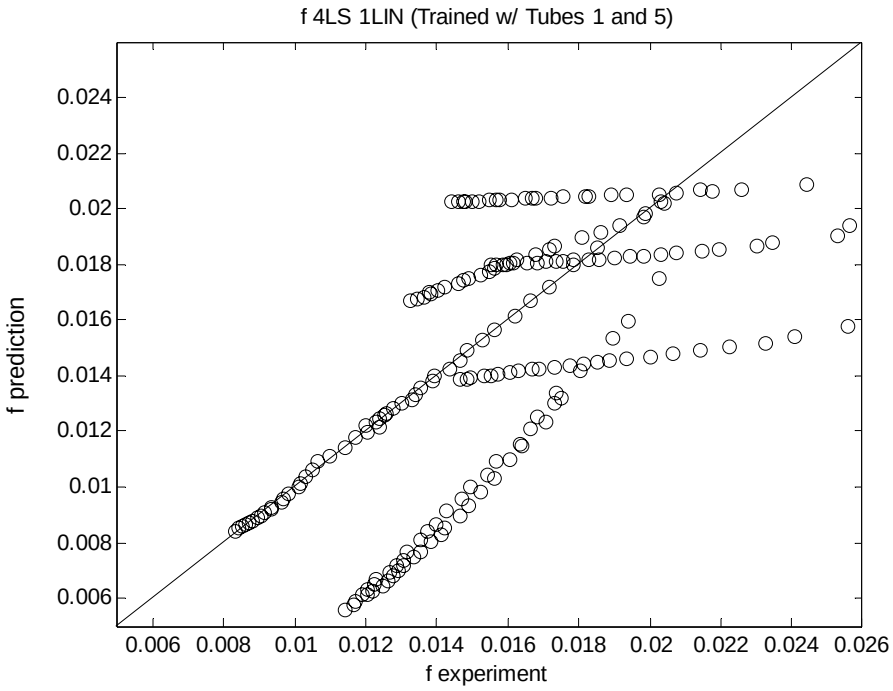

Training Set

Data from tubes 1 and 5. 48 data points (25.1 % of entire data set)

Validation Set

191 data points (entire data set)

Mean Squared Error

$MSE = 1.321\text{x}10^{-5}$

Architecture

1st layer: 4 nodes, log-sigmoid node functions
2nd layer: 1 node, linear node function

Weight Matrices

$$W^{1,0} = \begin{bmatrix} -10.6233 & 14.2637 & 36.3383 & -6.9768 \\ 17.6568 & 9.5378 & -30.1848 & -1.176 \\ -8.0379 & -13.9437 & -19.2802 & -15.7391 \\ -7.4223 & -16.0299 & -13.2603 & 15.0961 \end{bmatrix}$$

$$W^{2,1} = \begin{bmatrix} 0.15338 & 0.10457 & 0.02006 & -0.025383 \end{bmatrix}$$

Bias Vectors

$$b^1 = \begin{bmatrix} -4.5968 \\ -2.963 \\ 25.3965 \\ -6.8371 \end{bmatrix} \qquad b^2 = \begin{bmatrix} -0.049918 \end{bmatrix}$$

- **f_4LS_1LIN (Trained with Tubes 1, 3, and 5)**

Training curve

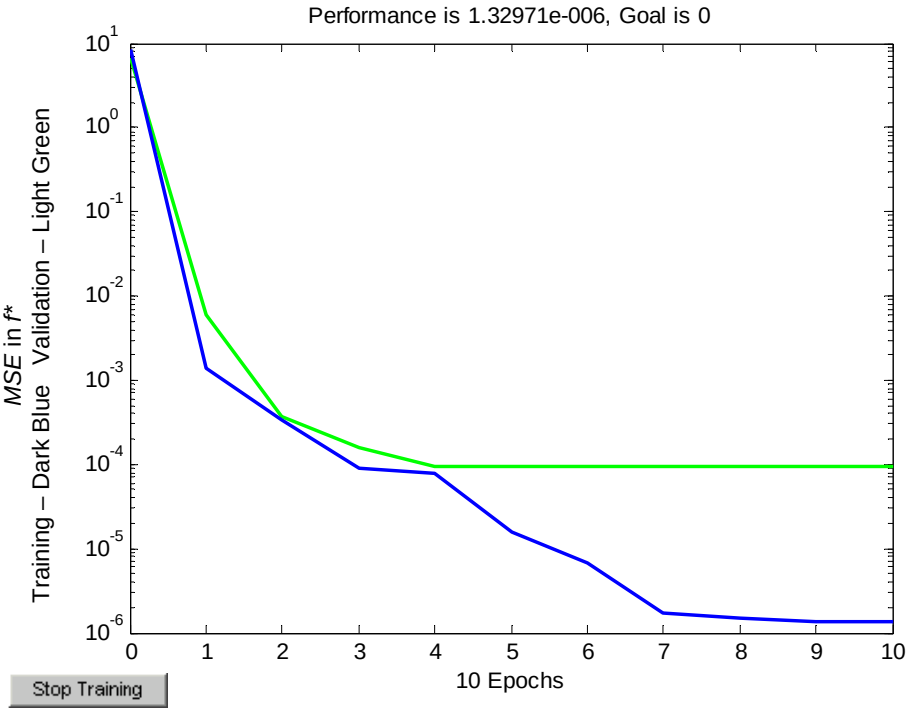

Performance curve

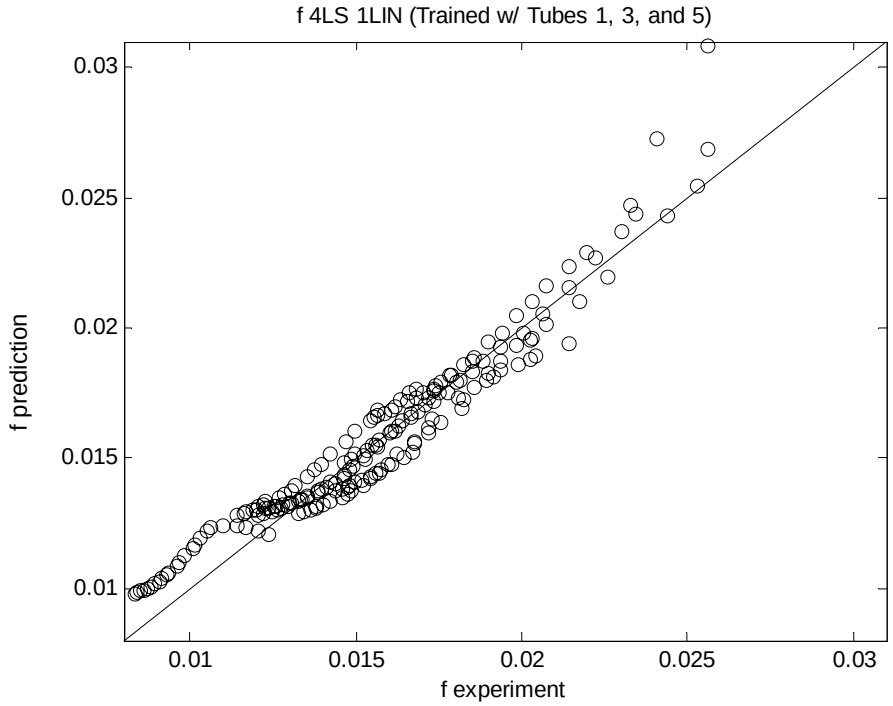

Training Set

Data from tubes 1, 3, and 5. 72 data points (37.7 % of entire data set)

Validation Set

191 data points (entire data set)

Mean Squared Error

$MSE = 9.290\text{x}10^{-7}$

Architecture

1st layer: 4 nodes, log-sigmoid node functions
2nd layer: 1 node, linear node function

Weight Matrices

$$W^{1,0} = \begin{bmatrix} -6.2684 & -7.7509 & -41.3106 & 14.5755 \\ -18.5453 & 5.4435 & -31.1845 & -5.9903 \\ 1.9517 & 0.12348 & -18.8066 & 20.8802 \\ 10.1458 & -13.4434 & 42.4279 & 2.9836 \end{bmatrix}$$

$$W^{2,1} = \begin{bmatrix} -0.20236 & -0.090462 & -0.063562 & -0.80884 \end{bmatrix}$$

Bias Vectors

$$b^1 = \begin{bmatrix} 12.1544 \\ 12.1983 \\ -12.6822 \\ -3.1777 \end{bmatrix} \qquad b^2 = \begin{bmatrix} 1.196 \end{bmatrix}$$

- **f_4LS_1LIN (Trained with Tubes 1, 3, 5, and 7)**

Training curve

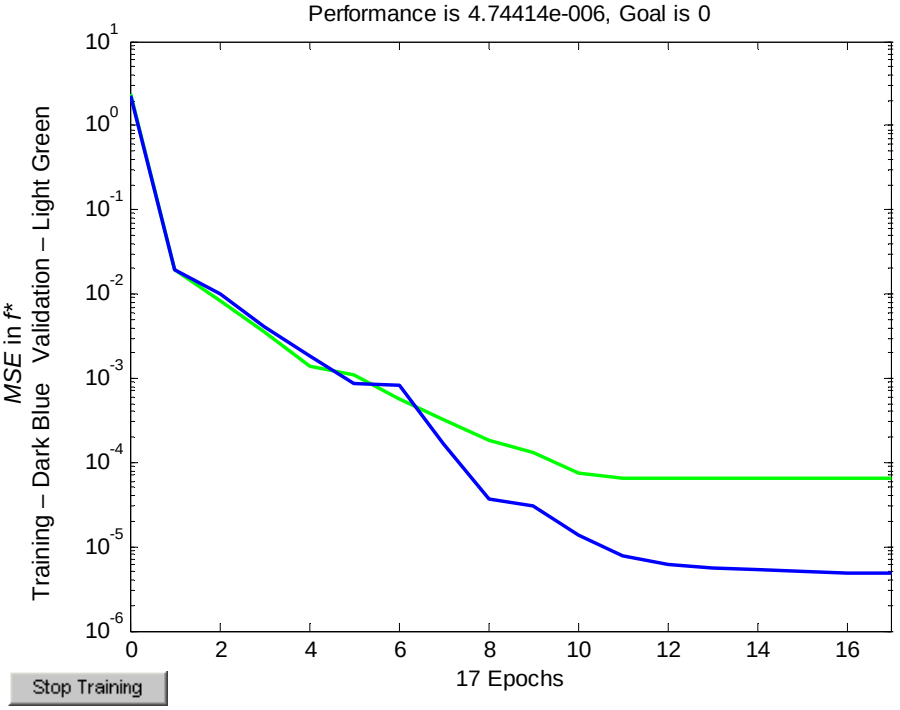

Performance curve

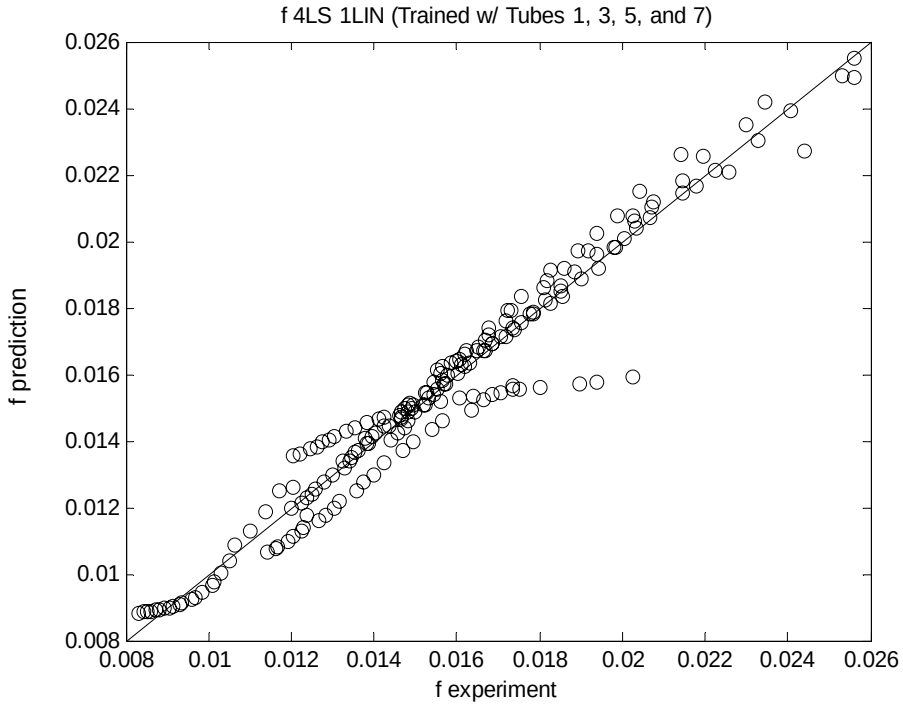

Training Set

Data from tubes 1, 3, 5, and 7. 95 data points (49.7 % of entire data set)

Validation Set

191 data points (entire data set)

Mean Squared Error

$MSE = 6.348\text{x}10^{-7}$

Architecture

1st layer: 4 nodes, log-sigmoid node functions
2nd layer: 1 node, linear node function

Weight Matrices

$$W^{1,0} = \begin{bmatrix} -6.5058 & -19.7273 & 31.5896 & -1.8206 \\ -2.7053 & -25.6833 & -8.58 & 7.7529 \\ -11.8958 & 4.3339 & 2.5764 & 17.3044 \\ 19.0618 & 9.78 & -6.6952 & 12.4852 \end{bmatrix}$$

$$W^{2,1} = \begin{bmatrix} 0.3001 & -0.12647 & -0.06925 & 0.46538 \end{bmatrix}$$

Bias Vectors

$$b^1 = \begin{bmatrix} 12.4092 \\ 13.336 \\ -13.2892 \\ -8.7611 \end{bmatrix} \qquad b^2 = \begin{bmatrix} -0.48347 \end{bmatrix}$$

- **f_4LS_1LIN (Trained with Tubes 1, 3, 4, 5, and 7)**

Training curve

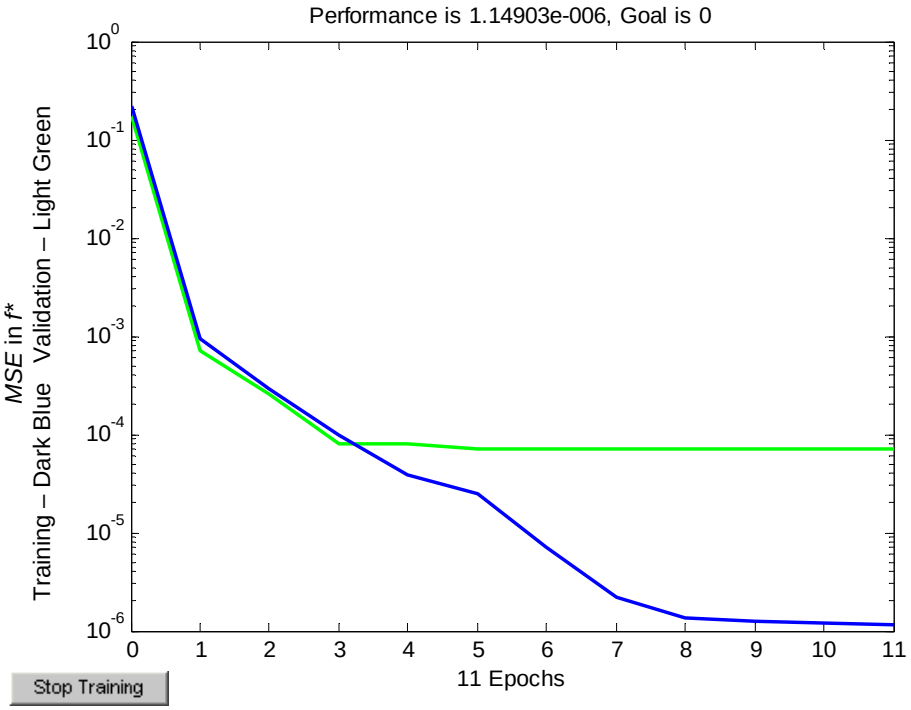

Performance curve

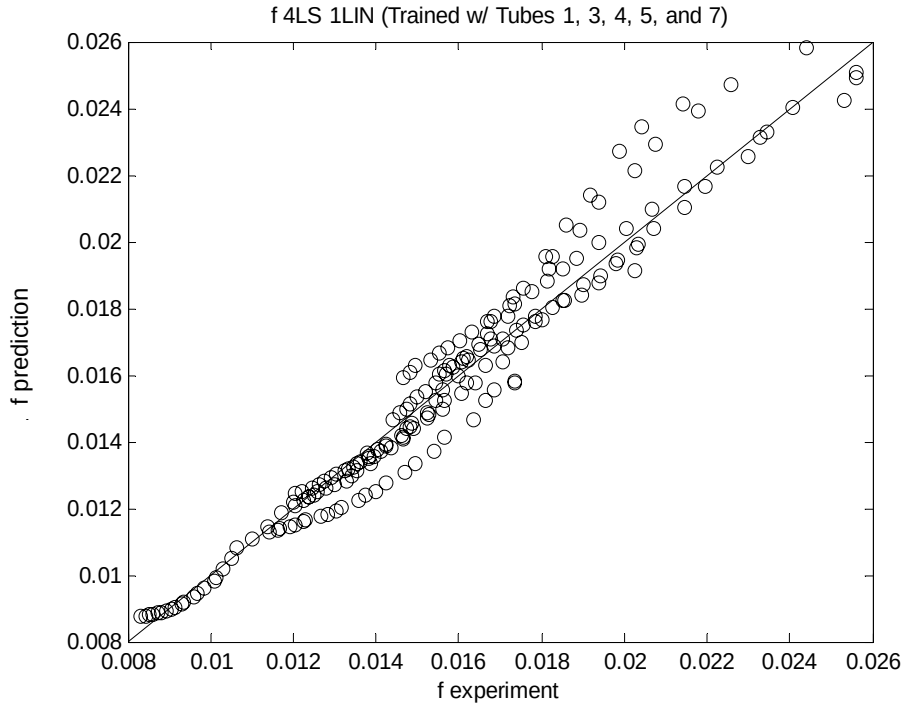

Training Set

Data from tubes 1, 3, 4, 5 and 7. 119 data points (62.3 % of entire data set)

Validation Set

191 data points (entire data set)

Mean Squared Error

$MSE = 7.060\text{x}10^{-7}$

Architecture

1st layer: 4 nodes, log-sigmoid node functions
2nd layer: 1 node, linear node function

Weight Matrices

$$W^{1,0} = \begin{bmatrix} 9.9203 & -3.3424 & 47.6919 & 10.9871 \\ -0.78788 & 1.1413 & -32.0074 & 9.9395 \\ -7.6648 & 10.9958 & -22.2547 & -14.4109 \\ -6.7485 & -9.8856 & -13.7901 & -7.8034 \end{bmatrix}$$

$$W^{2,1} = \begin{bmatrix} -0.066006 & -0.12096 & 0.053824 & -0.16007 \end{bmatrix}$$

Bias Vectors

$$b^1 = \begin{bmatrix} -27.2561 \\ 0.12498 \\ 13.0717 \\ 14.3825 \end{bmatrix} \qquad b^2 = \begin{bmatrix} 0.22725 \end{bmatrix}$$

- **f_4LS_1LIN (Trained with Tubes 1, 3, 4, 5, 7, and 8)**

Training curve

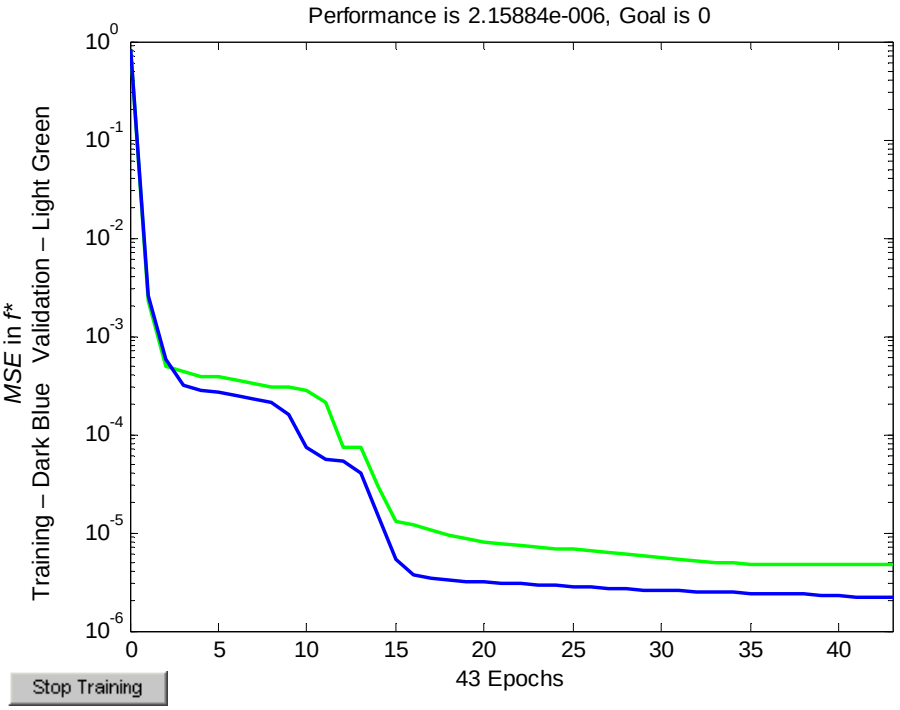

Performance curve

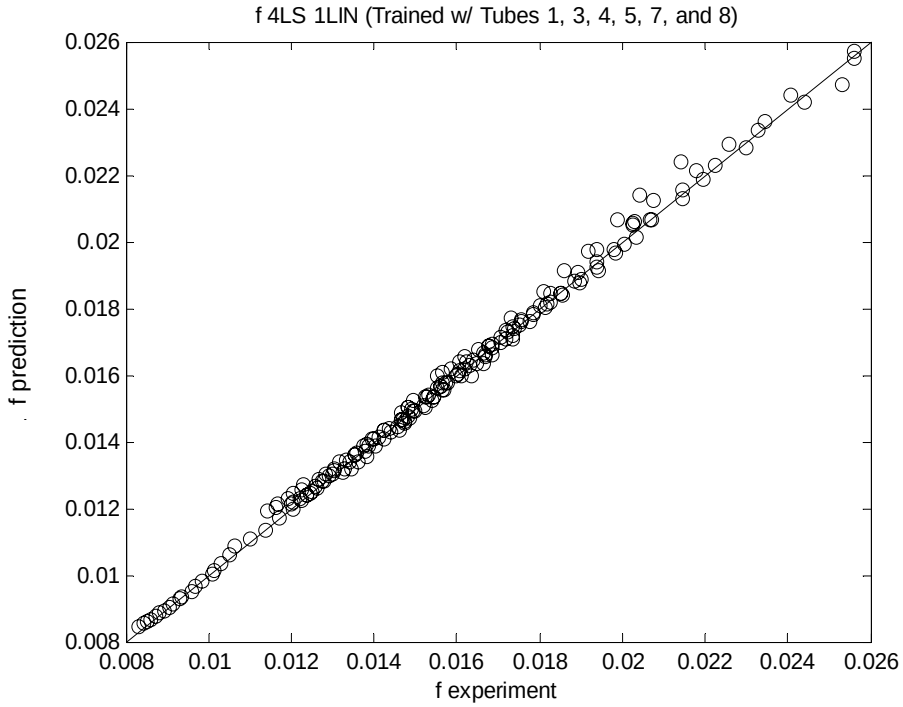

Training Set

Data from tubes 1, 3, 4, 5, 7, and 8. 143 data points (74.9 % of entire data set)

Validation Set

191 data points (entire data set)

Mean Squared Error

$MSE = 4.7125\text{x}10^{-8}$

Architecture

1st layer: 4 nodes, log-sigmoid node functions
2nd layer: 1 node, linear node function

Weight Matrices

$$W^{1,0} = \begin{bmatrix} -12.3243 & 21.0286 & -27.0291 & 10.3632 \\ 0.62089 & -0.38821 & -0.97513 & 2.0593 \\ 9.4293 & 14.9492 & -18.5655 & 4.7969 \\ -4.9159 & 8.3204 & 30.8513 & 14.5582 \end{bmatrix}$$

$$W^{2,1} = \begin{bmatrix} -0.021166 & -0.73519 & 0.15295 & -0.032048 \end{bmatrix}$$

Bias Vectors

$$b^1 = \begin{bmatrix} -5.4117 \\ -1.9455 \\ -6.9407 \\ -19.107 \end{bmatrix} \qquad b^2 = \begin{bmatrix} 0.27958 \end{bmatrix}$$

A4. j_4LS_1LIN Networks Trained with Selected Tube Data

- **j_4LS_1LIN (Trained with Tubes 1 and 5)**

Training curve

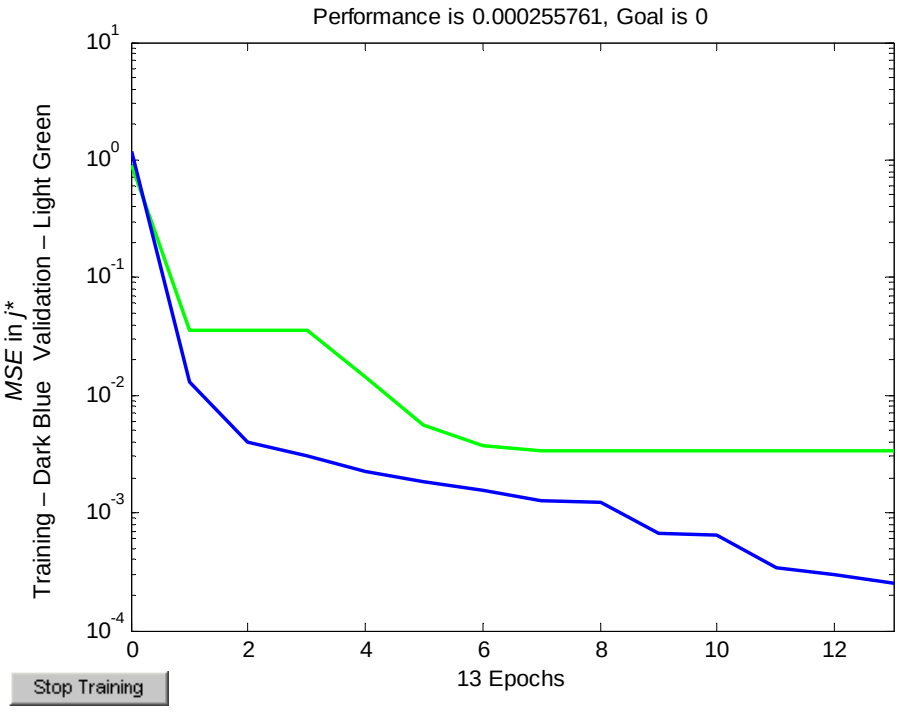

Performance curve

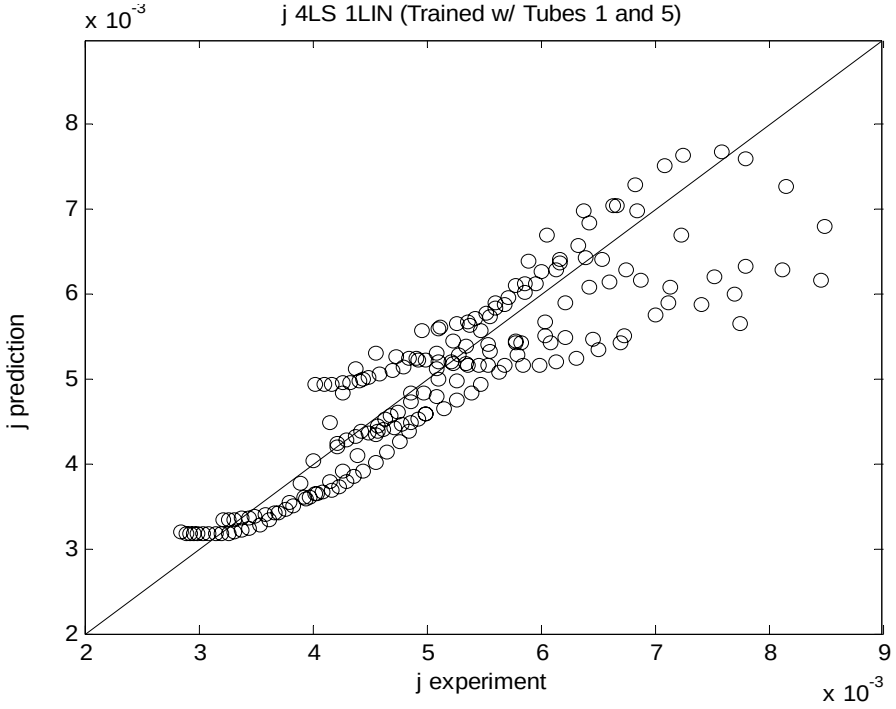

Training Set

Data from tubes 1 and 5. 46 data points (25.1 % of entire data set)

Validation Set

183 data points (entire data set)

Mean Squared Error

$MSE = 3.329\text{x}10^{-7}$

Architecture

1st layer: 4 nodes, log-sigmoid node functions
2nd layer: 1 node, linear node function

Weight Matrices

$$W^{1,0} = \begin{bmatrix} -6.004 & -17.5505 & -38.6115 & -4.9804 \\ -1.8435 & -15.911 & -31.3817 & -14.1376 \\ -2.0368 & 11.2466 & -33.0312 & 19.5385 \\ 6.2555 & -0.2014 & -15.7331 & -22.9495 \end{bmatrix}$$

$$W^{2,1} = \begin{bmatrix} -0.18254 & -0.11665 & 0.12348 & 0.35972 \end{bmatrix}$$

Bias Vectors

$$b^1 = \begin{bmatrix} 29.2771 \\ 29.031 \\ -9.9378 \\ 19.1673 \end{bmatrix} \qquad b^2 = \begin{bmatrix} 0.47934 \end{bmatrix}$$

- **j_4LS_1LIN (Trained with Tubes 1, 3, and 5)**

Training curve

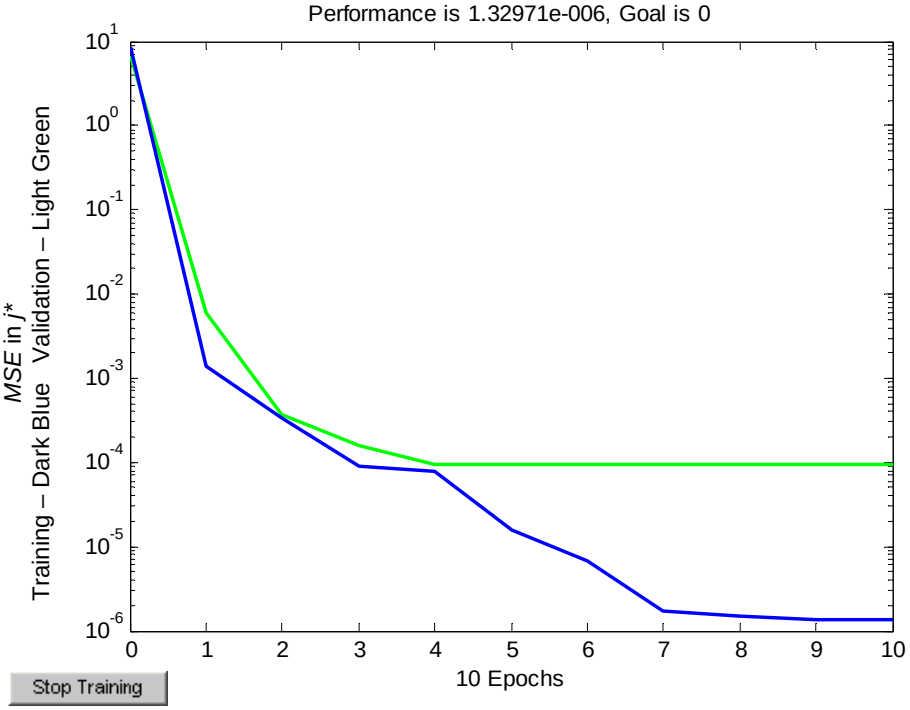

Performance curve

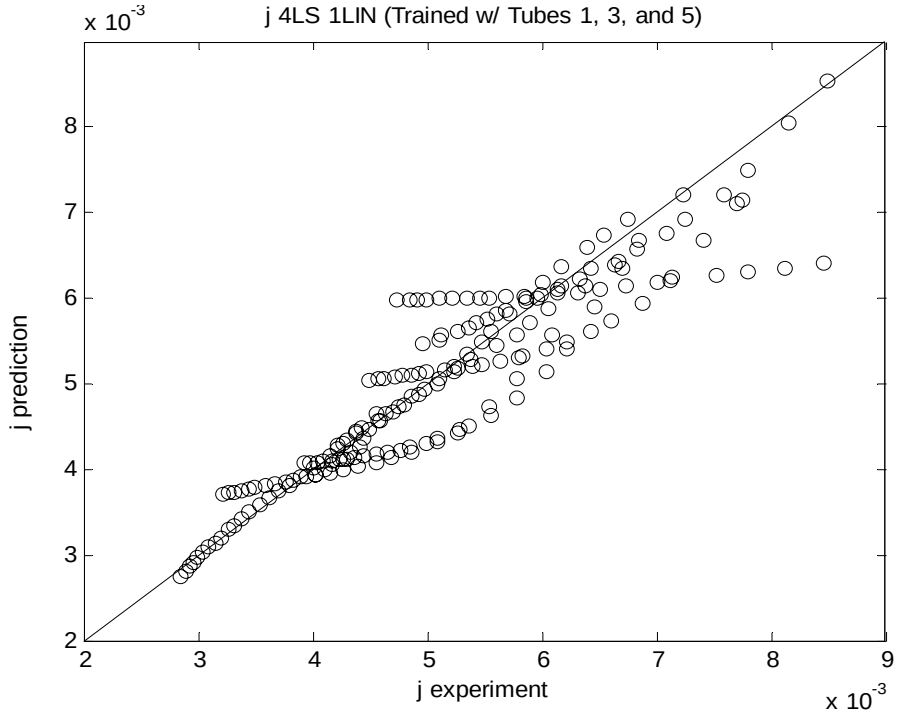

Training Set

Data from tubes 1, 3, and 5. 69 data points (37.7 % of entire data set)

Validation Set

183 data points (entire data set)

Mean Squared Error

$MSE = 2.324\text{x}10^{-7}$

Architecture

1st layer: 4 nodes, log-sigmoid node functions
2nd layer: 1 node, linear node function

Weight Matrices

$$W^{1,0} = \begin{bmatrix} -11.1716 & -21.5478 & -19.5312 & -2.1456 \\ -9.4318 & -0.09138 & 43.6481 & 14.1468 \\ -3.3483 & -2.5025 & 35.2687 & -19.4611 \\ 8.8253 & -8.4141 & 34.3957 & -13.8505 \end{bmatrix}$$

$$W^{2,1} = \begin{bmatrix} -0.23617 & -0.26859 & 0.05342 & 0.43427 \end{bmatrix}$$

Bias Vectors

$$b^1 = \begin{bmatrix} 23.9361 \\ -15.3394 \\ 5.8117 \\ 7.4493 \end{bmatrix} \qquad b^2 = \begin{bmatrix} 0.46653 \end{bmatrix}$$

- **j_4LS_1LIN (Trained with Tubes 1, 3, 5, and 7)**

Training curve

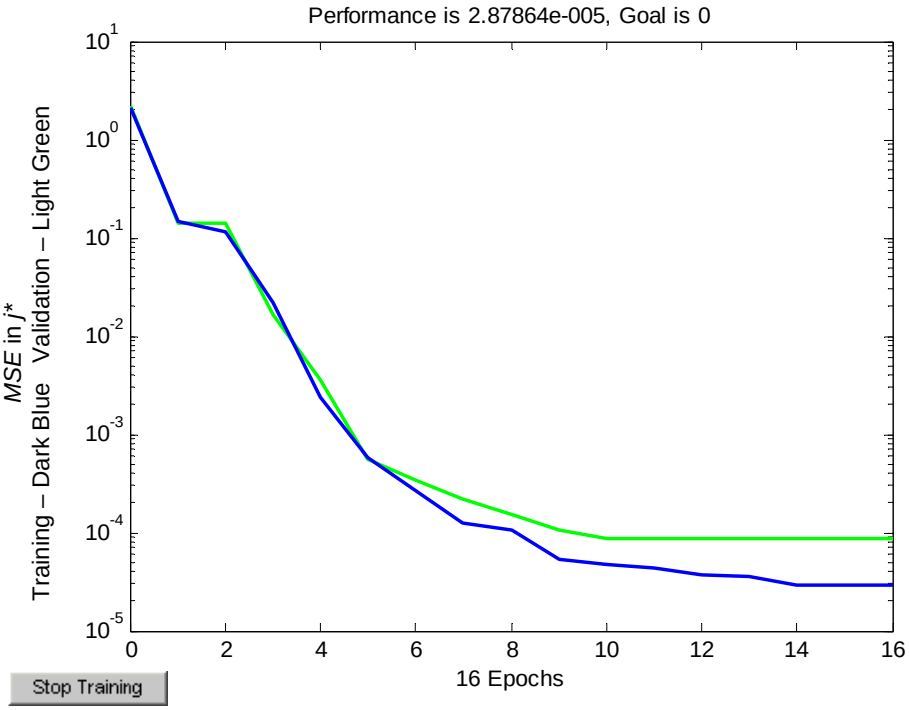

Performance curve

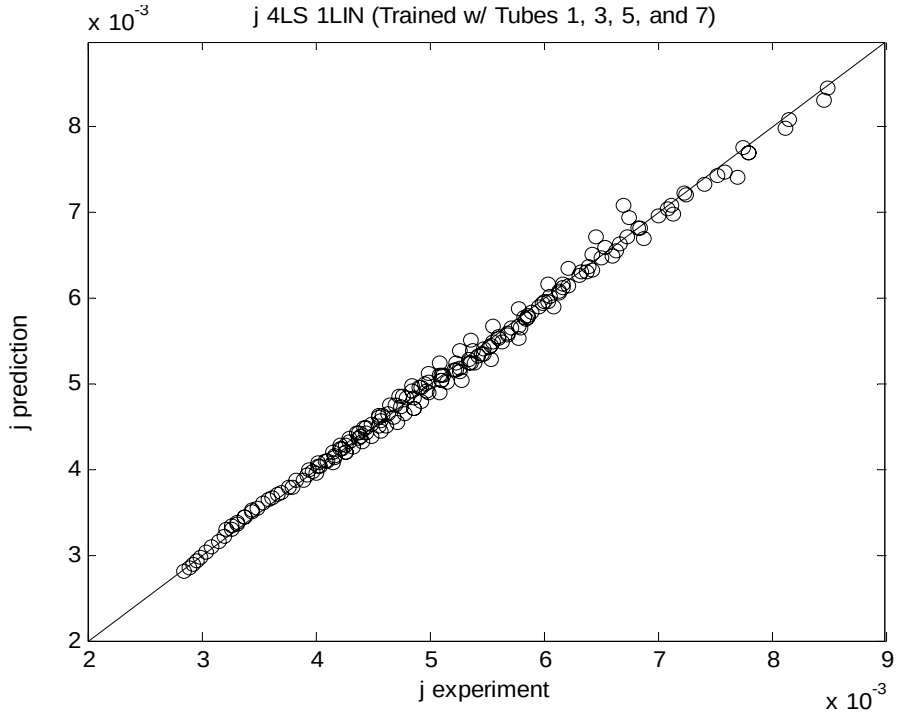

Training Set

Data from tubes 1, 3, 5, and 7. 91 data points (49.7 % of entire data set)

Validation Set

183 data points (entire data set)

Mean Squared Error

$MSE = 8.794 \text{x} 10^{-9}$

Architecture

1st layer: 4 nodes, log-sigmoid node functions
2nd layer: 1 node, linear node function

Weight Matrices

$$W^{1,0} = \begin{bmatrix} -4.055 & -2.1926 & -4.0848 & 4.4525 \\ -10.634 & 13.7955 & -33.2395 & -3.9029 \\ 10.8447 & -10.1747 & -31.4522 & 18.7794 \\ -0.53596 & -0.65698 & -13.9276 & -33.7803 \end{bmatrix}$$

$$W^{2,1} = \begin{bmatrix} -0.78438 & 0.36381 & -0.17828 & 0.093022 \end{bmatrix}$$

Bias Vectors

$$b^1 = \begin{bmatrix} 1.1736 \\ 21.1011 \\ 11.166 \\ 32.4836 \end{bmatrix} \qquad b^2 = \begin{bmatrix} 0.80879 \end{bmatrix}$$

- **j_4LS_1LIN (Trained with Tubes 1, 3, 4, 5, and 7)**

Training curve

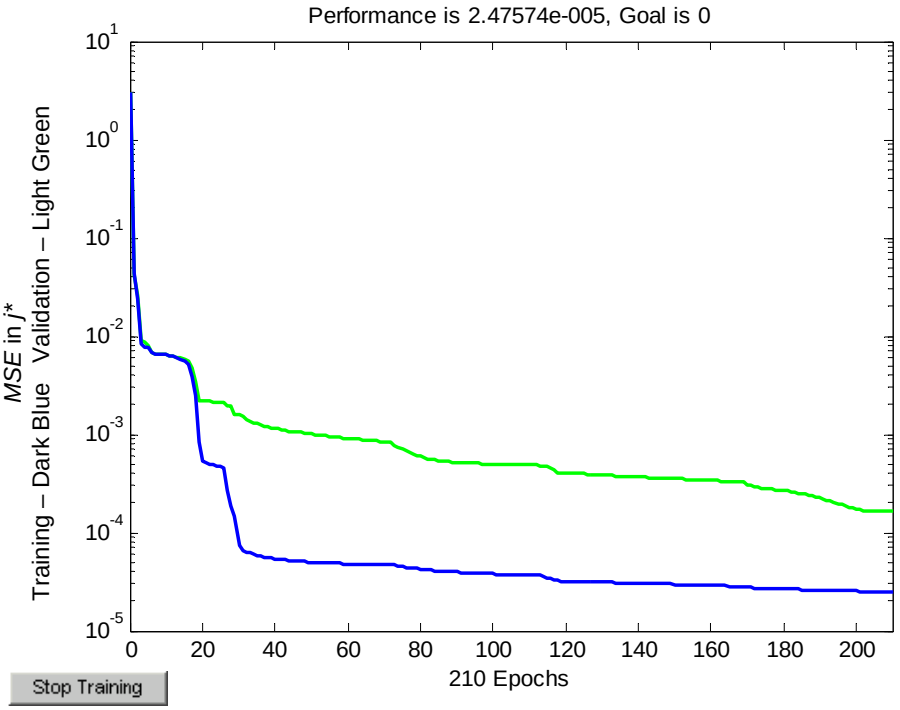

Performance curve

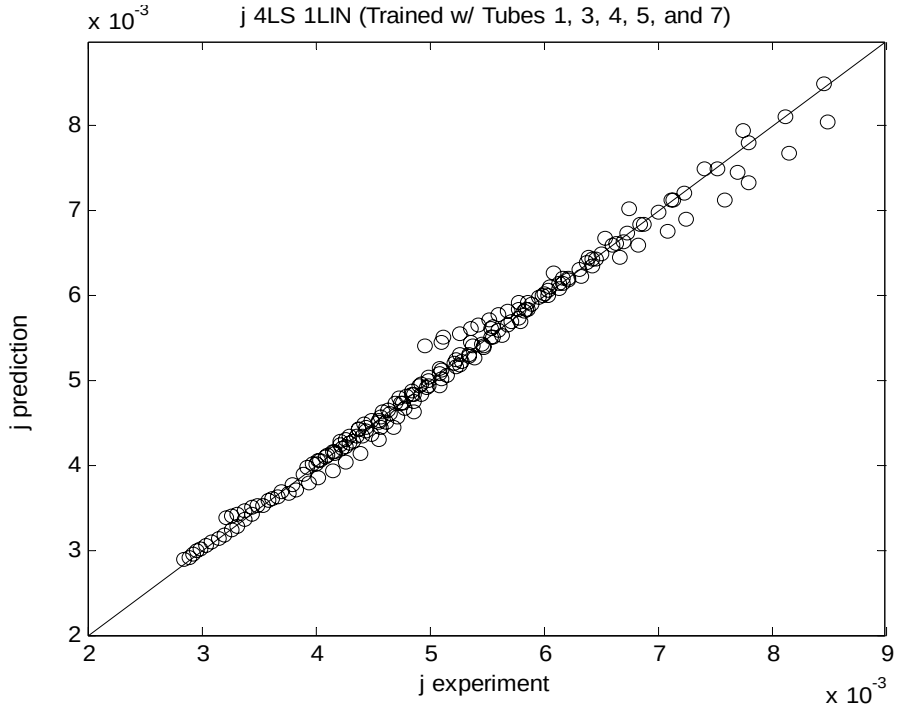

Training Set

Data from tubes 1, 3, 4, 5, and 7. 114 data points (62.3 % of entire data set)

Validation Set

183 data points (entire data set)

Mean Squared Error

$MSE = 1.668\text{x}10^{-8}$

Architecture

1st layer: 4 nodes, log-sigmoid node functions
2nd layer: 1 node, linear node function

Weight Matrices

$$W^{1,0} = \begin{bmatrix} -6.0542 & 28.073 & 13.9615 & -0.95522 \\ 18.1659 & 10.4271 & -10.2015 & -22.8403 \\ -18.6558 & -9.4831 & -45.0371 & -13.5521 \\ -0.87365 & 4.5951 & 3.9581 & 1.2164 \end{bmatrix}$$

$$W^{2,1} = \begin{bmatrix} 0.94486 & 0.11333 & -2.2533 & -2.4868 \end{bmatrix}$$

Bias Vectors

$$b^1 = \begin{bmatrix} -16.2809 \\ 8.2787 \\ 21.2551 \\ -4.6304 \end{bmatrix} \qquad b^2 = \begin{bmatrix} 1.0181 \end{bmatrix}$$

- **j_4LS_1LIN (Trained with Tubes 1, 3, 4, 5, 7, and 8)**

Training curve

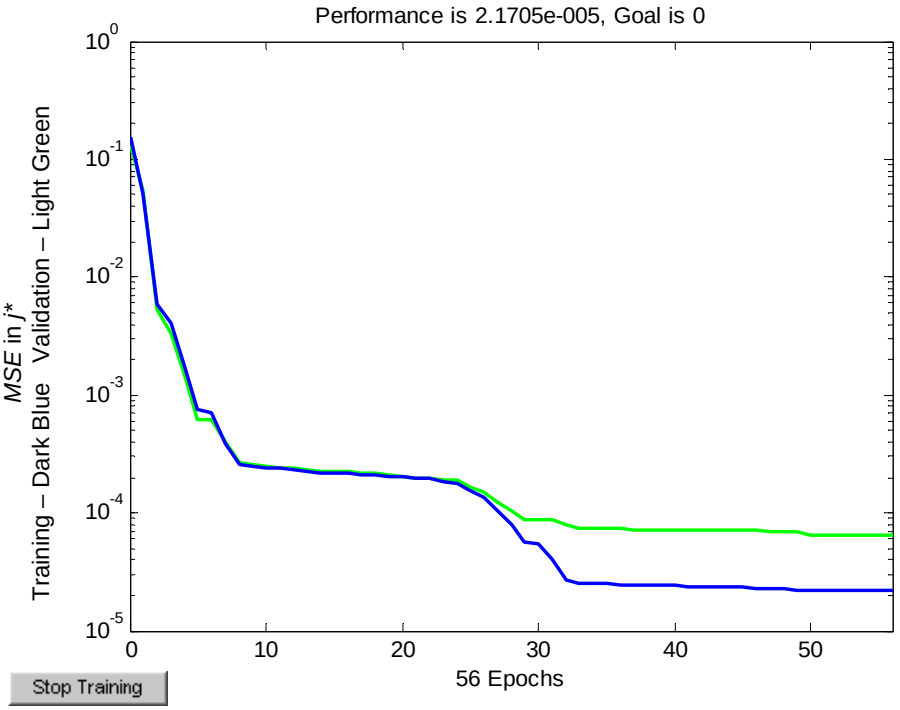

Performance curve

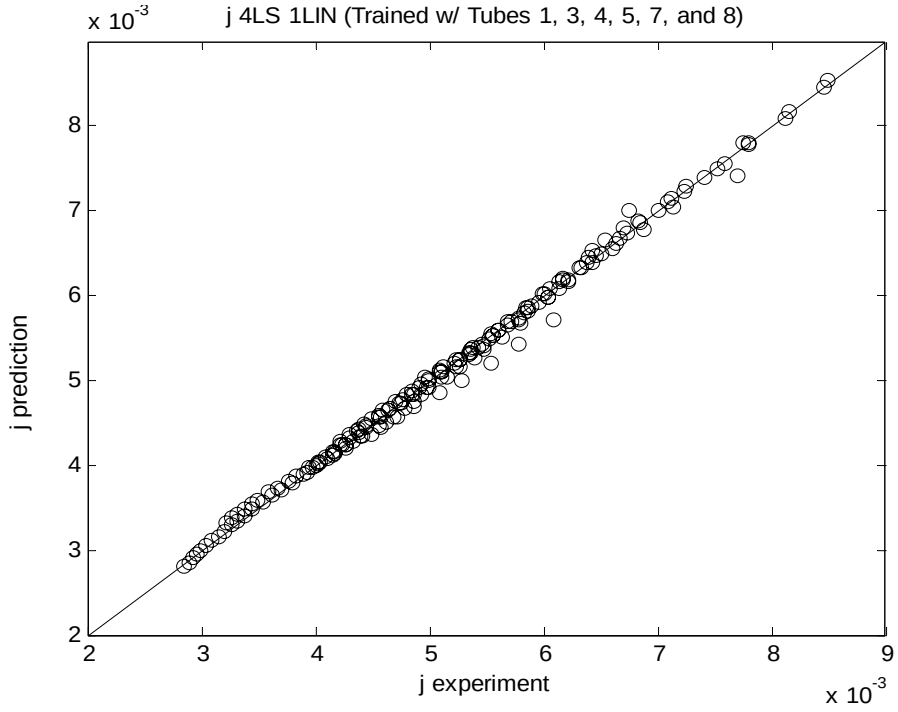

Training Set

Data from tubes 1, 3, 4, 5, 7, and 8. 137 data points (74.9 % of entire data set)

Validation Set

183 data points (entire data set)

Mean Squared Error

$MSE = 6.442\text{x}10^{-9}$

Architecture

1st layer: 4 nodes, log-sigmoid node functions
2nd layer: 1 node, linear node function

Weight Matrices

$$W^{1,0} = \begin{bmatrix} -0.35486 & 29.4055 & 20.7134 & -2.4885 \\ 3.0085 & 2.4883 & 3.284 & -2.9504 \\ 1.8288 & 19.4695 & -23.3021 & 10.3803 \\ -0.56618 & -2.4245 & -3.7767 & -14.0671 \end{bmatrix}$$

$$W^{2,1} = \begin{bmatrix} -0.080372 & 1.0847 & 0.21975 & 0.34233 \end{bmatrix}$$

Bias Vectors

$$b^1 = \begin{bmatrix} -25.1903 \\ -2.0774 \\ -20.4137 \\ 15.6018 \end{bmatrix} \qquad b^2 = \begin{bmatrix} -0.06288 \end{bmatrix}$$

A5. f_4LS_1LIN Network Trained with Half of Combined Database

Training curve

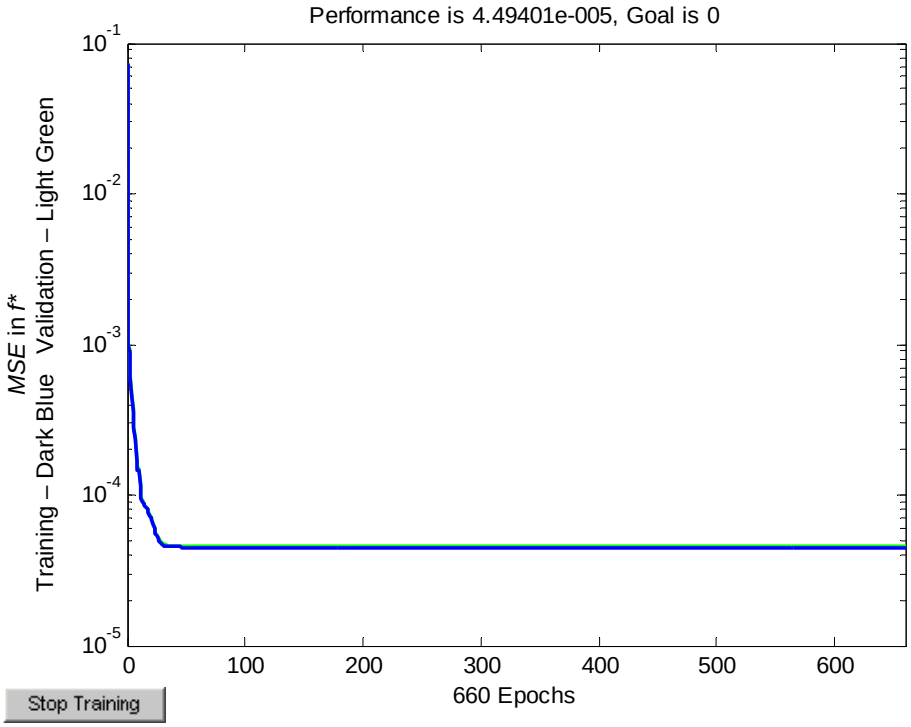

Performance curve

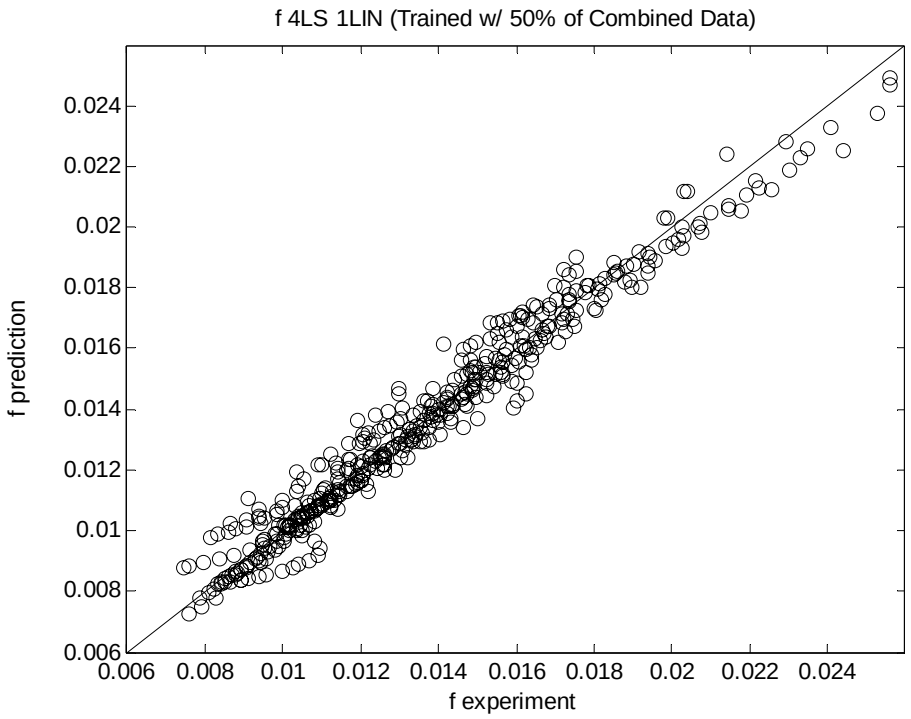

Training Set

219 data points (49.9 % of combined data of Jensen and Vlakancic (1999), Webb et al. (2000), and the current study; every other Reynolds number)

Validation Set

439 data points (combined data of Jensen and Vlakancic (1999), Webb et al. (2000), and the current study)

Mean Squared Error

$MSE = 4.553 \times 10^{-7}$

Architecture

1st layer: 4 nodes, log-sigmoid node functions
2nd layer: 1 node, linear node function

Weight Matrices

$$W^{1,0} = \begin{bmatrix} -7.2671 & -0.98217 & 2.0073 & 0.091471 \\ 7.5391 & 1.7808 & -2.2548 & -0.15899 \\ 3.5592 & -17.3752 & 4.0051 & -0.0099933 \\ -18.0686 & -9.384 & 4.6424 & 1.322 \end{bmatrix}$$

$$W^{2,1} = \begin{bmatrix} 13.8559 & 13.3015 & 0.77504 & -0.70134 \end{bmatrix}$$

Bias Vectors

$$b^1 = \begin{bmatrix} 1.5625 \\ -1.8321 \\ 7.5575 \\ 12.0355 \end{bmatrix} \qquad b^2 = \begin{bmatrix} -13.4947 \end{bmatrix}$$

A6. f_4LS_1LIN Network Trained with Half of Combined Database

Training curve

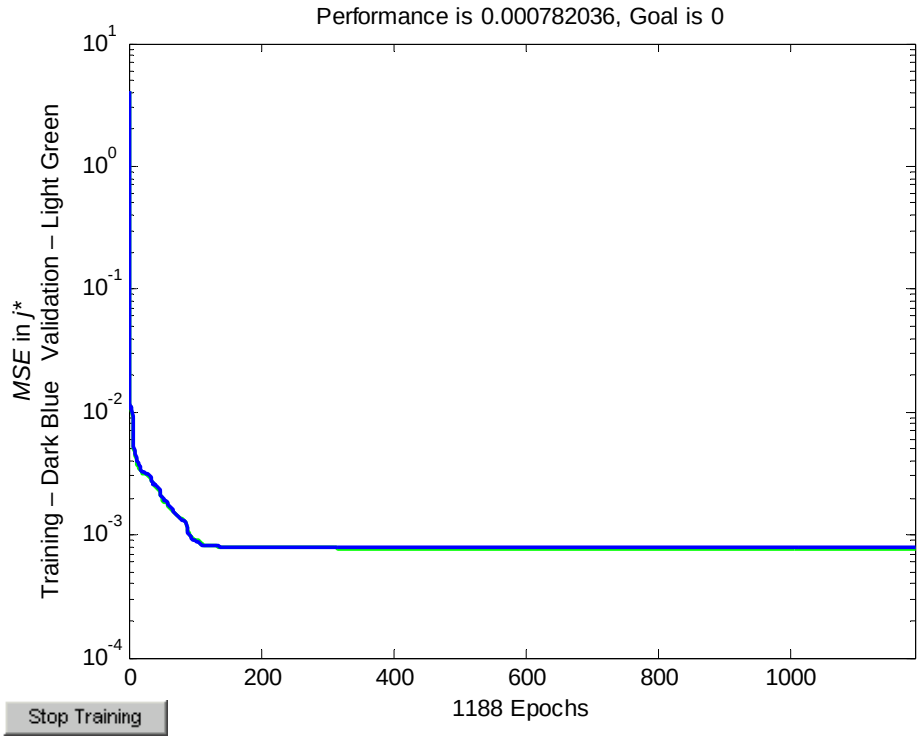

Performance curve

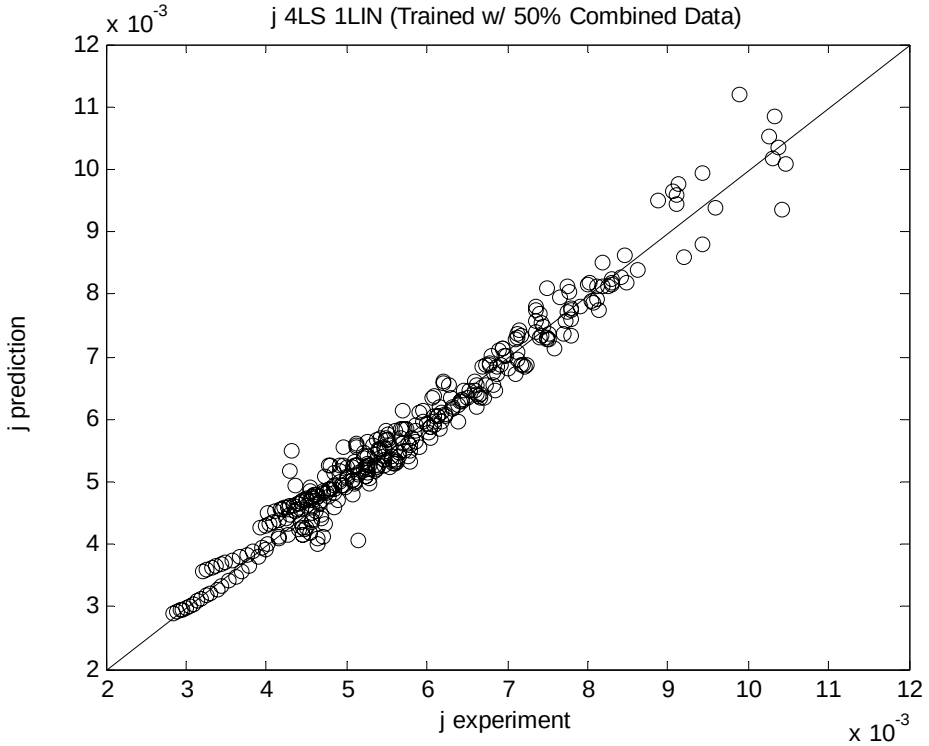

Training Set

171 data points (50.0 % of combined data of Jensen and Vlakancic (1999), Webb et al. (2000), and the current study; every other Reynolds number)

Validation Set

342 data points (combined data of Jensen and Vlakancic (1999), Webb et al. (2000), and the current study)

Mean Squared Error

$MSE = 7.671 \text{x} 10^{-8}$

Architecture

1st layer: 4 nodes, log-sigmoid node functions
2nd layer: 1 node, linear node function

Weight Matrices

$$W^{1,0} = \begin{bmatrix} -1.1545 & -0.068708 & -10.3588 & 2.0436 \\ -8.1534 & 62.9377 & -18.7554 & -0.12242 \\ 7.2905 & -127.338 & 16.7488 & 0.13477 \\ -108.2838 & -406.3062 & -595.2478 & 1.2132 \end{bmatrix}$$

$$W^{2,1} = \begin{bmatrix} -2.0141 & -173.9585 & -174.9652 & 0.95102 \end{bmatrix}$$

Bias Vectors

$$b^1 = \begin{bmatrix} 2.5897 \\ -30.5346 \\ 68.2465 \\ 402.9581 \end{bmatrix} \qquad b^2 = \begin{bmatrix} 176.0276 \end{bmatrix}$$